SANDIA REPORT
SAND2010-7501
Unlimited Release
Printed November 2010

Surface Rheology and Interface Stability

Lisa Mondy, Carlton Brooks, Anne Grillet, Harry Moffat, Tim Koehler, Melissa Yaklin,
Matt Reichert, Lynn Walker, Raymond Cote, Jaime Castañeda

Prepared by
Sandia National Laboratories
Albuquerque, New Mexico 87185 and Livermore, California 94550

Sandia National Laboratories is a multi-program laboratory managed and operated by Sandia Corporation, a wholly owned subsidiary of Lockheed Martin Corporation, for the U.S. Department of Energy's National Nuclear Security Administration under contract DE-AC04-94AL85000.

Sandia National Laboratories

Issued by Sandia National Laboratories, operated for the United States Department of Energy by Sandia Corporation.

Available to DOE and DOE contractors from
U.S. Department of Energy
Office of Scientific and Technical Information
P.O. Box 62
Oak Ridge, TN 37831

Telephone: (865) 576-8401
Facsimile: (865) 576-5728
E-Mail: reports@adonis.osti.gov
Online ordering: http://www.osti.gov/bridge

Available to the public from
U.S. Department of Commerce
National Technical Information Service
5285 Port Royal Rd.
Springfield, VA 22161

Telephone: (800) 553-6847
Facsimile: (703) 605-6900
E-Mail: orders@ntis.fedworld.gov
Online order: http://www.ntis.gov/help/ordermethods.asp?loc=7-4-0#online

SAND2010-7501
Unlimited Release
Printed November 2010

Surface Rheology and Interface Stability

Lisa Mondy,[1] Carlton Brooks,[1] Anne Grillet,[1] Harry Moffat,[2] Tim Koehler,[3] Melissa Yaklin,[3]
Matt Reichert,[4] Lynn Walker,[4] Raymond Cote, [1] Jaime Castañeda[1]

[1]Thermal/Fluid Experimental Sciences
[2]Nanoscale and Reactive Processes
[3]Microscale Science and Technology
Sandia National Laboratories
P.O. Box 5800
Albuquerque, New Mexico 87185-MS0346

[4]Department of Chemical Engineering
Carnegie Mellon University
5000 Forbes Avenue
Pittsburgh, PA 15213-3890

Abstract

We have developed a mature laboratory at Sandia to measure interfacial rheology, using a combination of home-built, commercially available, and customized commercial tools. An Interfacial Shear Rheometer (KSV ISR-400) was modified and the software improved to increase sensitivity and reliability. Another shear rheometer, a TA Instruments AR-G2, was equipped with a du Noüy ring, bicone geometry, and a double wall ring. These interfacial attachments were compared to each other and to the ISR. The best results with the AR-G2 were obtained with the du Noüy ring. A Micro-Interfacial Rheometer (MIR) was developed in house to obtain the much higher sensitivity given by a smaller probe. However, it was found to be difficult to apply this technique for highly elastic surfaces. Interfaces also exhibit dilatational rheology when the interface changes area, such as occurs when bubbles grow or shrink. To measure this rheological response we developed a Surface Dilatational Rheometer (SDR), in which changes in surface tension with surface area are measured during the oscillation of the volume of a pendant drop or bubble. All instruments were tested with various surfactant solutions to determine the limitations of each. In addition, foaming capability and foam stability were tested and compared with the rheology data. It was found that there was no clear correlation of surface rheology with foaming/defoaming with different types of surfactants, but, within a family of surfactants, rheology could predict the foam stability. Diffusion of surfactants to the interface and the behavior of polyelectrolytes were two subjects studied with the new equipment. Finally, surface rheological terms were added to a finite element Navier-Stokes solver and preliminary testing of the code completed. Recommendations for improved implementation were given. When completed we plan to use the computations to better interpret the experimental data and account for the effects of the underlying bulk fluid.

ACKNOWLEDGMENTS

The authors gratefully acknowledge the support of the Laboratory Directed Research and Development (LDRD) Program. We would like to thank Edna S. Wong for her assistance in getting the Langmuir trough operational for the ISR. Rekha Rao (1512) was instrumental in the initial stages of developing the modeling approach and is a coauthor of Appendix C.

CONTENTS

FIGURES

TABLES

LIST OF SYMBOLS

A = drop surface area or contact area of probe with subphase [=] length^2 = mm^2

A_0 = initial surface area of drop

A_p = surface area of interfacial probe

D_s = Interfacial diffusion coefficient

$\underline{\underline{D_s}}$ = symmetric surface rate of deformation tensor [=] 1/s

E_s = surface tensile (Young’s) modulus [=]force/length = mN/m

f = frequency [=] Hz

g = acceleration due to gravity [=] length/time^2 = m/s^2

G_s = surface shear modulus [=]force/length = mN/m

G_s^* = dynamic surface shear modulus $= G_s' + iG_s''$ [=] force/length = mN/m

G_s' = dynamic surface shear storage modulus [=] force/length = mN/m

G_s'' = dynamic surface shear loss modulus [=] force/length = mN/m

k_B = Boltzmann’s constant

K_s = surface dilatational modulus [=] mN/m

K_s^* = dynamic surface dilatational modulus $= K_s' + iK_s''$ [=] force/length = mN/m

K_s' = dynamic surface dilatational storage modulus [=] force/length = mN/m

K_s'' = dynamic surface dilatational loss modulus [=] force/length = mN/m

L = length of rod (needle) in the ISR [=] length

N_{Bd} = Bond number [=] dimensionless

N_{Bq} = Boussinesq number [=] dimensionless

N_{Re} = Reynolds number [=] dimensionless

P = perimeter of the interface probe in contact with the interface [=] length = mm

R = probe geometry [=] length

R_0 = radius of curvature at pendant drop apex [=] length = cm

R_1, R_2 = principal radii of curvature [=] length = cm

s = surface contour coordinate

T = temperature

$\boldsymbol{T}_{in}, \boldsymbol{T}_{ext}$ = bulk stress tensor for the internal and external phases, respectively [=] force/length^2

V = drop volume [=] length^3= µL or mm^3

Greek Symbols

α_s = surface dilatational strain

γ = shear strain

γ_E =Euler's constant = 0.57721566…

γ_s = surface shear strain

δ = modulus phase angle

$\underline{\underline{\varepsilon}}_s$ = surface strain tensor

η_b = Shear viscosity of the bulk fluid [=] mN-s/m^2

η_s = Surface shear viscosity (non-Newtonian) [=] mN-s/m

η_s^* = Dynamic surface shear viscosity = $\eta_s' + i\eta_s''$ [=] mN-s/m

θ = contact angle

κ_s = Surface Newtonian dilatational viscosity [=] mN-s/m

μ_s = Surface Newtonian shear viscosity [=] mN-s/m

ν_s = surface Poisson's ratio

π = pi = 3.14159265…

Π = surface pressure [=] force/length = mN/m

σ = surface tension [=] force/length = mN/m

$\underline{\underline{\sigma_s}}$ = surface stress tensor [=] force/length = mN/m

$\underline{\Upsilon}_{\boldsymbol{s}}$= surface stress tensor

ψ = phase angle from fitting the responses to a sine function [=] radians

$\underline{\underline{\tau_s}}$ = surface deviatoric stress tensor [=] force/length = mN/m

φ = angle of the surface normal with respect to the z-axis

ω = angular frequency [=] rad/s

LIST OF ABBREVIATIONS, ACRONYMS, & INITIALISMS

ARIA = name of a Sandia developed finite element fluids code in SIERRA family of engineering codes

GOMA = name of a Sandia developed finite element fluids code

ISR = Interfacial Stress Rheometer

MIR = Micro Interfacial Rheometer

PES = Poly Electrolyte Surfactant

SDR = Surface Dilatational Rheometer

SEM = Scanning Electron Microscopy

1. INTRODUCTION

Microfluidic devices have demonstrated a broad range of applications and are areas of active research. At small length scales the surface to volume ratio is large, and the properties of interfacial boundaries predominate. In addition to microfluidics, many macroscopic applications with large surface areas have properties that are strongly influenced by interfacial phenomena, e.g. foams, emulsions, and nano-suspensions. In the context of foams, the role of the interface is dramatic. Foams cannot be made with pure liquids, and require the presence of a second material which is surface active, called surfactants. The role of surfactants in foam stability is illustrated in Figure 1. The surfactants resist deformation of the interface, which inhibits the rate of drainage of liquid films in the foam. The interface can have distinct rheology when compared to the bulk properties on either side of the boundary. Due to the large effects that interfaces can impart on macroscopic flows, the aim of this project was to develop a better understanding of interfacial rheology and to develop predictive simulation tools that incorporate surface rheological phenomenon into multiphase simulations.

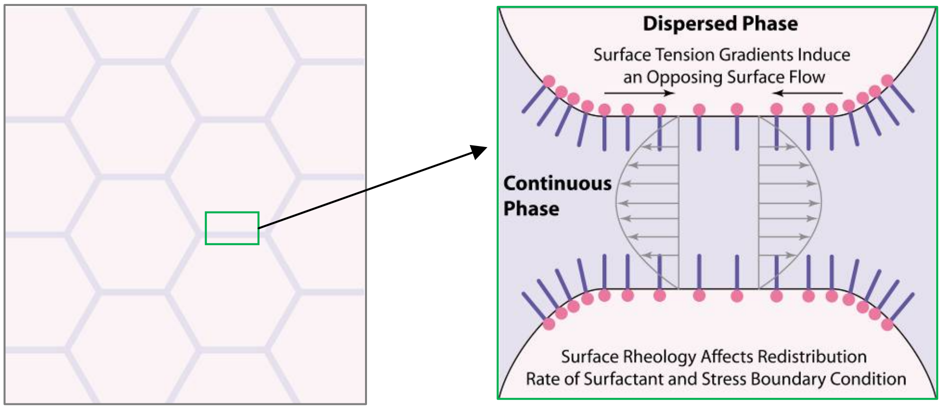

Figure 1: Surfactants at interfaces give the boundary distinctly different properties than the bulk fluid and can affect flow boundary conditions. At left is a hexagonal foam cell structure. At right is a microscopic view of the role of surfactants at the interface.

Interfaces can be deformed in a variety of ways, similar to bulk materials. Figure 2 illustrates fundamental flow fields that can be developed at interfaces: dilation, shear, and extension. We have obtained two commercially available state-of-the-art interfacial rheometers: a KSV ISR-400 Interfacial Shear Rheometer (ISR) and a TA AR-G2 shear rheometer with several attachments to measure interfacial viscosity. We tested and/or improved the instruments as will be described in the following sections. Furthermore, we developed a Micro-Interfacial Rheometer (MIR) in which particles at an interface are tracked to provide a direct probe of an air-liquid interface. These instruments all measure the shear response. In addition, we developed a Surface Dilatational Rheometer (SDR) to measure the dynamic response of an interface when expanded and contracted. We have, thus, established a unique surface characterization capability.

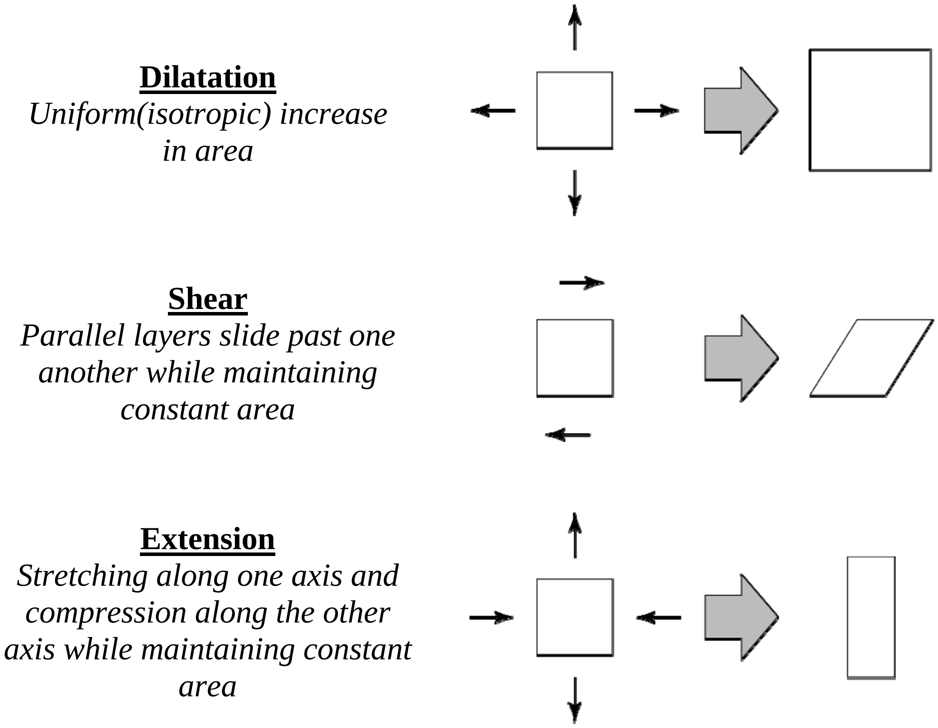

Figure 2: Fundamental deformations possible for an interface: dilatational (top), shear (middle), and extension (bottom)

Studies of the interfacial rheology of aqueous solutions of several families of surface active materials including surfactants, proteins, and polyelectrolytes, as well as the foaming and foam stability behavior of these solutions were undertaken both to examine the sensitivity ranges of the new apparatuses and to learn more about the connection among interfacial rheology and foam behavior. Studies were also undertaken to better understand the dynamics of surfactant adsorption and investigate the role of diffusion-limited situations as identified by Alvarez et al. (2010). In addition, the effects of polyelectrolyte-surfactant aggregates on the mechanical properties of the air-liquid interface were also explored.

Finally, surface rheological models were developed and implemented in GOMA. Currently, no commercially available code can include surface rheological effects; therefore, this work, although not fully matured, resulted in a unique capability for Sandia.

The new Surface Rheology Lab will continue to provide cutting-edge experimental discoveries necessary to extend current computational models. Measurements can now be performed that are critical to understanding the drainage of foam lamella phenomenon relevant in foaming and degassing, nuclear fuel rod reprocessing, and industrial waste treatment processes, as well as emerging technologies such as microencapsulation, microreactors, and clinical diagnostic assays. In addition, we will provide interfacial property data and perform validation experiments vital to the development of surface rheological models to be included in fluids codes such as ARIA. These techniques can also provide measurements important to other computational capabilities in development such as nanoparticle interactions in suspensions or interactions between emulsifying agents used in foaming processes, where the physics is dominated by the thin liquid films of the continuous phase.

2. NEW INSTRUMENTATION

The following subsections describe several approaches used in this work to measure the shear and dilatational rheology of interfaces. The first three focus on techniques to measure the *shear* rheology of interfaces using several techniques. In Section 2.5 a technique that oscillates a pendant drop is described to measure the *dilatational* rheology of interfaces.

2.1. Interfacial Shear Rheology

One of the primary challenges faced when trying to measure the rheology of surfaces (air-liquid) or interfaces (liquid-liquid) is the coupling of the flow at the surface with the surrounding bulk phases. When using a probe placed at an interface to measure surface rheology, it is useful to construct a dimensionless Boussinesq number to describe the degree of coupling with the bulk [Edwards et al. 1991]. The total drag on the probe comes from two sources, the bulk and the surface. The Boussinesq number, N_{Bq}, is the ratio of the surface drag, which acts on the perimeter of the probe, to the bulk drag, which acts on the contact area:

$$N_{\mathrm{Bq}} = \frac{\text{Surface Drag}}{\text{Bulk Drag}} \tag{2.1.1}$$

Ideally, to measure the surface drag without any artifacts from the bulk, a large Boussinesq number is required. However, in addition to a large N_{Bq}, there is also a requirement that the deformation profile is known *a priori* to accurately determine the surface shear rate where the surface contacts the probe. Since the surface also experiences coupling to the subphase, the geometry of the flow cell also can influence the deformation within the interface. As a consequence N_{Bq} >>1 is necessary, but not sufficient, for directly measuring the rheological properties of the surface. To determine the conditions where the subphase can be neglected requires a full analysis of the flow field that identifies what the *minimum* value of N_{Bq} is needed for a given geometry and material properties of the surrounding phases [Reynaert et al. 2008].

Often measurements of surface rheology are taken in an oscillatory mode, which gives values of the dynamic surface shear modulus G_s^*, which is composed of a real component $G_s^{'}$ (storage/elasticity term) and an imaginary component $G_s^{''}$ (loss/dissipative term).

Presumably in two-dimensional flows, the surface shear modulus can be related to the steady surface shear viscosity η_s by the Cox-Merz rule (equation 2.1.2), as in similar measurements for the bulk liquid [Al-Hadithi et al. 1992, Renardy 1997].

$$\left|\eta_s^*(\omega)\right| = \left|G_s^*(\omega)\right| / \omega = \eta_s(\dot{\gamma} = \omega) \tag{2.1.2}$$

This rule states that the magnitude of the complex viscosity $\left|\eta_s^*(\omega)\right|$ is equivalent to η_s when the angular frequency ω is equal to the steady shear rate $\dot{\gamma}$.

2.2. Interfacial Stress Rheometer (ISR)

We modified a commercial interfacial stress rheometer (ISR) (KSV Instruments ISR400, Helsinki) whose design was based on Carlton Brooks' thesis work (Figure 3 & Figure 4) [Brooks et al. 1999] the investigate the *shear* deformation of interfaces. The ISR uses a Langmuir trough to prepare monolayers of insoluble surfactant with a desired surface density at an air-liquid interface. A Teflon® coated magnetized needle is freely suspended at the interface due to surface tension forces. The needle is subjected to a periodic magnetic field gradient with a pair of Helmholtz coils, and from the amplitude and phase shift of the needle displacement, the viscoelastic properties of the interface are measured.

$$\frac{\partial \tau_s}{\partial \gamma_s} = G_s^*(\omega) = G_s^{'}(\omega) + iG_s^{''}(\omega) = \left|G_s^*(\omega)\right|\cos\delta + i\left|G_s^*(\omega)\right|\sin\delta \qquad (2.2.1)$$

where τ_s is the surface shear stress applied by the coils, γ_s is the surface strain from the measured needle displacement, and δ is the phase angle.

We modified the KSV ISR400 in several ways:

1) We moved the entire barrier drive mechanism for the Langmuir trough outside the Helmholtz coils. The components of the drive mechanism were made of ferrous materials, which disrupted the uniformity of the magnetic field created by the Helmholtz coils. We also eliminated the use of the gooseneck light source since it was also made of magnetic materials. We replaced it with a fiber-optic light diffuser situated below the Langmuir trough, and passed the light through a quartz window in the trough.

2) We made custom flow cells out of cylindrical tubing. This was to maintain consistency with numerical analysis of the coupling of the surface flow to the subphase flow [Brooks 1999, Reynaert et al. 2008]. Cylindrical tubes with 1 mm thick walls were cut into lengths of 100 mm and cut 1 mm off the centerline (see Fig. 5). Cylinders with inner diameters of 4, 5, 6, 7, 8, and 10 mm were made.

3) We replaced the firewire camera that came with the instrument with a high speed firewire camera, increasing the rate at which we could acquire frames from 60 to 200 frames per second. Custom software was also written in LabVIEW to track the lateral position of the needle, in addition to its axial position. This creates the capability to potentially measure normal stress differences by oscillating the needle when it is not located in the center of the flow cell and observing a 2ω response in the lateral position.

4) Data acquisition circuitry was installed that measures the current being delivered to the coils. Inevitably, there is inductive cross-coupling between the coils and high frequency roll-off with the power supplies driving the coils. As a consequence there is no guarantee that both the amplitude and phase of the current that is commanded to the power supplies is actually delivered. Previous embodiments of the instrument assumed that the commanded current from the power supplies was actually sent to the coils. In this new configuration, measurement of the voltage across a high power 1-Ohm resistor in series with the coils enables the direct measurement of the current passing through the coils, eliminating this uncertainty.

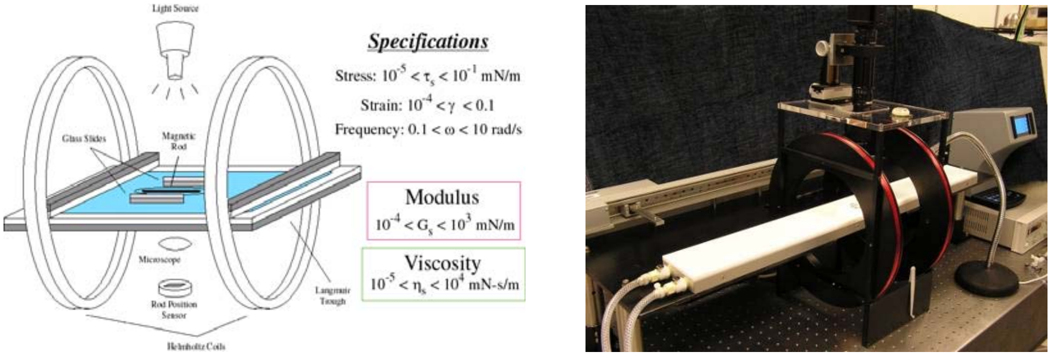

Figure 3: Interfacial stress rheometer (ISR) designed by Brooks 1999 (left) and a photo of Sandia's system (right).

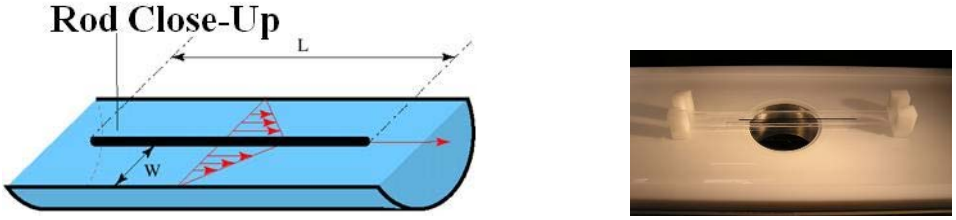

Figure 4: Close up of the needle used in the ISR

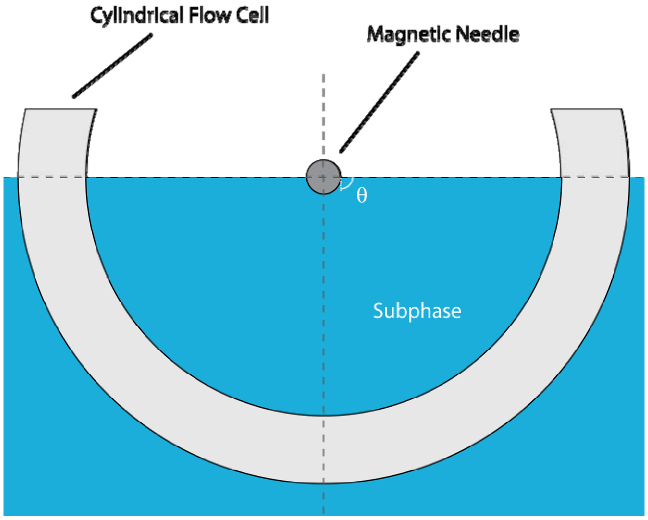

Figure 5: Cross sectional view of rod in flow cell, identifying the contact angle (θ), and the assumption of a flat interface (zero gravity).

For the needle geometry, a dimensionless Boussinesq number can be formed

$$N_{\mathrm{Bq}}^{\mathrm{ISR}} = \frac{\eta_s P}{\eta_b A} = \frac{\eta_s (2L + 4R)}{\eta_b 2(\pi - \theta)RL} = \frac{\eta_s}{\eta_b R(\pi - \theta)} \quad \text{for } R << L \tag{2.2.2}$$

where η_s is the surface viscosity, η_b is the viscosity of the bulk fluid, P is the perimeter of the probe in contact with the interface, A is the area of the probe in contact with the subphase, θ is the contact angle of the liquid on the probe, L is the length of the rod, and R is the radius. Note that the units of surface viscosity vary from those of the bulk viscosity by a length scale. For the ISR the radius of the probe *R* is 0.245 mm. To ensure the deformation profile at the interface is constant, a large Boussinesq number ($N_{\mathrm{Bq}}^{\mathrm{ISR}}$>>100) is desired [Brooks 1999, Reynaert et al. 2008].

2.3. TA Instruments AR-G2

The du Noüy ring, commonly used for interfacial tension measurements has been successfully applied to interfacial shear testing. Like the bi-cone, the ring is located at the interface of two liquids or a liquid and a gas. When the ring is subjected to an angular displacement, the surface between the ring and the circular wall of the vessel containing the liquids is sheared. The light construction of the ring permits the characterization of very fragile interfaces, without the inertia dominating the experiment. However, most bulk rheometers have too low sensitivity and too high inertia to use the du Noüy ring in oscillation mode. The AR-G2 rotational rheometer (TA Instruments) with a torque range of almost nine decades and a sensitivity comparable to that of the specialized interfacial rheometers, has been successfully used in conjunction with a du Noüy ring to perform dynamic interfacial rheology measurements over and beyond the range of specialized instruments. [Franck 2010]

The du Noüy ring can be used with the AR-G2 for sensitive interfacial measurements, because of its low inertia and its capability to control and apply tiny torques. The du Noüy ring is attached to the stress motor, mounted on the slide of the rheometer. In the basic setup, a circular glass dish locates in the center on the Peltier plate and held in position with an annular Peltier cover as shown in Figure 6. The du Noüy ring used in these investigations is shown in Figure 6 and has a radius of 10 mm, the thickness of the Pt-Ir wire being 0.36mm. Note that the annulus between inner and outer ring (R_2-R_1) is much wider, than what is typically used in bulk measurements. Possible errors due to the wide gap are not accounted for. [Franck 2010]

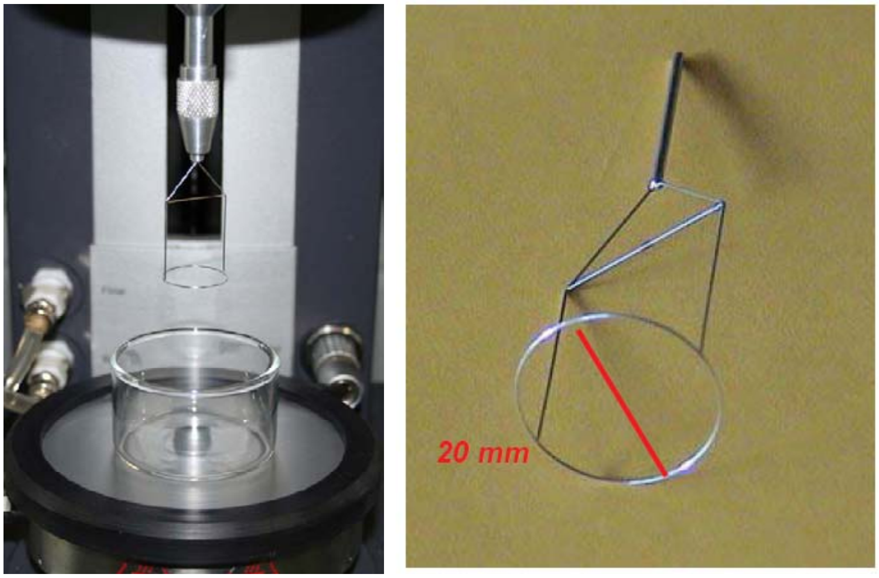

Figure 6: TA Instruments AR-G2 with du Noüy ring attachment.

Franck of TA Instruments has compared the performance of the AR-G2 with the du Noüy ring with an interfacial stress rheometer (ISR400) for a 0.35µM solution of lysozyme that was prepared in a phosphate buffer, pH 7.2. The decane was added after the du Noüy ring was positioned at the surface. The full lines in Figure 7 show the development of the interfacial storage G_s' and loss modulus G_s" with time, measured at a frequency of 0.05Hz and a strain amplitude of 2%. G_s' increases faster than G_s", which is due to the formation of a strong elastic gel at the interface. [Franck] These results compare well with previous measurements done with the ISR400 rheometer developed by Carlton Brooks and Gerry Fuller [Freer et al. 2003]. The measurements with the ISR400 were conducted over a much longer time period, showing that the modulus continues to increase indefinitely. The same test conditions were chosen for both experiments, except slight differences in the buffer pH (7.0 vs. 7.2) and the second liquid phase (decane vs. hexadecane). After the adsorption of the native globular protein at the interface, partial unfolding takes place, exposing the hydrophobic groups. The proteins aggregate and form an elastic layer. The continuous increase of the interfacial shear modulus suggest that proteins continue to unfold and aggregate, forming multiple layers at the interface [Freer et al. 2003].

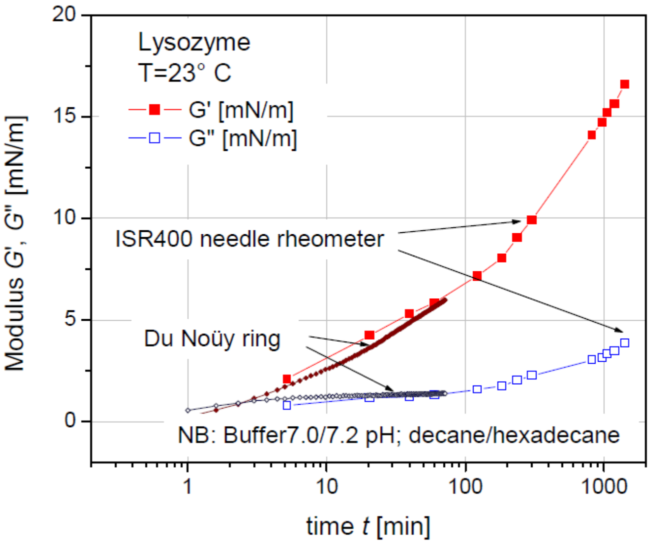

Figure 7: Comparison of AR-G2 with du Noüy ring and ISR400 for 0.35µM lysozyme showing modulus as a function of time. [Franck 2010]

We have also employed the new interfacial measurements geometry marketed by TA Instruments the Double Wall Ring (DWR) which is shown in Figure 8.

In Figure 9, we show results for a 0.1wt% bovine serum albumin (BSA) solution in 1mM NaCl using both interfacial fixtures to illustrate the results and possible pitfalls of these interfacial rheology measurements.

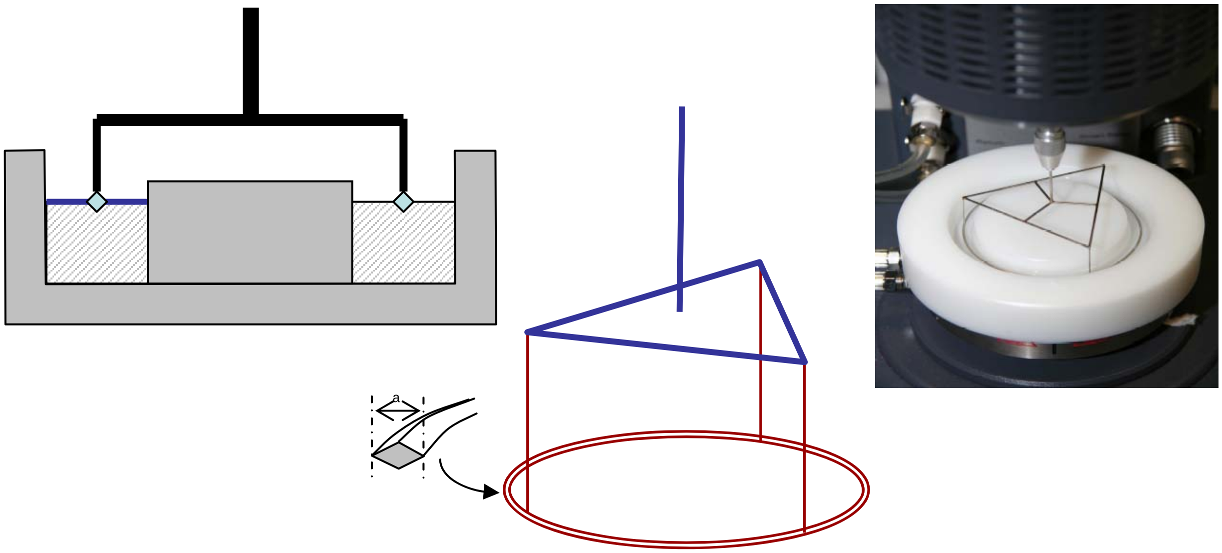

Figure 8: TA Instruments Double Wall Ring (DWR) interfacial rheology fixture.

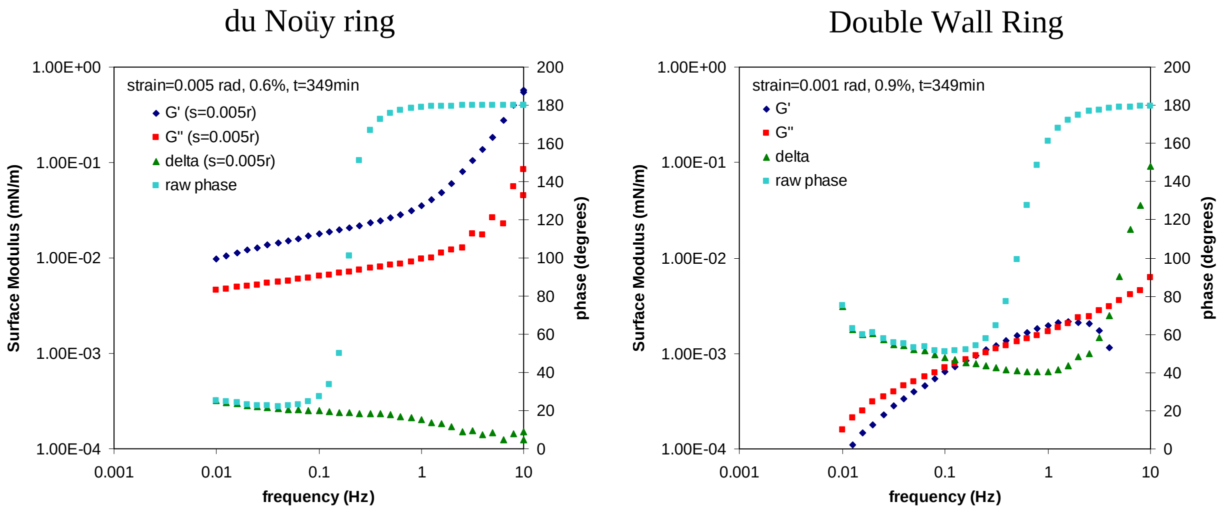
du Noüy ring

Double Wall Ring

Figure 9: Comparison of du Noüy ring and DWR for 0.1wt% BSA solution showing both quanitative and qualitative disagreement between the two fixtures.

We have employed the AR-G2 with du Noüy ring according to manufacturer suggestions. The glass cup was cleaned with a solvent and then rinsed several times with fresh Milli-Q water. The ring was flamed with a propane torch prior to use. The main limitation with use of the AR-G2 for surface rheology measurements is the small signal, which can be overwhelmed by the tool inertia. In Figure 9 on the left, the measured interfacial moduli and both the calculated and raw phase are shown over a range of frequencies at a constant strain amplitude of 0.0005 radians. For frequencies below 0.1Hz, the raw phase and calculated phase overlap indicating that tool inertia is negligible. In this regime, the elastic portion of the surface modulus dominates over the viscous component and both increase slowly with frequency. For frequencies above 0.1Hz, the raw phase rapidly increases to 180°. That is the hallmark of inertia dominated signal. The instrument performs a series of corrections to remove inertia from the signal. Eventually, the calculated values get increasingly noisy and above 1Hz the data can no longer be trusted. Thus the large increase in the modulus at high frequencies is not believed to be physical. The oscillatory mapping is supposed to improve inertial corrections and hence data quality at high frequencies or large strain, but did not affect data in the region where the raw and calculated strains are in agreement. In section 3.3, we will demonstrate that results from the Du Noüy ring compare fairly well with measurements on BSA interfaces using the ISR.

Results for the double wall ring fixture are shown on the right side of Figure 9. Our initial expectation was that the double wall ring would provide improved sensitivity since the geometry was designed to more accurately account for subphase contribution. However, that was not the case. As shown above, the results from the double wall ring were several orders of magnitude different from both the ISR and the Du Noüy ring. They were also qualitatively different in that the elastic and viscous components of the interfacial module were nearly the same order of magnitude with a cross-over point ~0.2Hz. Once again tool inertia renders data measured for frequencies greater than 1Hz unreliable. We favor the Du Noüy ring attachment because of its high surface sensitivity and low inertia, which allows the broadest range of measurement parameters.

Again to ensure that the measured stress is dominated by the interfacial rheology a large N_{Bq} is desired (equation 2.2.2). For the Du Noüy ring where the radius of the ring *R* is 10mm and the diameter of the wire *D* is 0.36 mm.

$$N_{\mathrm{Bq}}^{\mathrm{DNR}} = \frac{\eta_s P}{\eta_b A} = \frac{\eta_s (4\pi R)}{\eta_b 2\pi^2 RD} = \frac{2\eta_s}{\eta_b D\pi} \tag{2.3.1}$$

The sensitivity of this instrument to interfacial contributions should be of the same order of magnitude as the ISR. However the ARG2 is significantly easier to run, provides higher time resolution, and avoids concerns over the needle dropping through the interface for low surface tension materials.

2.4. Micro-interfacial Rheometer (MIR)

An extension to currently employed interfacial rheology methods which use macroscopic probes to measure interfacial rheology is to employ microparticles as surface probes. The advantage of a micron sized surface probe is that the surface sensitivity is increased by several orders of magnitude over other methods. The idea of probing surface rheology using diffusing particles was initially investigated by Saffman for disks diffusing in biological membranes [Saffman 1976]. He found that the measured diffusion coefficient D_s' was related to the interfacial viscosity η_s by:

$$D_s' = \frac{k_b T}{4\pi\eta_s}\left[\ln\left(\frac{2\eta_s}{\eta_b a}\right) - \gamma_E\right] \tag{2.4.1}$$

$$2\eta_s >> \eta_b a$$

where R is the radius of the microparticle, k_b is the Boltzman's constant, T is the temperature, η_b is the subphase viscosity and γ_E is Eulers constant (0.5772). As shown, this relationship holds for cases where the surface contribution to the particle drag is large relative to the subphase contribution. While his original analysis assumed that the probes were flat disks within the membrane, this relation is also used for spherical particles (which by definition have a circular cross section at the interface) since the subphase contribution is assumed to be small.

Saffman's original analysis assumes that diffusion coefficients were measured from observing a single particle. Single particle measurements can be influenced by changes to the local microstructure in the neighborhood of the particles or if the material is inhomogeneous. Many surface films are observed to have a domain structure which might be locally inhomogeneous. Thus we use two-point measurements. These measurements are independent of the coupling between the tracer particle and the medium [Crocker et al. 2000]. This is especially important for interfacial measurements where there may be some localized distortion of the interface due to the particles.

Prasad and Weeks (2009) have employed particle tracer diffusion to measure the interfacial rheology of Dawn soap films. They generated thin soap films (thickness between 400-3000nm) and then observed the diffusion of fluorescent polystyrene tracer particles in the liquid phase. When the film thickness was less than four times the particle diameter, they were able to calculate the interfacial viscosity of the soap film using Saffman's relation to be 0.97 nPa-s-m or 9.7×10^{-7} mN-s/m. For thicker soap films, particle diffusion coefficients increased approaching bulk values. This is a result of having the tracer particles freely suspended in the liquid and not isolated at the interface. For thick films, the surface rheology dominates the observed particle diffusion, but for thicker films the particles diffuse around the bulk unhindered by the surface rheology.

Microrheology is a promising tool with a growing body of literature to support the development of this technique. Theoretical developments by Mason & Weitz (1995) noted thermal fluctuations of colloidal probe particles were directly related to the rheological properties of the surrounding medium. By statistically analyzing the diffusive motion of the probe particles, the full frequency dependent elastic and viscous moduli could be calculated. While this has only been implemented for bulk rheology, in principle, the same analysis methods could be applied to determine the full frequency dependent interfacial rheology as well [Squires & Mason 2010].

The previous methods have focused on using thermal fluctuations to probe the interfacial behavior, also known as passive microrheology. At Sandia, we also have access to optical trapping experiments which have the potential to perform active microrheology where we optically manipulate the tracer particle using focused laser light. Laser tweezers optical trapping has been demonstrated in bulk systems and has proven to be an accurate and flexible way to not only manipulate colloidal particles, but accurately measure interaction forces between particles with resolutions of up to 10 femtoNewtons [Grillet 2009]. Active microrheology using laser tweezers has been demonstrated at liquid-liquid interfaces by Park et al. (2008). Using direct force interaction measurements, they were able to determine the stabilizing mechanism for Pickering emulsions.

Based on the existing body of literature, we proposed to use passive and active microrheology to study interfacial rheology of air liquid system to better understand the link between interfacial rheology and foam stability. The main motivation for pursuing interfacial microrheology was the promise of improved surface sensitivity due to the small size of the probe. We define the Boussinesq number as:

$$N_{Bq}^{MIR} = \frac{\eta_s}{\eta_b R} \tag{2.4.2}$$

where R is the radius of the microparticle. In order to effectively measure interfacial properties, the Boussinesq number must be greater than 10. Figure 10 shows the Boussinesq number as a function of subphase and interfacial viscosities for a tracer particle radius of 0.5micron. For air-water interfaces, the potential sensitivity of the micro interfacial rheometer is η_s>5x10^{-6} mN-s/m – almost three orders of magnitude more sensitive than the ISR and AR-G2 rheometers. This also opens the possibility of making measurements with more viscous liquid phases. With a bulk phase viscosity of 1000 mPa (equivalent of a fairly viscous epoxy), MIR still has the potential to measure surface viscosities η_s>5x10^{-3} mN-s/m.

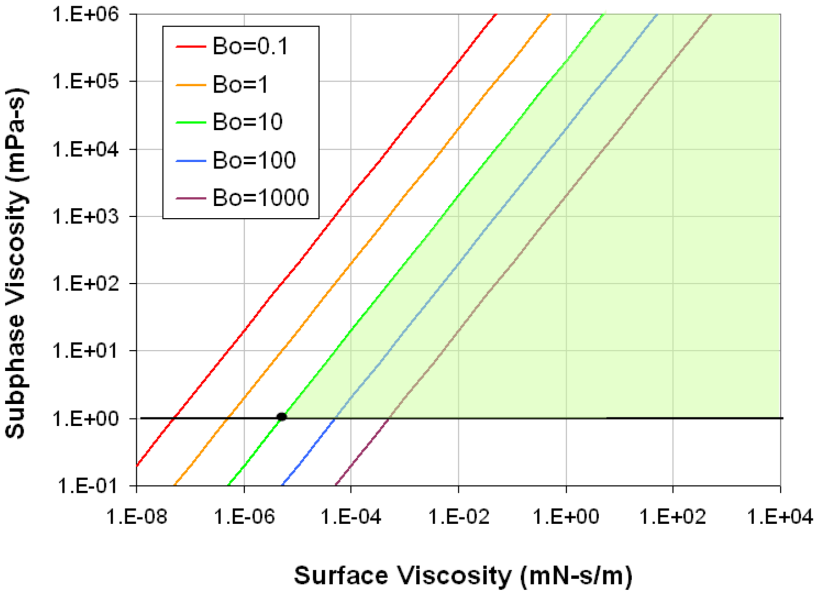

Figure 10: Bousinnesq number as a function of viscosity of the interface and bulk for interfacial microrheology

However there were several challenges of extending these microrheology methods to working with air-liquid interfaces. First was the difficulty of immobilizing particles at air-liquid interfaces. Particles need to be highly hydrophobic to be trapped at the interface. Second, air-liquid interfaces are less stable than liquid-liquid interfaces being very susceptible to evaporation and vibration. Finally, it was determined that there was an upper limit to surface viscosity measurements using micro interfacial rheology. We will now discuss each of these challenges in turn and finally present demonstration results for a Pluronic® surfactant system.

2.4.1. Particles at air-water interfaces

Particle stabilized emulsions or Pickering emulsions have been an active area of research, but it is far more difficult to suspend particles at air-water interface than at a liquid-liquid interface such as oil and water. Recent research has shown that interactions through the oil phase contribute significantly to the stability of the particles at the interface by introducing long range repulsions between the particles [Park et al. 2008]. Without those stabilizing forces, particles at the interface tend to aggregate. Also in oil-water emulsions, particles are drawn to and trapped at the interface when they are only moderately hydrophobic due to the presence of the hydrophobic layer. At an air-water interface, particle must be highly hydrophobic to remain at the interface as poor interactions with water are generally favored over no interactions in the air phase.

Since most available monodisperse microparticles have hydrophilic surface character, we have explored several methods of surface modification to keep the particles at the interface. First we explored grafting polydimethylsiloxane polymers onto silica microspheres. Polydimethylsiloxane is highly immiscible with water suggesting a high possibility of immobilizing the particles at the interface. However, it was very difficult to adequately rinse the microspheres. When a solution of particle and chloroform was deposited at the interface, visible surface contamination was generally observed. This problem was compounded by the fact that we later discovered that our vials were not compatible with the chloroform solvent and were degrading the material in the cap resulting in additional surface contamination. We also explored performing surface modification of silica microspheres with various end groups. By varying the end groups, we could vary the contact angle with water. The two we worked with extensively were octadecyltrichlorosilane (OTS) and aminopropyltriethoxysilane (APTES) which had contact angles with water of 90° and 40° respectively. Contact angles were measured on glass cover slides that received the same surface modification as the silica microparticles.

Images of these two surface modified particles suspended on a water-air interface are shown in Figure 11. The differences in the particle images are due to the fact that the particles have different contact angles and hence are located at different depths relative to the interface. The particles at the interface act as little lenses reflecting and refracting the light that hits them.

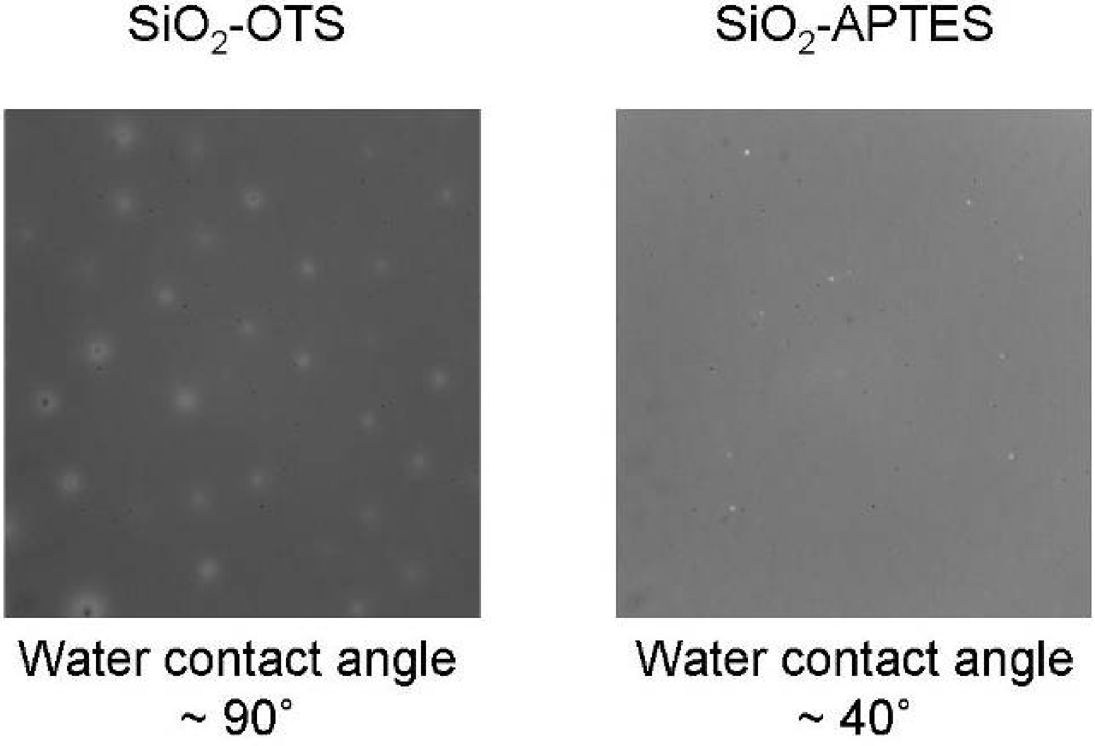

Figure 11: Images of surface modified silica microparticles at an air water interface.

To quantify more precisely the location of the particles in the interface, we performed Gellan fixation and scanning electron microscopy (SEM) of the particles [Park et al. 2008]. 2% Gellan solutions were heated to 90°C to completely dissolve the Gellan. There was difficulty in preventing a skin from forming on the Gellan before and during application of the microparticles. Thus the Gellan solution was pipetted into preheated Petrie dishes inside an oven and the microparticles were immediately deposited on the interfaces and left at 50°C for 5 minutes to equilibrate. The particle laden Gellan solutions were then cooled to room temperature to solidify the Gellan solution. Silicone elastomer (Dow Corning Sylgard 184) was then poured over the surfaces and allowed to cure overnight. The silicon layer was then carefully removed from the Gellan leaving the particle imbedded in the surface. These were then coated with platinum and imaged using scanning electron microscopy.

Scanning electron microscopy images of the various particles taken in backscatter mode are shown in Figure 12. Contact angles were measured on both sides of the particle and averaged over 3 separate particles at the interface. This method confirms that the surface coating does alter the position of the particle at the interface as expected from the contact angles measured on coated glass slides. However, the contact angles determined from the SEM images tended to be larger than the angles measured on the treated glass slides. This was perhaps due to differences in surface roughness of the particles, or possibly due to the evaporation of the chloroform solvent upon application of the microparticle solutions causing the formation of a skin preventing the particles from fully sinking into the Gellan solution. Alternately, impurities in the Gellan may have affected the interface though Gellan starch is widely considered not to be surface active

[Park et al. 2008].

Surface Treatment	SEM Contact Angle
Bare	84
APTES	88
OTS	102

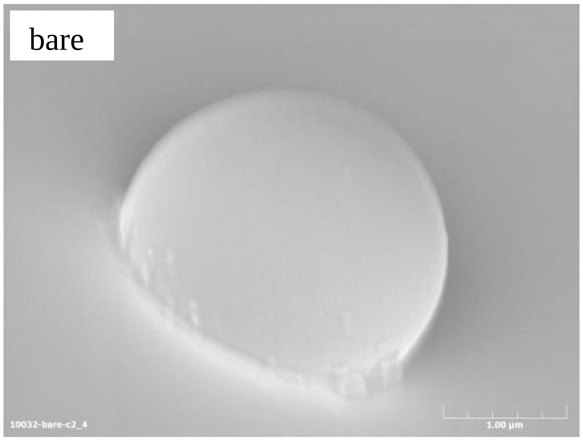

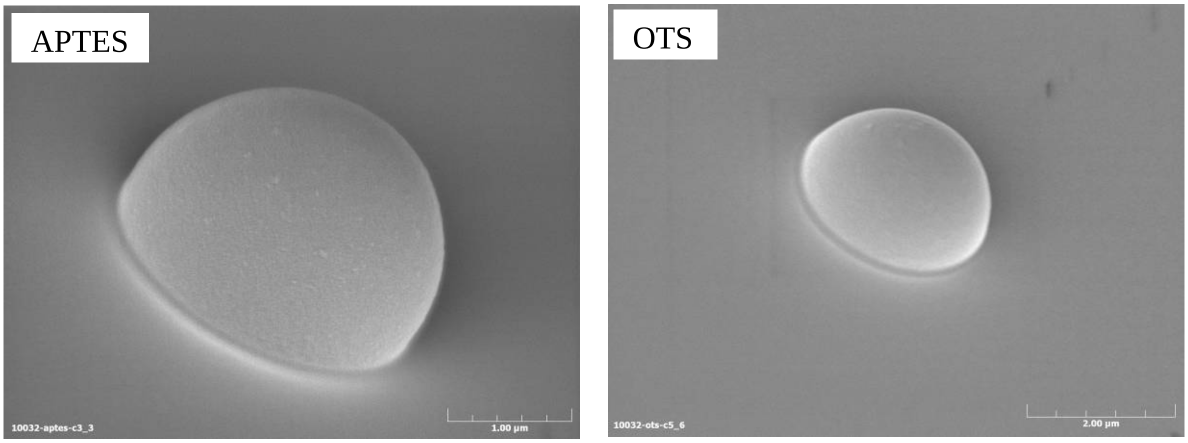

Figure 12: SEM Images of microparticles at air interface from Gellan imprint

An alternate method we explored for making particle which segregated to the interface was synthesizing Janus particles. This class of particle is named after the two-faced Roman god. The method we used followed the methodology of Takei & Shimizu (1997) as illustrated in Figure 13. Silica or fluorescent polystyrene particles were deposited onto a coverslip with low enough concentrations to ensure no overlap of particles. A conformal gold coating was applied to the top surface of the particle and then reacted with 10mM solution of 1-Dodecanethiol in ethanol. After 24 hours, the coverslips were gently rinsed and then sonicated to dislodge the particles from the coverslip. The particles were then rinsed 3 times with fresh ethanol. This generated particles which were hydrophilic silica or polystyrene on one side and coated with hydrophobic dodecane on the other. In principle, these particles should rest at the interface with a 90° contact angle. Additionally, the Janus morphology should prevent unwanted degrees of freedom at the interface such as particle rolling.

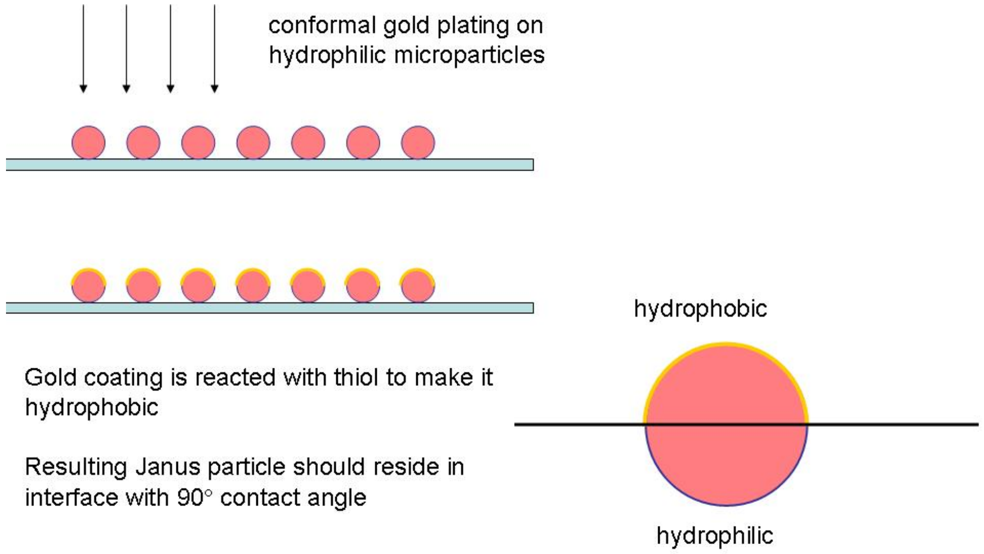

Figure 13: Schematic of synthesis procedure to make Janus Particles.

Once synthesized the fluorescent polystyrene based Janus particles were deposited on a glass slide to see if they were anisotropic. On the glass slide, the orientation of the particles was expected to be random. As shown in Figure 14, with transmitted light imaging, several clusters of the modified particles are visible. If we switch to fluorescence imaging of those same particles (as shown in the bottom image) some of the particles appear bright because the fluorescent face is pointed toward the camera where others only partially appear or are complete dark if the gold coated surface is towards the camera.

Next we needed to test that the particles would orient as expected at an interface. The fluorescent polystyrene based Janus particles were deposited on a Gellan interface from an ethanol solution and transferred to a PDMS layer as described above. As shown in Figure 15, the Janus particles aligned as expected with the fluorescent faces towards the hydrophilic phase and the hydrophobic faces towards the air interface. The Janus particles were developed late in the project, so we were not able to utilize them in our interfacial rheology measurements, but they are quite promising for interfacial investigations. The primary advantage is that the contact angle with the interface is fixed at 90° and should be independent of the surface tension. So the location of the particles at the interface shouldn't change with the addition of surface active materials. Also, as mentioned before, the Janus particles shouldn't roll at the interface whereas uniform particles have more degrees of freedom for their motion.

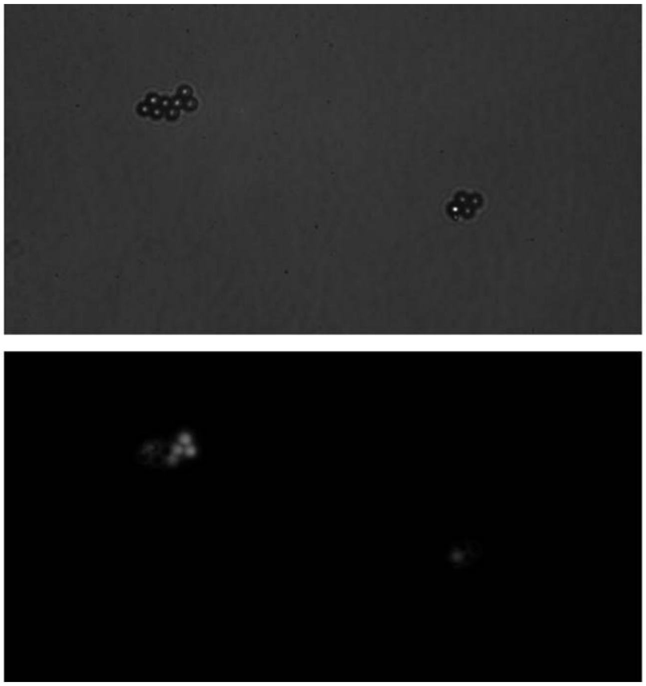

Figure 14: Fluorescent polystyrene Janus particles deposited on glass slide. In transmitted light imaging, several clusters of particles are visible. In fluorescent imaging on the bottom. some appear bright because the fluorescent face is pointed toward the camera where others only partially appear or are complete dark if part of the gold coated surface is towards the camera.

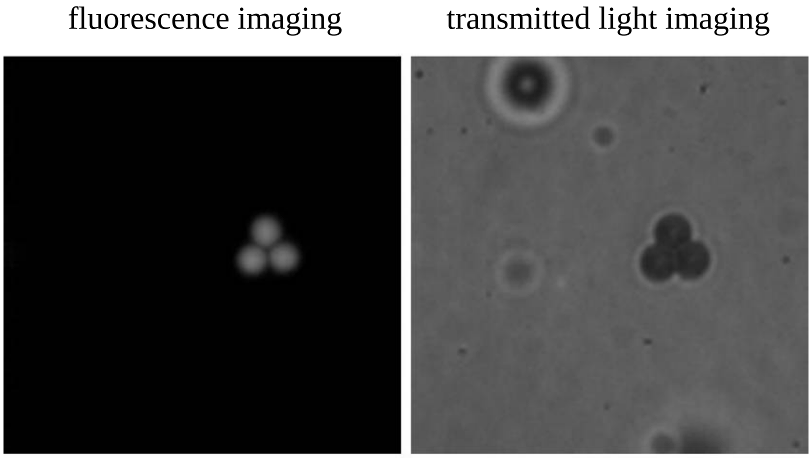

fluorescence imaging

transmitted light imaging

Figure 15: Imaging of fluorescent polystyrene Janus particles at an air-water interface.

2.4.2. Challenges of working at an air-water interface

Since our ultimate application was foams, we were specifically interested in making measurements at air-water interfaces. This would also allow us to work on the same systems that could be investigated with the other techniques previously discussed. However, these interfaces pose unique challenges for microrheology. First the interfaces are susceptible to vibrations. On the macroscale these are damped by capillary forces and not much concern, but for microrheology, even small deflections of the interface by several microns can ruin an experiment. All experiments were performed on a Newport vibration isolation table. Of additional concern were any forces which caused motion of the interface such as evaporation, room drafts or Marangoni stresses. Random flow currents at the interface were a continuing problem. We tried to minimize flow currents and evaporation by covering the testing apparatus with a cover containing a piece of moist cloth.

Our initial goal was to perform active microrheology using laser tweezers at the interface. However, that required very thin water layers (~200 microns thick) due to the working distance limitations of the high numerical aperture objectives required for good optical trapping. While we were able to make these thin layers by careful experimental preparation, these layers were not very stable. Additionally, we quickly discovered that trapping particles at air interfaces was very problematic. As discussed in Park et al. (2008), the refraction of the laser beam though the microparticles is critical to trap strength. While their analysis was for oil-water interfaces, the implications for air-water interfaces are clear. When the particle is imbedded in the interface, many of the light rays which would generate the trapping force get refracted or reflected inside of the particle by total-internal-reflection due to the large refractive index difference between the particle and air. This is exacerbated by the need to have highly hydrophobic particles which protrude far out of the water layer in order to be stable at the interface.

Figure 16 diagrams the laser tweezers optical trapping implementation as it was applied to particles at a liquid-air interface. The optical trap position in the view field was controlled using the acousto-optic deflector (AOD) and the particle was dragged along the interface by translating the microscope stage.

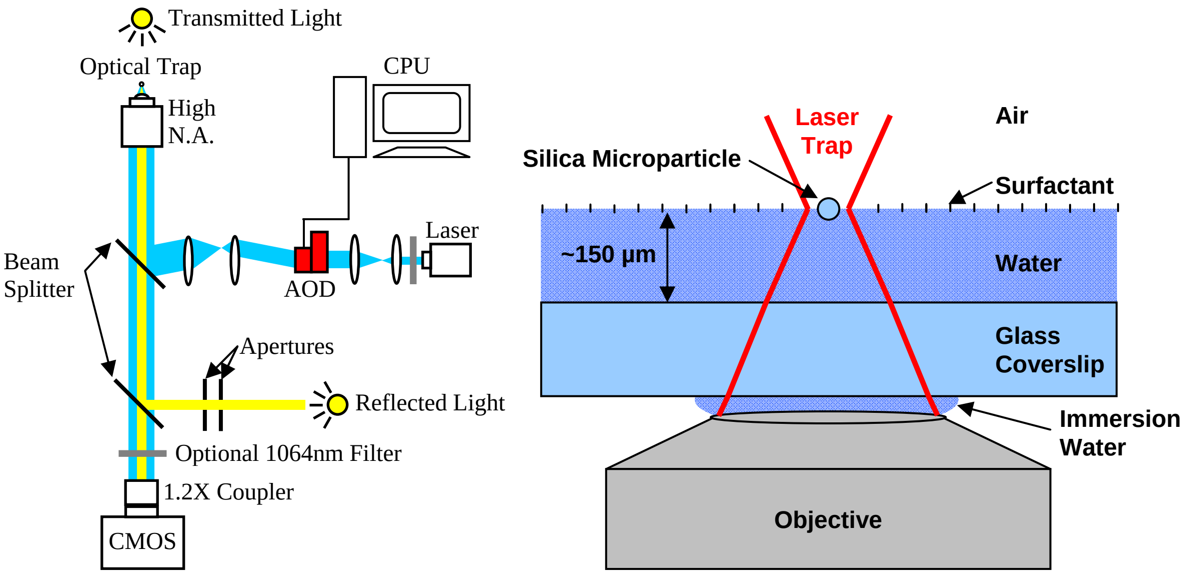

Figure 16: Schematic of active MIR. Acousto-optic deflector (AOD) moves the laser in the field of view of the microscope.

Figure 17 shows an image of a silica microparticle with a polydimethylsiloxane (PDMS) surface coating held in an optical trap. The particle could be translated through the surface at speeds up to 5 microns per second. While we have demonstrated trapping of particles at interfaces, the fragility of the very thin films needed and the poor quality of the optical trap caused us to focus our efforts away from active microrheology towards passive microrheology.

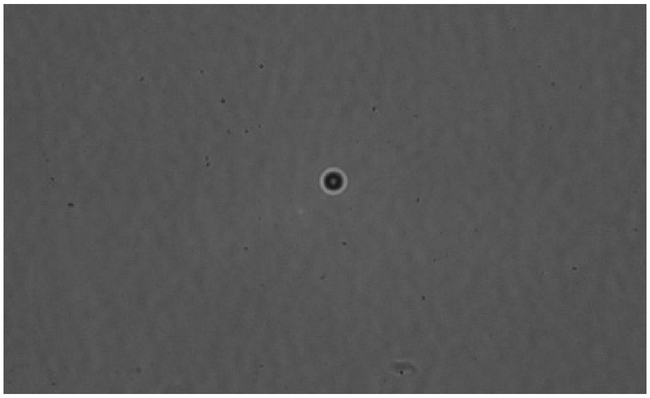

Figure 17: Silica microparticle with grafted PDMS coating held at an air-water interface in an optical trap.

2.4.3. Passive Micro Interfacial Rheology

For the last year of the project, we focused development of the micro-interfacial rheometer on passive techniques. With these techniques, we use thermal diffusion of the tracer particles to probe the interfacial rheology. Our methodology was to use the Saffman's relation, but use relative diffusion of two particles to measure the interfacial mobility as mentioned previously. Figure 18 illustrates the method. The change in the distance between two particle centers Δr is tracked as a function of time. The mean squared displacement $< \Delta r^2 >$ as a function of time is calculated from the width of the distribution in the change in particle separation, which increases linearly with time. The slope of that curve is the interface diffusion coefficient D'_s which is used to calculate the surface viscosity.

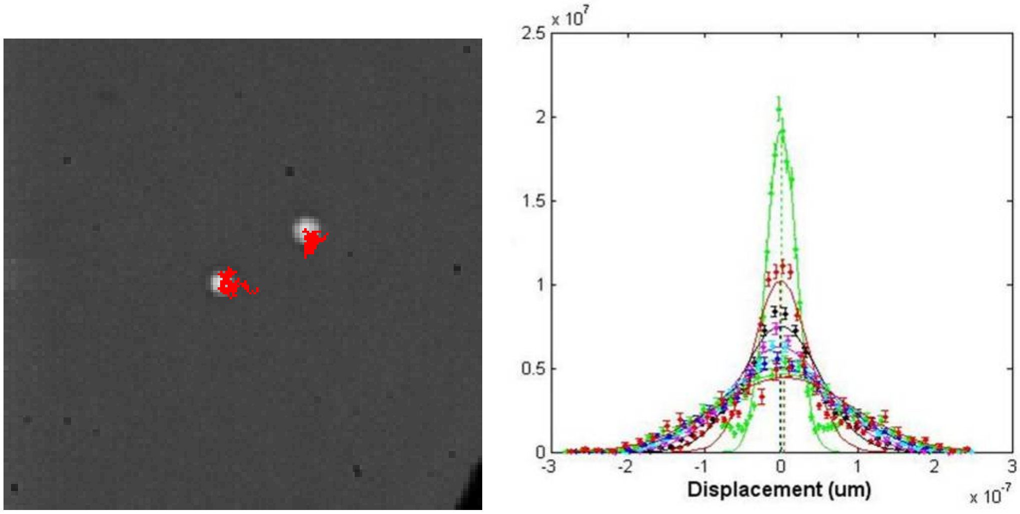

Figure 18: Image showing the tracking of a particle pair and the resulting measurement of Mean Squared Displacement (MSD) to determine diffusion coefficient and surface viscosity.

The limitation of passive methods is that the particles need to diffuse enough during the experimental window to measure the displacement. If the displacements are too small to measure (<0.1 pixel or ~20nm), the diffusion signal gets lost in the noise (mostly due to vibration or thermal fluctuations of the camera CCD). While we were able to make measurements when the surface viscosity was low, for very stiff interfaces such as for bovine serum albumin (BSA), the interface was so stiff that we couldn't measure the diffusion coefficient. Figure 19 shows mean squared displacement (MSD) as a function of time for several pair of particles on a 0.1wt% BSA solution. The MSD should increase linearly with time. When the interface has been aged 15 minutes, some diffusion of the particles is observed. If we fit a line to initial slope, we estimate a surface viscosity of 550nPa s m or 5.5×10^{-3} mN s/m. The measured displacements are at the limit of out spatial resolution so this should really be considered the upper limit of surface viscosity for this technique. It should also be noted that this value is not in good agreement with other measures of the surface viscosity for BSA interfaces. If the BSA interface is aged for 30 minutes, then no measurable diffusion of the tracer particles is measured.

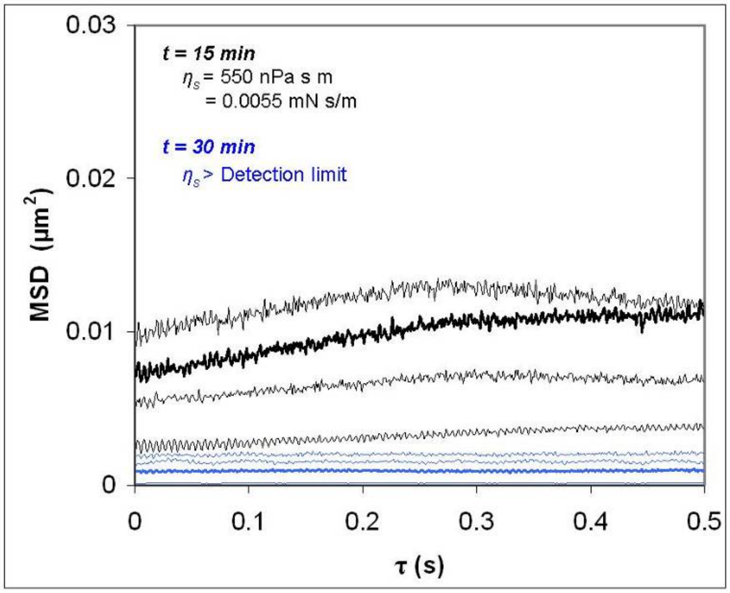

Figure 19: Mean Squared Displacement for 0.1wt% BSA with 2.5micron SiO_2-OTS.

2.5. Surface Dilatational Rheometer (SDR)

With the above instrumentation it is possible to create surface *shear* flows that occur at constant surface area. To study the rheological response to *dilatational* deformations (changes in area), we measure changes in the surface tension of an oscillating pendant drop. We have developed a surface dilatational rheometer (SDR) conceptually similar to designs created by others [Freer et al. 2003, Zholob et al. 2009, Ravera et al 2009]. The basic approach builds on the foundations of a pendant drop tensiometer, where surface tension is measured by fitting the shape of a hanging drop to a solution to the Young-Laplace equation of capillarity (equation 2.5.1)[1]:

$$\Delta P = \sigma\left(\frac{1}{R_1} + \frac{1}{R_2}\right) \tag{2.5.1}$$

where ΔP is the difference in pressure across the interface, σ is the surface tension, and R_1 and R_2 are the principle radii of curvature. In this class of devices, the volume of the droplet is forced to oscillate, which causes sinusoidal variations in the surface area, A, at a frequency ω. The changes in surface tension with surface area are measured from the drop profiles and are used to determine the dynamic surface dilatational modulus, $K_s^*(\omega)$, defined as:

$$A\frac{\partial \sigma}{\partial A} = K_s^*(\omega) = K_s^{'}(\omega) + iK_s^{"}(\omega) = \left|K_s^*(\omega)\right|\cos\delta + i\left|K_s^*(\omega)\right|\sin\delta\,. \tag{2.5.2}$$

---

[1] See Appendix A for a more detailed discussion of how to measure the surface tension from a pendant drop image.

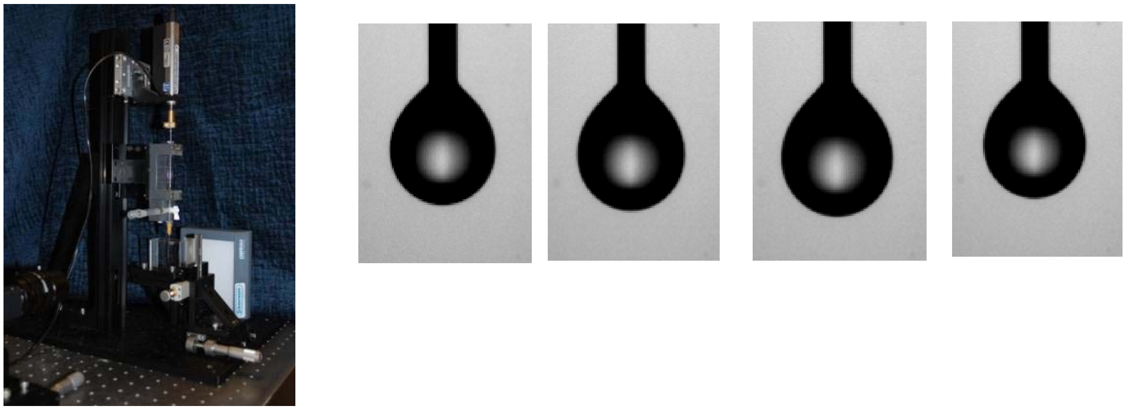

Figure 20: Surface dilatational rheometer (SDR) (left) and close-ups of an oscillating drop (right).

The dilatational modulus *K* is analogous to a bulk modulus, which measure a material's resistance to a uniform compression.[2]

The SDR uses the pendant drop technique to measure changes in surface tension of an oscillating droplet or bubble (Figure 20). We generate a time-dependent surface area, *A*, by varying the drop volume through the use of a microsyringe (1710RN 100 microliter Hamilton gastight syringe with a Nordson EFD PTFE-coated syringe tip (ID: 0.33 mm)) driven by a robust mechanical actuator (Newport HS-LTA). The actuator is programmed to deliver a sinusoidal stroke. The resulting changes in surface tension are analyzed to measure an effective surface dilatational modulus (equation 2.5.2) $K_s^*(\omega)$, with storage and loss moduli analogous to those in equation 2.2.1 for the surface shear modulus. Figure 21 shows time plots of Bond number, radius of curvature at the apex of the drop, surface tension, volume, and surface area from a representative drop oscillation experiment on the SDR.

After removing background drift, the surface tension (σ) and surface area (*A*) are fit to a sinusoidal function at the same frequency as the applied volume forcing.

$$\sigma(t) = \sigma_0 + \Delta\sigma \sin(\omega t + \psi_\sigma) \qquad (2.5.3)$$

$$A(t) = A_0 + \Delta A \sin(\omega t + \psi_A) \qquad (2.5.4)$$

where ω is the forcing frequency, σ_0 and A_o are the offset, $\Delta\sigma$ and ΔA are the amplitude, and ψ_σ and ψ_A are the phase angle for the surface tension and surface area, respectively. Eqn. 2.5.2 can be rewritten in terms of these fitting parameters to determine the dynamic surface dilatational modulus:

$$A\frac{\partial\sigma}{\partial A} = K_s^*(\omega) = \Delta\sigma \frac{A_0}{\Delta A}\exp[i(\psi_\sigma - \psi_A)]. \qquad (2.5.5)$$

---

[2] In the literature it is commonplace to use "E_s" to represent the surface dilatational modulus. However, to avoid making the incorrect analogy with the bulk tensile (Young's) modulus, which is typically referred to as "*E*", we choose to use K_s. This makes a natural connection between the surface dilatational modulus and the bulk modulus in 3D, which is typically referred to as "*K*".

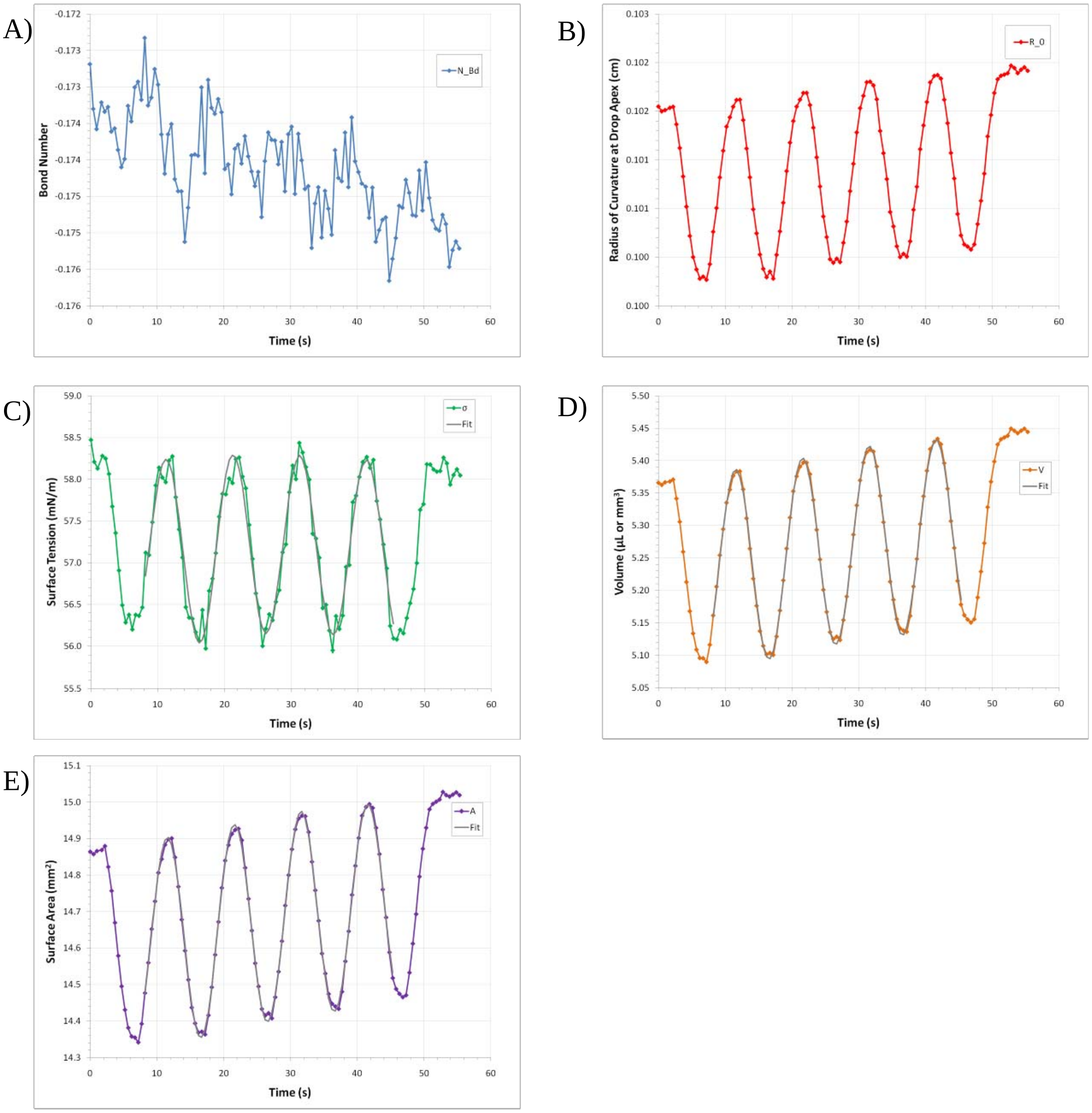

Figure 21: Results from processing a series of pendant drop images. Two of the drop fitting parameters, the Bond number and the radius of curvature at the apex, are shown in A and B. The calculated surface tension from eqn. A.13 is shown in C. The drop volume and surface area are shown in D and E, respectively. Curve fits to the sinusoidal portions of the surface tension, surface area, and volume are also plotted.

The SDR has the flexibility to examine droplets that are more dense (hanging) or less dense (rising) than the surrounding phase (Figure 22). We achieve this by using different needle attachments. We use a standard straight tip for hanging drops and custom needles bent into the shape of a hook for rising bubbles (e.g. air bubbles immersed in a liquid).

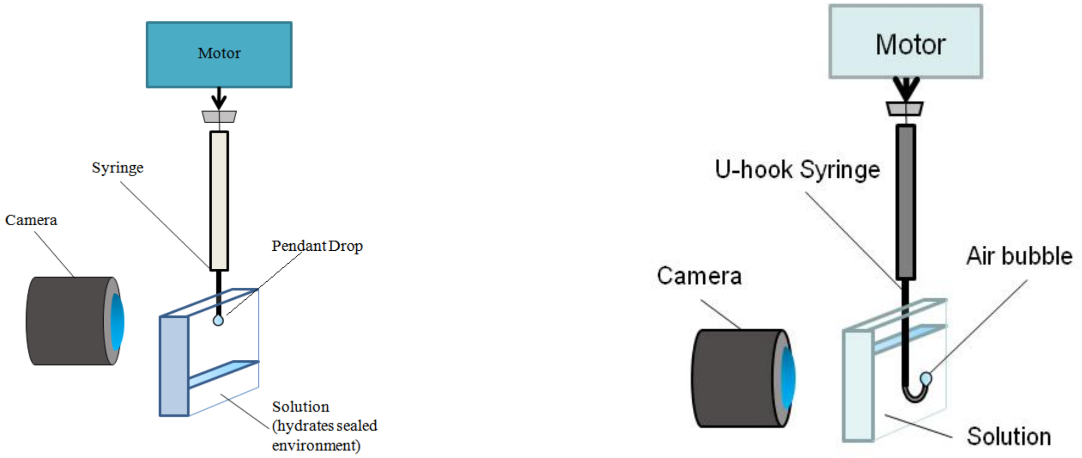

Figure 22: SDR showing capability to make either a liquid drop in air or a bubble in liquid. The bubble method allows testing with a large reservoir of surfactant solution.

3. INTERFACIAL RHEOLOGICAL STUDIES

We have applied this new instrumentation to a wide array of surface active materials including surfactants, proteins and polyelectrolytes. The surfactants chosen included a variety of types and, in some instances, several concentrations. Two families of nonionic surfactants were included: a block copolymer based on ethylene oxide and propylene oxide (Section 3.1) and an ethylene oxide attached to an alkane chain (Section 3.2). These surfactants were later tested in foaming-defoaming studies presented in Section 4.

In the next subsection we discuss the effects of varying molecular weight of the hydrophobe and fraction of hydrophile. In Section 3.2 we describe a study designed to connect surface dilatational rheology with surfactant diffusion of ethylene oxide to and from the air-liquid interface. Also tested in the foaming studies were several proteins. The surface rheology of these proteins is discussed in Section 3.3. In Section 3.4 we describe tests with a polyelectrolyte-surfactant mixture. Polyelectrolytes consist of charged monomer units, and when these are mixed with oppositely charged surfactants, they exhibit widely varying behavior that is not yet well understood. Finally, a brief study of the interactions among particles and surfactants is included in Section 3.5 and some results from examining body wash samples from a commercial vendor are included in Section 3.6.

In addition to developing a better understanding of surfactant behavior, these studies also show the sensitivities of the new instrumentation and demonstrate that a range of instrumentation is needed to measure various surfactant solutions because of these sensitivities.

3.1. Pluronic® Surfactants

Pluronic®(BASF), or poloxamers, are a class of surfactants that are ABA block copolymers with a central block (B) of propylene oxide and end blocks (A) of ethylene oxide. Depending on the molecular weight of the hydrophobic propylene oxide block and the ethylene oxide block they can be tailored for use as detergents, foaming and defoaming agents, emulsifiers, and wetting agents (Figure 23). We chose to examine the surface rheology of two surfactants from this class of materials that had widely differing behavior: F108 (foaming agent, MW=14600 g/mol, 3000 g/mol propylene oxide block, 80 wt.% ethylene oxide) and L31 (defoaming agent, MW=1100 g/mol, 900 g/mol propylene oxide block, 10 wt.% ethylene oxide). Because of their polymeric nature, a portion of the Pluronic® F108 attached to the interface is adsorbed irreversibly, whereas the L31, having a lower molecular weight, adsorbs and desorbs more freely [Svitova et al. 2003]. Both materials were examined as aqueous solutions at a concentration of 1 mM.

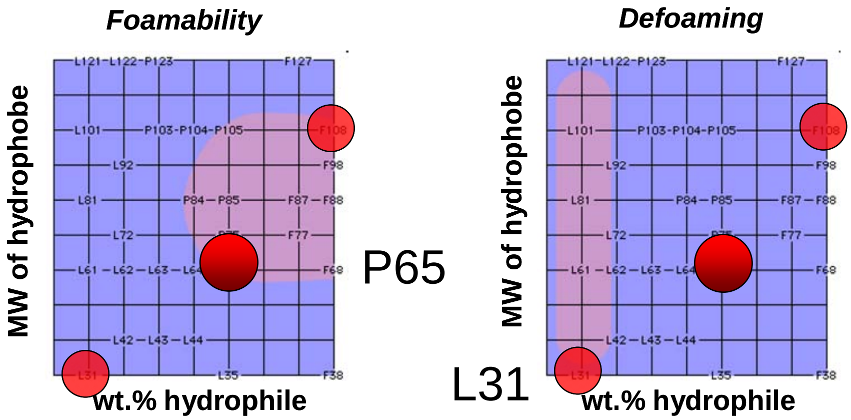

Figure 23: Formulations of block copolymers studied marked by red circles. Purple shaded areas mark formulations of foaming agents (left) and defoamers (right) from manufacturer information (BASF).

3.1.1. Surface Tension and Dilatational Rheology

The dilatational rheology was measured with the SDR by creating an air bubble immersed in the Pluronic® solution or a hanging droplet of the Pluronic® solution in air. Experiments with air bubbles and liquid drops were performed at different times and different protocols were used. For air bubble measurements, an initial air bubble was created and the surface tension monitored for 1000 s prior to oscillating the drop over a range of frequencies. For liquid droplet measurements, oscillations were fixed at 0.5 Hz.

The surface tension response for F108 and L31 are shown in Figure 24 and Figure 25. Both experiments started out with initial values of 44-45 mN/m. The surface tension value for pure water, 72.8 mN/m, could not be detected since the surfactant can rapidly adsorb to the newly created surface. The long time response, however, showed markedly different results depending on whether an air bubble or droplet configuration was used. The liquid drop appeared to level off at much higher surface tension values than the air bubble. One potential explanation is that for the droplet configuration the amount of surfactant in the bulk is limited. Listed in Table 1 are typical properties of the bubbles/droplets used in these experiments, and these values indicate that there is a 4-order of magnitude difference in the ratio of the air-liquid interfacial area to the solution volume. If this is the reason for the difference, we suspect that in our liquid droplet experiments the concentration of the surfactant in the droplet is well below 1 mM because a large proportion adsorbs to the air-liquid interface.

It is also important to note that the long time values of the surface tension in our bubble experiments do not agree with the results from Svitova et al. 2003 or with product information on the BASF website. In the work by Svitova, 40±5 µL air bubbles were used, and for 1 mM L31 and 0.01 mM F108 the surface tension was ~43-47 mN/m at ~600 s. BASF reports the surface tension of 0.1 wt.% solutions of L31 and F108 to be 46.9 and 41.2 mN/m, respectively. It is possible that the difference we observed in our air bubble and droplet measurements could be due to contamination. In fact, when compared to these other sources, the droplet measurements appear to be more consistent.

Table 1: Typical Dimensions of Bubbles/Droplets Used in Dilatational Rheology Experiments of Pluronic® Surfactants

	Air Bubble	Liquid Drop
Gas Volume (μL or mm^3)	1-3	50,000
Solution Volume (μL or mm^3)	50,000	6-7
Surface Area (mm^2)	5-10	15-18
S/V Ratio for Solution (1/mm)	0.0001-0.0002	2-3

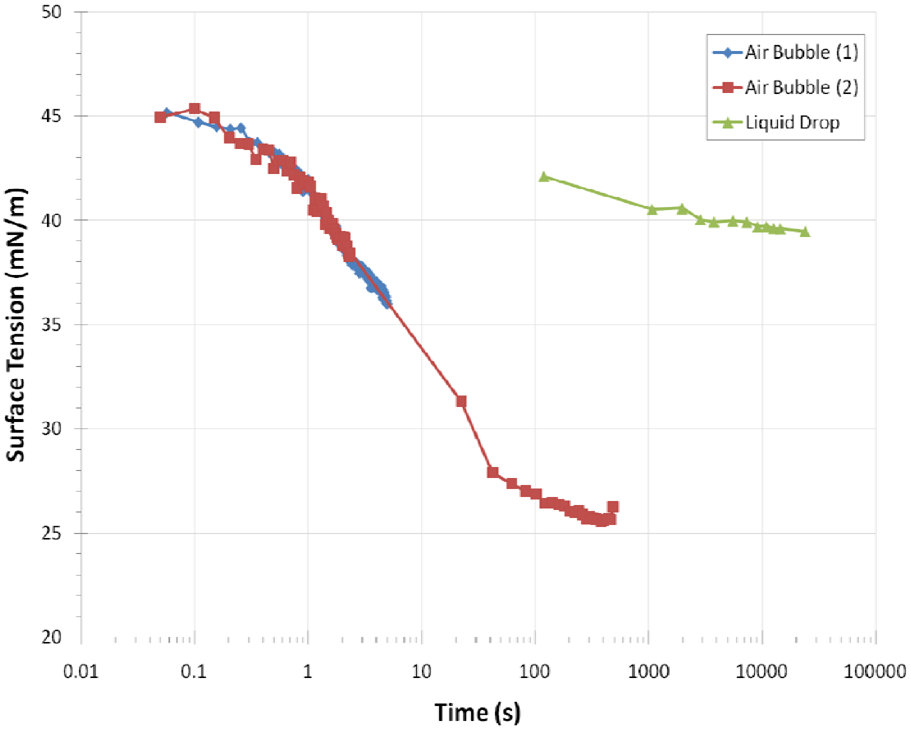

Figure 24: Comparison of the evolution of the surface tension of an air bubble and a liquid drop for a 1 mM F108 solution.

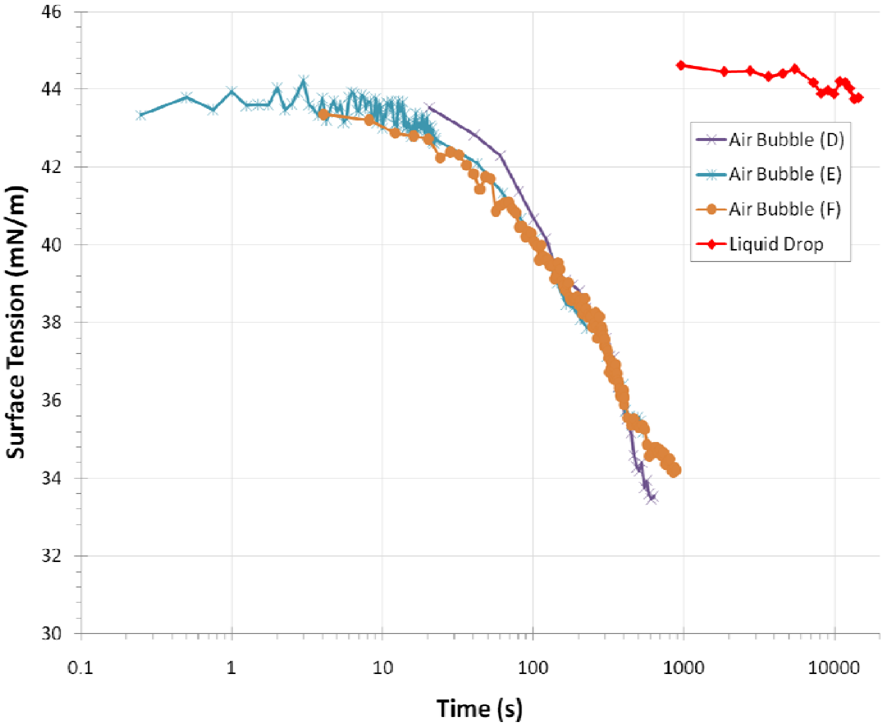

Figure 25: Comparison of the evolution of the surface tension of an air bubble and a liquid drop for a 1 mM L31 solution

For F108, the dilatational rheology of the air bubble and droplet at 0.5 Hz is shown as a function of surface tension in Figure 26. In the droplet experiments, the surface dilatational modulus is in the range of 8-18 mN/m, appears to have a linear dependence with surface tension, and is predominantly elastic (δ~20°). At 1000 s the air bubble has a higher modulus (43 mN/m) and is more viscous (δ~57°). The bubble was also subjected to oscillations over a range 0.01 to 1 Hz with dilatational strains ranging from 0.052 to 0.063 (Figure 27). The dynamic dilatational moduli exhibit a square root dependence on frequency, with the surface behaving slightly more viscous than elastic (tan 55^{o} = 1.4).

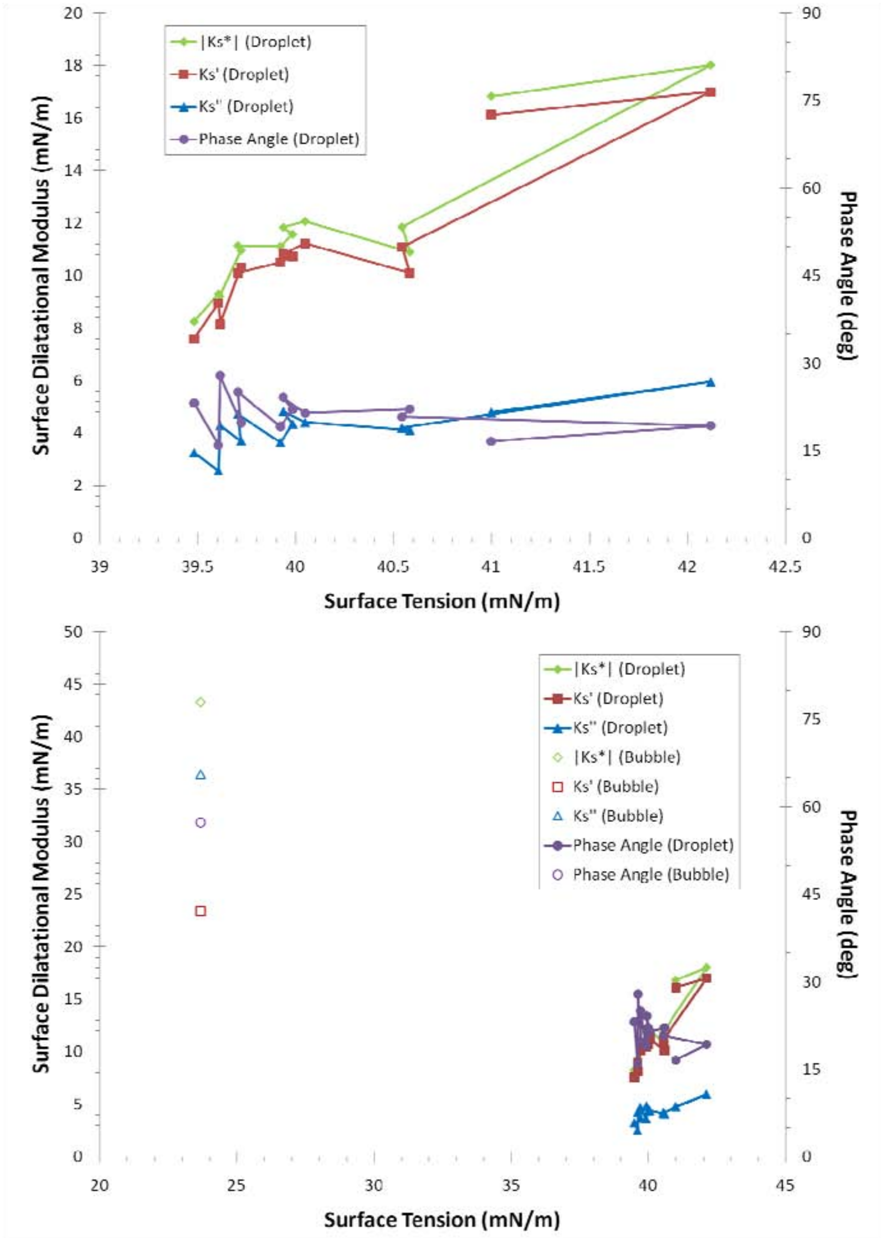

Figure 26: Surface dilatational rheology of a 1 mM F108 solution at 0.5 Hz. Area strains were 1.8-1.9% for the liquid drop, 5.2-6.4% for the air bubble.

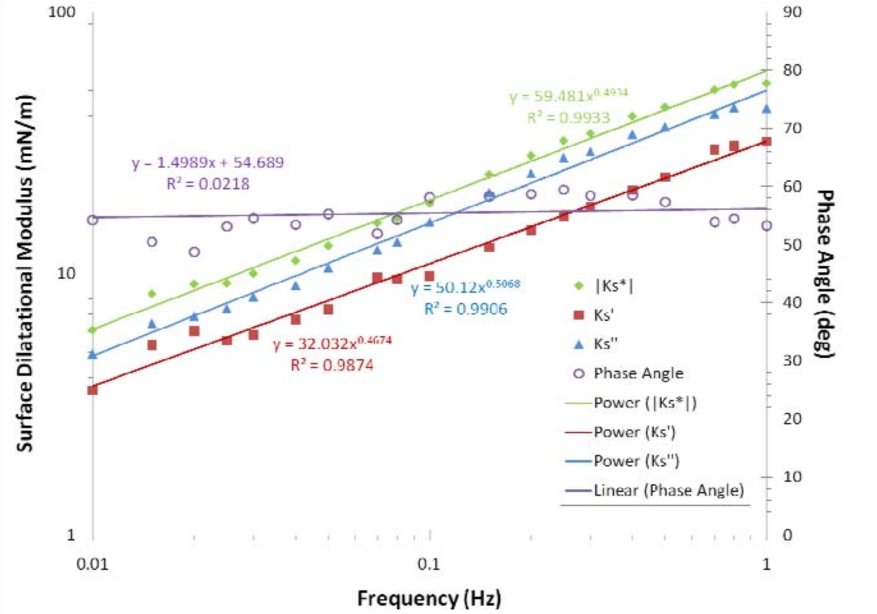

Figure 27: Surface dialtational rheology of a 1 mM F108 solution in contact with an air bubble after 1000 s. σ=23.5-23.8 mN/m during these measurements.

Results from examining the dilatational rheology of L31 at 0.5 Hz are presented in Figure 28. The droplet experiments show the surface dilatational modulus is 6.0 mN/m and is very elastic (δ~9°) within a surface tension range of 39.5-42.0 mN/m. Results from the air bubble experiments show extremely strange behavior, with the surface dilatational modulus in the range of 160-220 mN/m and a phase angle of δ~180°. Figure 29 is a plot of the surface tension and surface area oscillations that clearly demonstrate this out of phase behavior. The phase angle is expected to be in the range of 0-90°. Phase angles of 180° are typical in the cases where inertia dominates the response. In this case it is difficult to reason that it is the fluid inertia, however, since this type of behavior was not observed with an air bubble in F108 (which had an even lower modulus), and is never observed for pure water. This behavior was repeated with several air bubbles and was consistent over a frequency range of 0.01 to 1 Hz, with phase angles from 160 to 200° (Figure 30). Perhaps we have a coupling between the bulk diffusion and adsorption mechanisms that can give this type of behavior. The L31 does not form an irreversibly adsorbed layer like F108 [Svitova et al. 2003]. This is a surprising result that is yet to be fully explained.

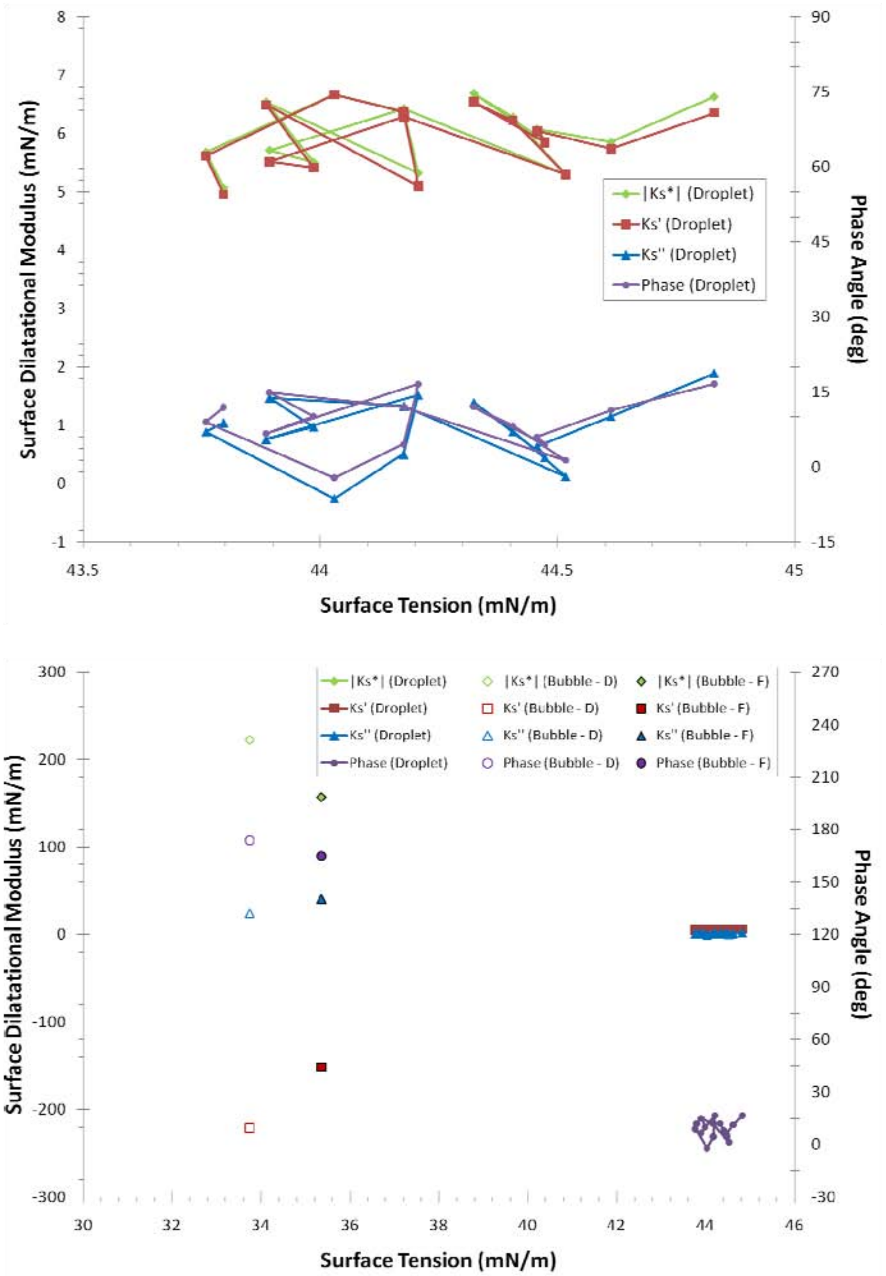

Figure 28: Surface dilatational rheology of a 1 mM L31 solution at 0.5 Hz. Area strains were 1.7-1.8% for the liquid drop, 0.21-0.94% for the air bubble.

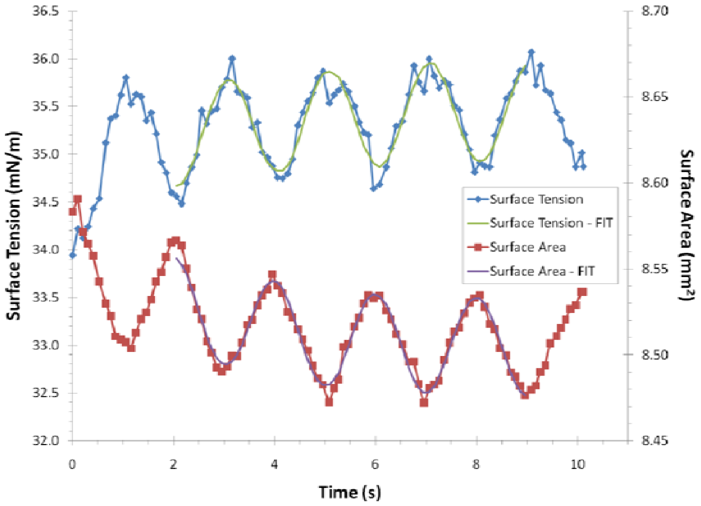

Figure 29: Response of the surface tension and surface area for the 0.5 Hz oscillation of an air bubble immersed in 1 mM L31.

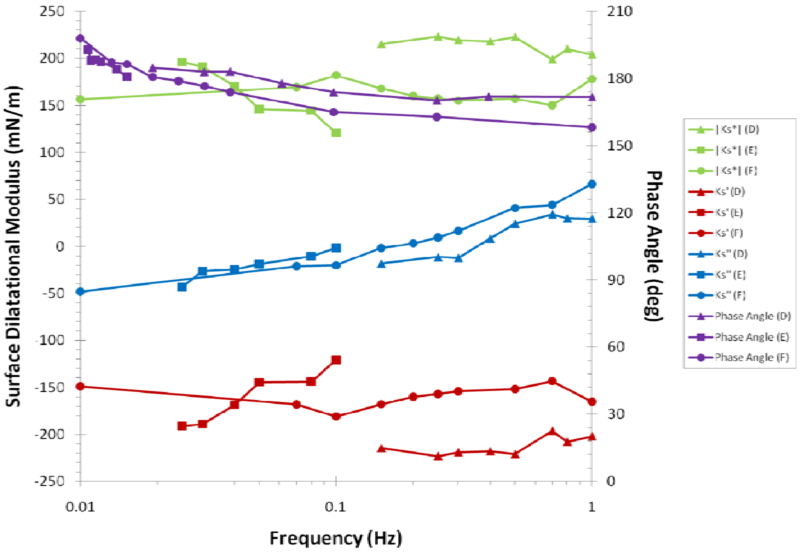

Figure 30: Surface dialtational rheology of a 1 mM L31 solution in contact with an air bubble after 1000 s. The surface tension for D (31.2-34.3 mN/m), E (31.5-36.0 mN/m), F (33.8-35.6 mN/m).

Since our two sets of measurements were performed by different personnel on samples prepared at different times, it is highly recommended that these measurements be repeated in a more consistent context to be able to make any firm conclusions. Initial work should focus on measuring the surface tension of numerous concentrations of Pluronic® with the air bubble and liquid drop configurations over at least a half hour (1800s) to test the surface-to-volume ratio hypothesis. Once this is characterized, the evolution of the dilatational modulus at fixed frequency (e.g. 0.5 Hz) should be measured with time to identify if and/or when the phase angle crosses over to 180°. Frequency sweeps should only be conducted when the surface is relatively stable (i.e. at long times) or by repeating the evolution experiment at different frequencies.

3.1.2. Shear Rheology

The Pluronic® surfactant 1 mM F108 (BASF) was tested using the ISR and MIR. The ISR could not detect any appreciable rheology (dynamic shear moduli < 0.01 mN/m) of the Pluronic®. However, MIR offered greater surface sensitivity and results are shown in Figure 31 for an 1 mM F108 interface aged by 15 minutes. The MIR was operated using 2.47 micron OTS coated silica microparticles because the measured contact angle at the liquid-air interface was approximately 90 degrees. The MSD was determined as a function of time for three particle pairs separated by a distance, *R* ~ 14 microns. The average slope of the three curves, 0.14 micron^2/s, is used to iteratively solve Saffman's equation for an effective surface viscosity, η =11 nPa·s·m or 0.00011 mN·s/m.

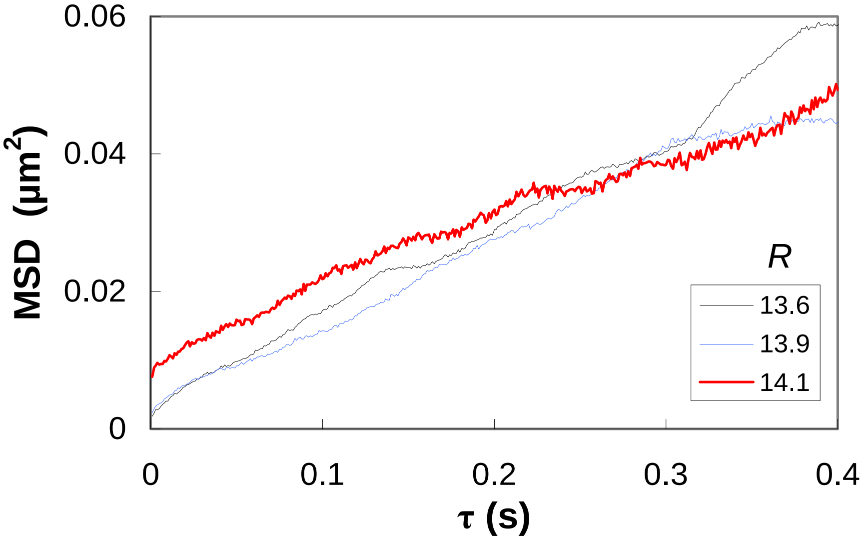

Figure 31: MIR results showing the mean squared displacement of 2.5 micron OTS-coated silica particles spread on a 1mM F108 interface aged for 15 minutes. Each line represents a different pair of particles separated by a distance R, measured in microns. The average slope of these curves is used to iteratively solve Saffman's equation for an effective surface viscosity, η = 12 nPa·s·m or 0.00012 mN·s/m.

3.2. Octaethylene glycol monododecyl ether ($C_{12}E_8$)

Using the pendant-drop technique of the SDR, we measured the surface tension and dilatational rheology of two different concentrations of the nonionic surfactant, $C_{12}E_8$. Single-step compressions and oscillatory measurements over a range of frequencies were compared and correlated for the purpose of inputting into a yet-to-be developed model that includes a diffusive flux term. Here, we show that the single-step compression tests are adequate and simple replacements for probing the interfacial rheology, and thus the complexity of modeling an oscillating interface can be avoided.

3.2.1. Background

The dynamics of surfactant adsorption have been an area of significant research activity for decades, and with the advent of digital imaging, the pendant-drop technique has become a widely used one. Thus in the past decade, there has been a strong drive toward understanding interfacial rheology in the context of surfactant adsorption dynamics, and this work seeks to reinvestigate the issue for the well-studied system of octaethylene glycol monododecyl ether, or $C_{12}E_8$.

There already exist several detailed descriptions of the adsorption activity of this and similar systems at an interface [Tsay et al. 1997, Lin et al. 1999, Gottier et al. 1986, MacLeod & Radke 1994, Pan et al. 1998, Liggieri et al 1999], and as such, we do not suggest that this work in its current state is finished; much of what we set out to do remains to be completed (with respect to modeling surfactant behavior at the interface). Specifically, it is well known that for a fluid interface coated in surfactant, compression and expansion of the interface will result in surfactant exchange with the bulk coupled with a change in the surface tension [Gottier et al. 1986, MacLeod & Radke 1994, Pan et al. 1998]. Measuring this exchange is trivial if one assumes that conformational changes in molecules at the interface either do not happen or do not affect the tension; however, this may be incorrect, as indicated by Liggieri, et al. (1999). Any molecular interactions at the interface would very likely result in an apparent rheological response, so it is important that this behavior be identified should it exist.

Thus, this work seeks to compare two different tests of interfacial elasticity (single-step compression/expansion as well as small-amplitude oscillatory measurements) and model the resulting behavior. Recently, work by Alvarez, et al. elucidated the limiting factors and applicable ranges for both the pendant-drop tensiometer and microtensiometer, concluding that in some cases surfactant dynamics can be diffusion-limited or kinetically limited, depending partially on the size of the drop [Alvarez et al. 2010]. For this work, a diffusion-limited model coupled with convection should adequately describe behavior at the air-liquid interface, and presumably deviations from this model would be the result of intermolecular interactions or rearrangements

Surface elasticity, or the response of a surface tension to deformation, can be determined using a pendant-drop setup in conjunction that allows for an oscillating drop size [Svitova et al. 2003, Tsay et al. 2004, Hsu et al. 2000]. This elasticity is called the Gibbs elasticity, and is defined as:

$$K_s = \frac{\partial \sigma}{\partial \ln A} = A\frac{\partial \sigma}{\partial A} \tag{3.2.1}$$

An oscillating drop will have both real and imaginary parts to the surface tension response:

$$K_s^* = K_s^{'} + iK_s^{''} \tag{3.2.2}$$

$$K_s^{'} = \Delta\sigma \frac{A_0}{\Delta A}\cos\delta \tag{3.2.3}$$

$$K_s^{''} = \Delta\sigma \frac{A_0}{\Delta A}\sin\delta \tag{3.2.4}$$

In this setup, the volume of the bubble oscillates according to a sine wave at some frequency ω, and the elastic (K_s', in-phase) and viscous (K_s", out-of-phase) components sum according to equation 3.2.2.

A single-step compression or expansion follows the same expression as in equation 3.2.1, except that a time-dependent relaxation modulus is measured from the response. However, it is far simpler to model single-step tests and then translate into frequency space rather than attempt the inverse. Thus, to calculate an elasticity from single-step data, a low amplitude region of a resulting surface tension versus time curve was selected, fit to a line, and normalized to yield a relevant frequency and elasticity. An example is shown in the materials and methods section.

3.2.2. Materials and Methods

For this work, we utilized a pendant-drop setup, as shown in the schematic in Figure 32. A Newport LTA series motorized actuator was connected to a 1710RN 100 microliter Hamilton gastight syringe, with a Nordson EFD PTFE-coated syringe tip (ID: 0.33 mm). The syringe was filled with solution and drops were suspended from the tip into a sealed cuvette. The cuvette contained a small amount of solution such that the drop environment would be well hydrated and convective evaporation would not affect the measurement. Backlighting was achieved with an LED spotlight and images were collected with a Basler 622fm monochrome firewire camera in conjunction with a zoom lens purchased from Edmund Optics.

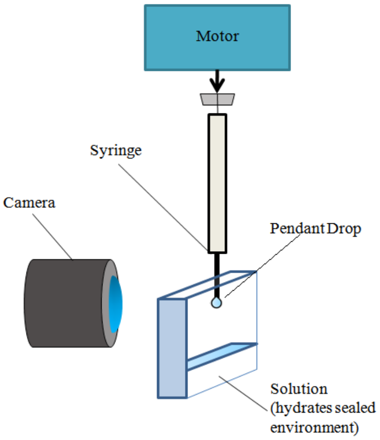

Figure 32: Schematic of pendant-drop setup

For each set of data, a drop was first formed at the end of the syringe tip and allowed to equilibrate for several thousand seconds. We confirmed our equilibrium surface tension values by utilizing Frumkin equation of state values as reported in the literature [Tsay et al. 1997]. When equilibrium was achieved, we then either performed a series of oscillatory tests or a series of single-step compressions and expansions. For the oscillatory tests, the linear actuator was moved in a sinusoidal fashion, which then retracted or expanded the drop according to a set amplitude and frequency. Amplitudes were maintained at less than five percent of the total drop area, so as to prevent a nonlinear rheological response. For single-step compression or expansion runs, a drop was retracted or expanded by a set volume at a variety of speeds. In order to save time, after a single step, the drop was returned to the original size and equilibrium was re-achieved (the alternative being compression or expansion to the point where the drop is destroyed and a new drop must be formed). This was performed for two separate concentrations, 6.25×10^{-3} mol/m^3 and 1×10^{-2} mol/m^3 (6.25 µM and 10 µM)

Drop images were post-analyzed using software developed in LabVIEW First, images were passed through a edge detection algorithm, and drop profiles were fit to the Young-Laplace equation as described in Appendix A and demonstrated in several other publications [Tsay et al. 1997, Lin et al. 1995, Lin et al. 1996]. For oscillatory measurements, surface tension and area versus time data were each fit to sine waves, and the phase and amplitude were used to calculate the Gibbs elasticity. The analysis of single-step compressions or expansions was briefly explained in the introduction, and an example is shown in Figure 33.

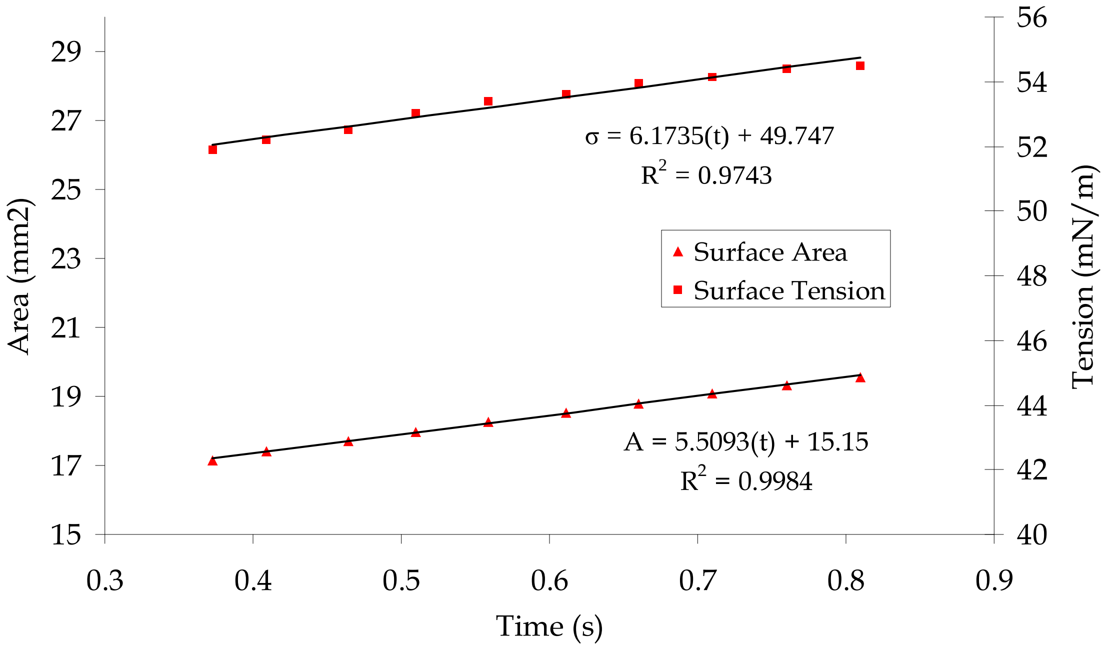

Figure 33: Surface tension and surface area versus time for a single-step drop expansion of 6.25×10^{-3} mol/m^3 (6.25 µM) $C_{12}E_8$ in DI water.

For this test, a drop of 6.25×10^{-3} mol/m^3 of $C_{12}E_8$ was suspended from the syringe tip, and compressed at a rate of 5.51 mm^2/s (that is, the resulting area compression rate when the drop was pulled inward by the syringe pump). The tension increased at a rate of 6.17 mN/m s, and the data was normalized accordingly:

$$V_R = \frac{\dot{A}}{A_0} [=] \frac{1}{s} \tag{3.2.5}$$

$$V_{TR} = \frac{\dot{\sigma}}{V_R} [=] mN/m \tag{3.2.6}$$

$\dot{A}$ is the rate of change in the interfacial area, 5.51 mm^2/s, A_0 is the initial area, and $\dot{\sigma}$ is the rate of change in the surface tension, 6.17 mN/m s. The resulting V_R is in units of frequency, and

V_{TR} is in units of mN/m (elasticity). In this case, V_R is about 0.35 s^{-1}, and V_{TR} is about 20 mN/m.

3.2.3. Results

Figure 34 shows a series of some of the single step compression-expansion tests for a solution of 6.25×10^{-3} mol/m^3 of $C_{12}E_8$.

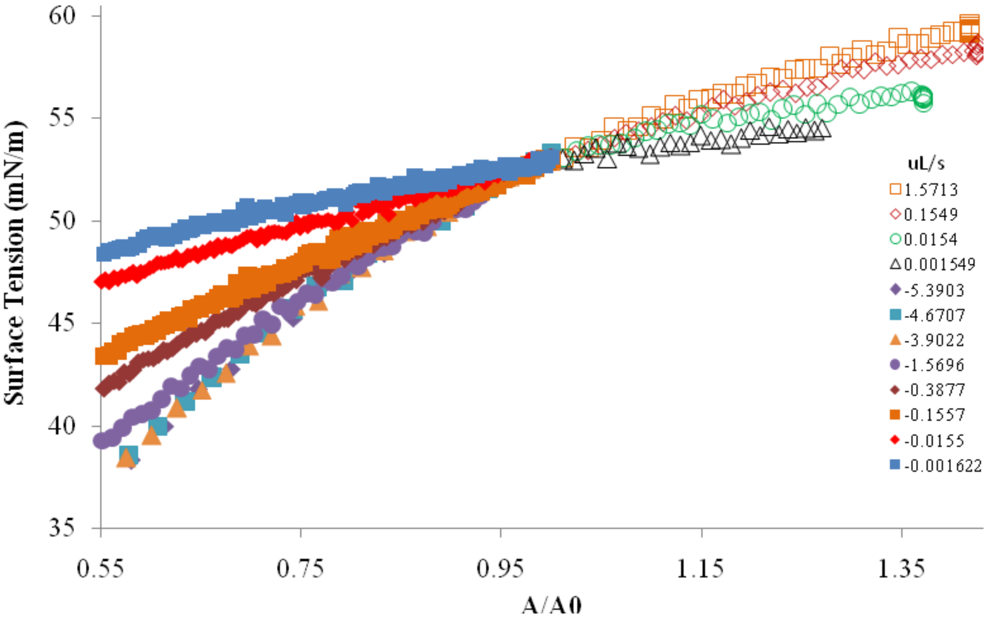

Figure 34: Series of compressions and expansions at varying rates. Solid markers represent compression tests, open markers are expansions. All tests begin at $A/A_0 = 1$, by definition. Equilibrium is approximately 52.5 mN/m for 6.25×10^{-3} mol/m^3 (6.25 μM) of $C_{12}E_8$ in water.

Experiments at the most rapid compressions and expansions probe the equation of state for this particular surfactant, as has previously been demonstrated [Nararajan & Wasan 1993]. Note that for the rapid compressions between -5.39 μL/s and -3.9 μL/s, there is dependence on compression speed, indicating that the surface is shrinking too fast for any surfactant to desorb over this range. In this way, the interface behaves as if the surfactant were insoluble, since the surfactant cannot leave the surface during the rapid time scale of compression. Slower speeds give more time for surfactant to desorb or adsorb, as the surface attempts to return to the equilibrium surface tension of 52.5 mN/m. Indeed, as the expansion / compression rates become slower, clear deviations from the fast-rate data are observed. The proposed model would fit this data directly, with a focus on convection from the interface, which has not yet been solved for in the literature. Deviations from the model would then be summarily investigated for the possibility of intermolecular interactions.

Linear fits over a range representing ten percent compression or expansion (i.e. $A=0.9\ A_0$ to $1.1A_0$) were used for normalization and comparison to oscillatory measurements. Figure 35 shows the resulting comparisons, using an average of the compression/expansion results and an average of several oscillatory runs.

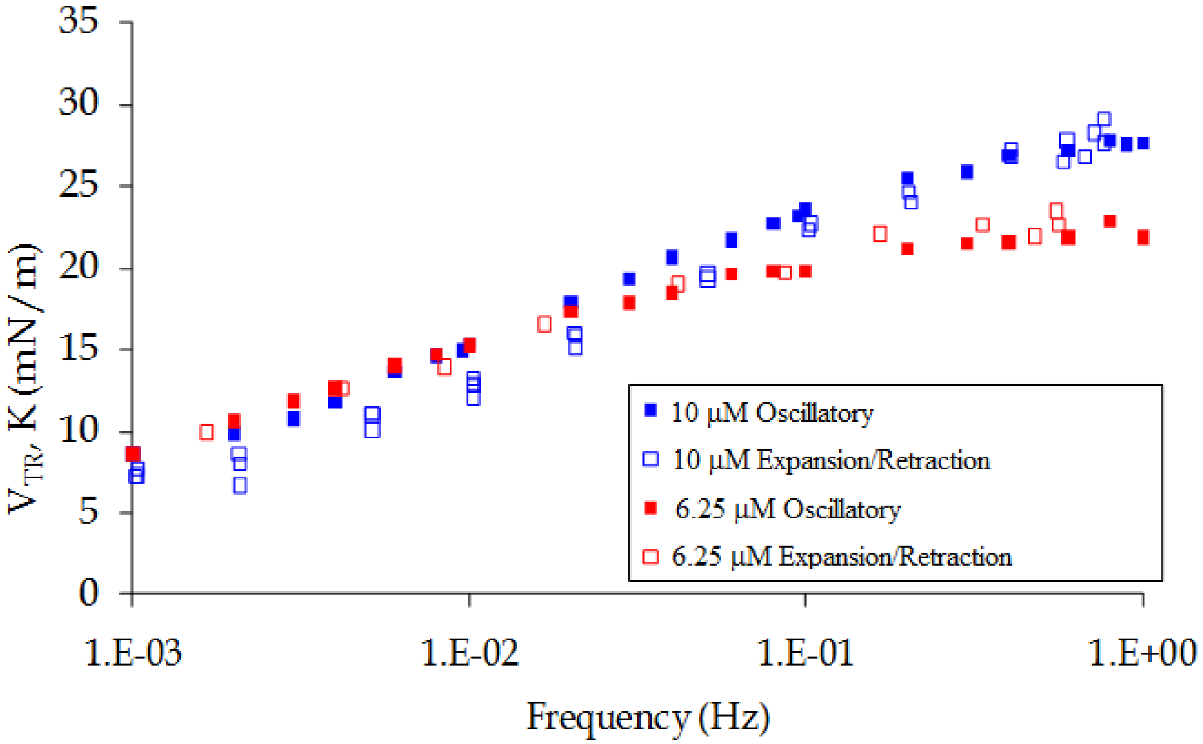

Figure 35: Direct comparison of Gibbs elasticity results from oscillatory tests, and normalized results from single-step compression/expansion tests.

The figure clearly demonstrates adherence between the two measurements, despite the lack of phase information in the single-step measurement. It is thus feasible to model the single-step test (provided the model describes the observed behavior) and from this, calculate the oscillatory response. However, it should be noted that a proper assessment would be to generate a frequency sweep from the single-step model using a Fourier transform (a rigorous explanation is available in Clint et al. (1981)). This is difficult to do with raw data, but possible if there is a high level of sampling. Due to scatter (the problem formulation requires derivatives from the data to be calculated, which is highly problematic even with the slightest bit of noise), this was not attempted with the current data, but this will be performed prior to publication using the model fits.

3.2.4. Conclusions

In this work, we performed a series of single-step deformations as well as an oscillatory frequency sweep to test the surface tension response of $C_{12}E_8$ at the air-liquid interface. We correlate the single-step test to the oscillatory test by correctly normalizing the single-step data, and thereby deduce that a proper model for the single-step test could thus be used to determine the oscillatory response of the surfactant. The model is currently in preparation, and publication will follow once it is complete.

3.3. Proteins

Proteins are complex charged molecules present in most forms of life. They are also known to be surface active and play a role in stabilizing foams from whipped cream to froth at the beach. We have studied three proteins in order to understand if there is a connection between surface rheology and foam stability for these materials.

Table 2. Proteins investigated

Protein	Molecular Weight
Bovine Serum Albumin (BSA)	66,382 g/mol
β-Casein	23,800 g/mol
β-Lactoglobulin	18,400 g/mol

We focused our efforts on bovine serum albumin (BSA) as a system which generates a robust interface with a pronounced interfacial shear rheology. We then investigated two other surface active proteins, beta-casein and beta-lactogloblin, in order to study the impact of interfacial rheology on foam stability. Protein solutions were tested with both shear and dilatational interfacial measurements. The only technique which did not lend itself to measurement of protein interfaces was the Micro Interfacial Rheometer because the surface moduli were above the measurement range as noted in section 0. In the following sections we will describe results from the ISR, du Noüy ring, and SDR.

3.3.1. Shear rheology of BSA Interfaces

Bovine serum albumin adsorbs to water-air interfaces forming a robust interfaces with interfacial shear properties which are easily measurable by both the Interfacial Stress Rheometer and the AR-G2 rheometer. This experimental system provides a good method to compare both instruments. Previous studies on the adsorption kinetics of BSA interfaces show that this protein adsorbs irreversibly onto air-water interfaces and will presumably form multilayered structures at the interface [Svitova et al. 2003]. BSA (Sigma Life Science) was mixed into a solution of 1 mM NaCl (Fisher Scientific) and stirred gently for several hours or overnight until the protein was completely dissolved. Solutions were prepared and stored in a refrigerator prior to use.

Prior to testing with the du Noüy ring fixture of the AR G2 rheometer, the ring was loaded and both rotational and oscillatory mapping was performed. The glass cup was cleaned with a solvent and then rinsed several times with fresh Milli-Q water. The ring was flamed with a propane torch prior to use. The protein solution was then loaded into the glass cup and the du Noüy ring was positioned at the interface. Typically, a time series was performed for 1-2 hours and then the oscillatory rheology of the interface was measured. Unless otherwise noted, results are for data where the measured raw phase was less than 90° so as to avoid any inertial artifacts.

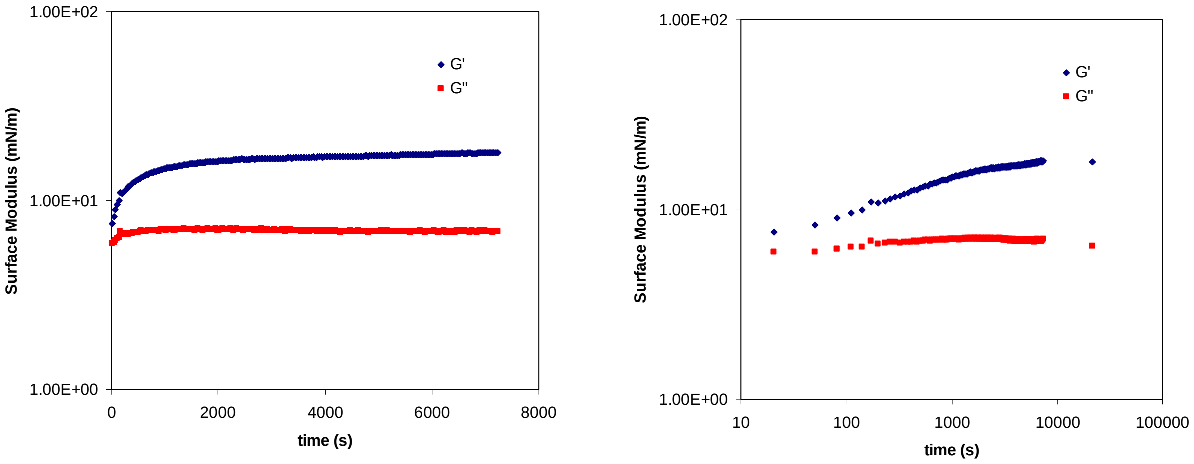

Figure 36: Interfacial modulus as a function of time for 0.1wt% BSA in 1mM NaCl tested at a frequency of 0.1Hz and strain of 0.6%. The extra points in the right graph are from subsequent tests on the aged interface at the same experimental conditions.

Figure 36 shows the interfacial moduli as a function of time for the a solution of 0.1wt% BSA in 1mM NaCl. Initially, both elastic and viscous moduli increase rapidly as a function of time, though the increase is more pronounced for the elastic modulus G'. After ~1000s, the viscous contribution reaches a plateau and even decreases slightly. Several additional data points at long times up to 21000 second (~6 hours) show that the elastic modulus is roughly equilibrated and the viscous modulus continues to decline slightly. This suggests that the interface is saturated with protein and stable.

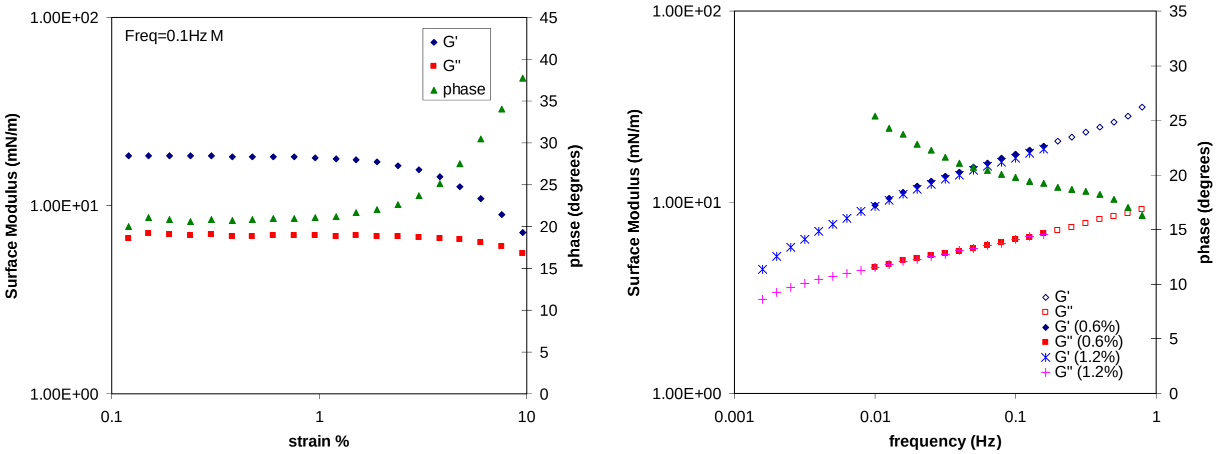

Figure 37: Oscillatory rheology of 0.1wt% BSA in 1mM NaCl (left) Strain sweep at f=0.1Hz and (right) frequency sweep at 0.6% strain. On right graph, crosses are data at a higher strain of 1.2% and open symbols are for data with raw phase angles above 90° indicating possible influence of inertial effects.

The oscillatory rheology of the interface is similar to bulk viscoelastic fluid rheology. The strain sweep shown in Figure 37shows a linear plateau for small strains where the moduli are independent of strain. At higher strains (>2%), the moduli decrease presumably due to the onset of non-linear effects. BSA surface films exhibit a modest dependence on frequency with both elastic and viscous contributions increasing with frequency and the phase angle decreasing. The results at low frequencies suggest that if lower frequencies were accessible, a cross-over point might be found.

We have also investigated the effect of salt and concentration on the interfacial rheology. Figure 38 shows a comparison of the interfacial rheology for 0.1wt% BSA in 1mM NaCl and the same solution diluted by half with fresh Milli-Q purified water to 0.05wt%BSA in 0.5mM NaCl. The more dilute solution has lower interfacial moduli, but at long times the elastic interfacial modulus is roughly identical. In the time-dependent plot, several data points from subsequent tests which matched the test frequency (0.1Hz) and strain (0.6%) of the initial aging study. As shown in the left plot, the moduli for the dilute solution are still increasing with time while the more concentrated solution has reached a long time plateau after 2 hours (3600s). Thus it is possible given the shapes of the time-dependent curves, that the dilute solution could reach the same values as the more concentrated BSA solution given a longer equilibration time. This is consistent with surface tension measurements on a more dilute 0.01wt% BSA solution where the time scales were even longer such that the surface tension were still decreasing after over 10 hours of observation [Svitova et al. 2003].

The similarity of the interfacial elastic moduli suggests that the main difference between the two concentrations is the time scale for adsorption of BSA at the interface. This lends credence to the hypothesis that the surface shear modulus is only dependent on the absorbed protein. At a lower concentration, it takes longer for the BSA to adsorb at the interface, but approaches the same interfacial conditions as the higher concentration.

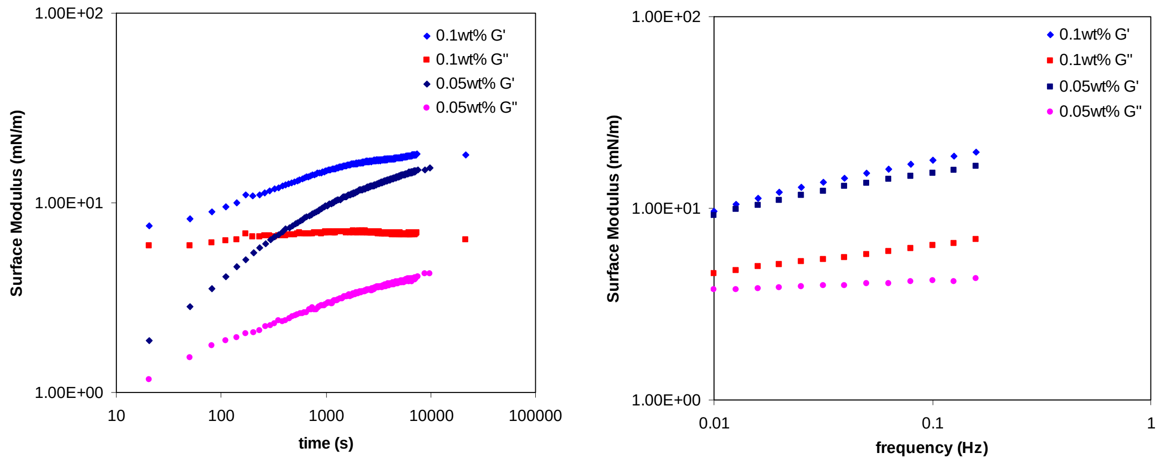

Figure 38: Comparison of interfacial rheology for 0.1wt%BSA and 0.05wt%BSA. Left surface moduli as a function of time measured at a frequency of 0.1Hz and a strain of 0.6%. Right, surface moduli as a function of frequency. While the 0.1wt% BSA solution was close to equilibrium, the moduli of the 0.05wt% BSA solution were still increasing. Isolated points on the time plot are taken from follow on tests which matched the same conditions.

In Figure 39 is the shear rheology measured with the ISR of two different BSA solutions plotted as a function of frequency at different times. Also plotted is the frequency response of just water. At each time point during the surface aging process, the frequency was varied from high to low, with 4 replicates at each frequency. The plots of surface shear modulus in the top of this figure indicate that above 10 Hz, the system response begins to become dominated by inertia effects. This is also apparent in the plots of the phase angle in the lower plots, with a rapid increase in the phase angle. Since this is an effect of the instrument, we will ignore them and focus on the surface effects that dominate below 5 Hz. Generally, the BSA interface is elastic and the modulus scales with frequency to 0.15 power. As the surface continues to age, the elasticity increases. To illustrate this trend, plotted in Figure 40 are responses at 0.1 and 1 Hz of the surface shear modulus and phase angle are plotted against time. The solution containing 0.02 wt.% BSA appears to exhibit a weaker dependence on time than the 0.1 wt.% BSA. At a given time, surprisingly the lower concentration has a higher surface shear modulus. We are not clear as to why this occurred, but it may be the result of testing a range of frequencies at each time point instead of a single frequency. This flow may have induced structural rearrangements in the layer.

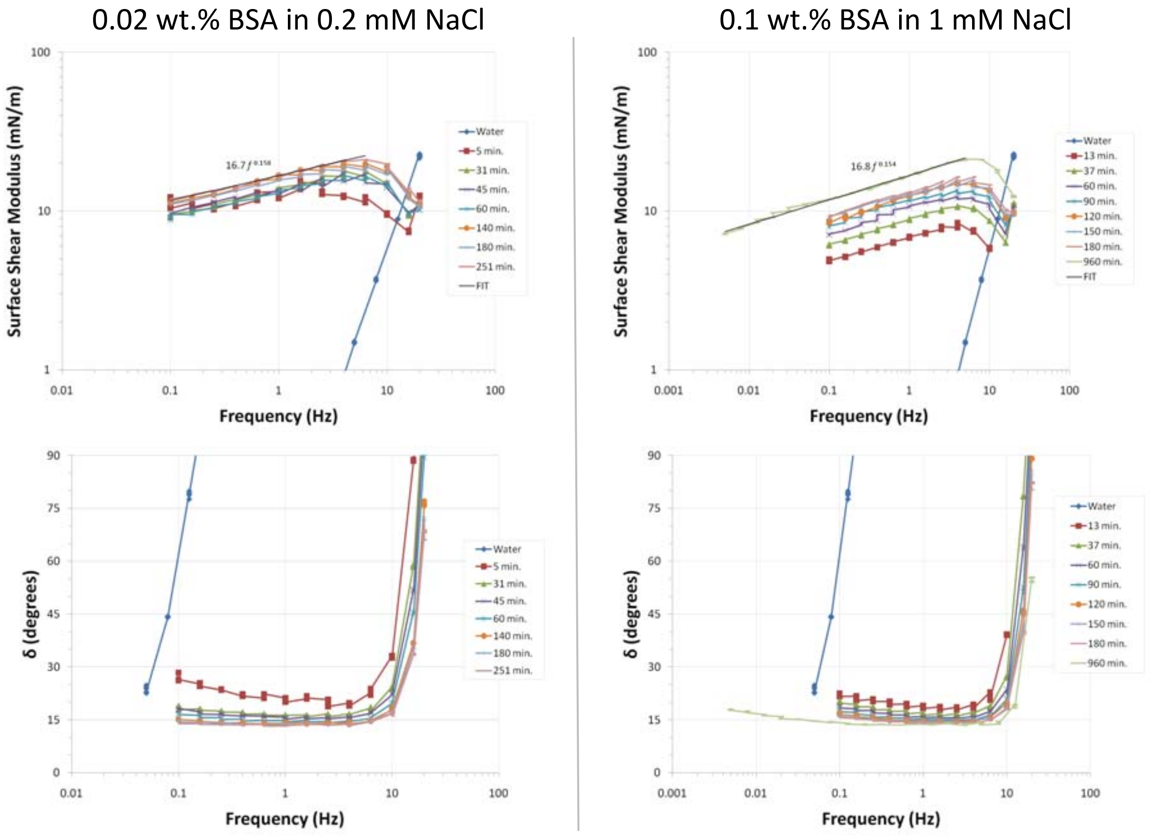

Figure 39: $|G_s^*|$ and phase angle vs. frequency measured with the ISR. Left: 0.02 wt.% BSA in 0.2 mM NaCl; Right: 0.1 wt% BSA in 1 mM NaCl.

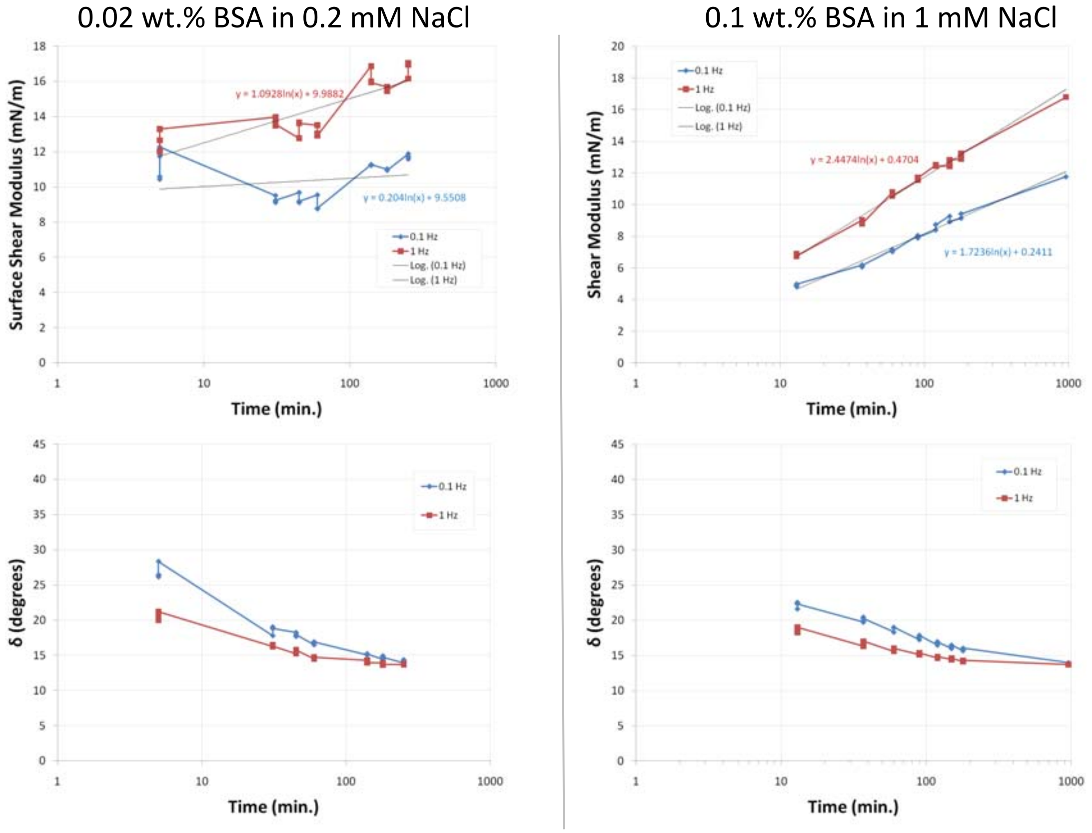

Figure 40: $|G_s^*|$ and phase angle vs. time measured with the ISR. Left: 0.02 wt.% BSA in 0.2 mM NaCl; Right: 0.1 wt% BSA in 1 mM NaCl.

In Figure 41, we compare the results from the oscillating du Noüy ring and the ISR for a solution of 0.1 wt.% BSA in 1 mM NaCl. We see that there is an appreciable discrepancy between the two measured values, with the du Noüy ring leveling off at around 19 mN/m and the ISR at 10 mN/m. This may be due to several factors. One possibility is the large gap between the ring and the rim of the cylindrical container (R_{cup}-R_{ring}=23mm). The wider the gap, the more likely the velocity/deformation profile at the interface will be curved as momentum transfer through the surface is dissipated into the bulk instead of transmitting to the walls. As a consequence, the measured strain which is averaged over the gap could be less than the actual strain that is local to the edge of the ring. The needle in the ISR is 3.5 mm away from the stationary glass cylinder, which ensures a linear deformation profile at the interface [Brooks 1999, Reynaert et al. 2008]. Another option is that the ISR does not account for inertial effects from the moving needle. Inertia would result in larger phase angles and higher moduli at large frequencies, but should not be an issue at small frequencies and strains. Another potential cause for the disagreements is due to the differences in the available BSA in solution due to the low surface-to-volume ratios and the nature of the container's surfaces. In the ISR, a Langmuir trough is used that is made out of Teflon. The liquid level is about 5-6 mm. After performing measurements with BSA solutions it was observed that the Teflon in the trough became hydrophilic because it was coated with BSA. Before each measurement the trough was cleaned. With the oscillating ring, the container was filled to a similar liquid level of ~5.8mm and was made of glass. The glass cup was cleaned before each use, but was not observed to develop a BSA coating after testing. Perhaps because the glass is naturally hydrophilic, the BSA did not adsorb as strongly. We suspect that in the ISR measurements BSA was being depleted as it coated the Teflon surface. As a result there was less material available to adsorb to the air-water interface, resulting a low bias in the ISR surface modulus values.

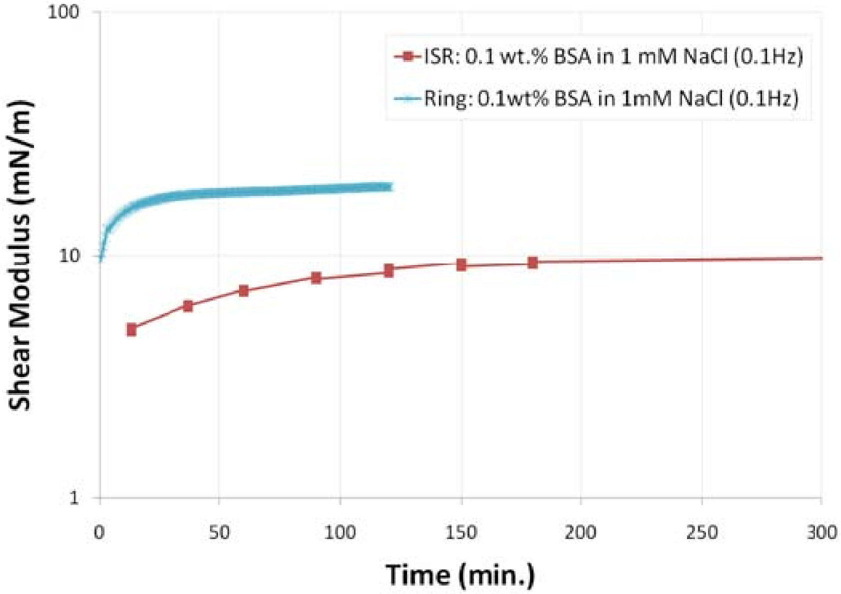

Figure 41: Comparison of interfacial shear moduli for Interfacial stress rheometer (ISR) and du Noüy ring with AR G2 rheometer at 0.1 Hz

3.3.2. Dilatational Rheology of BSA Interfaces

We also performed measurements of the dilatational rheology of BSA solutions. The dilatational response was tested for an air bubble in 0.02 wt.% BSA in 0.2 mM NaCl. The surface dilatational modulus and phase angle are plotted against frequency and surface tension in Figure 42. For each plot, the frequency was varied from 2 Hz to 0.1 Hz. At initial times (0-4 min.) the interface had a low dilatational modulus, around 10 mN/m. After 20 minutes, the dilatational modulus reached 60-70 mN/m. It also appears from the response, that the modulus at low frequencies may rise earlier than at high frequencies, as seen for Drop B, but this may be an artifact of performing the frequency sweeps from high to low and the time it took to reach 0.1 Hz. Also shown in Figure 42 is the dependence on surface tension, where we can see that as the surface tension drops during aging, the dilatational modulus increases and the interface becomes more elastic. For Drop B there was a significant change in the surface tension during the course of the measurement, which may explain why the value of the modulus at low frequencies for Drop B is much larger than at high frequencies.

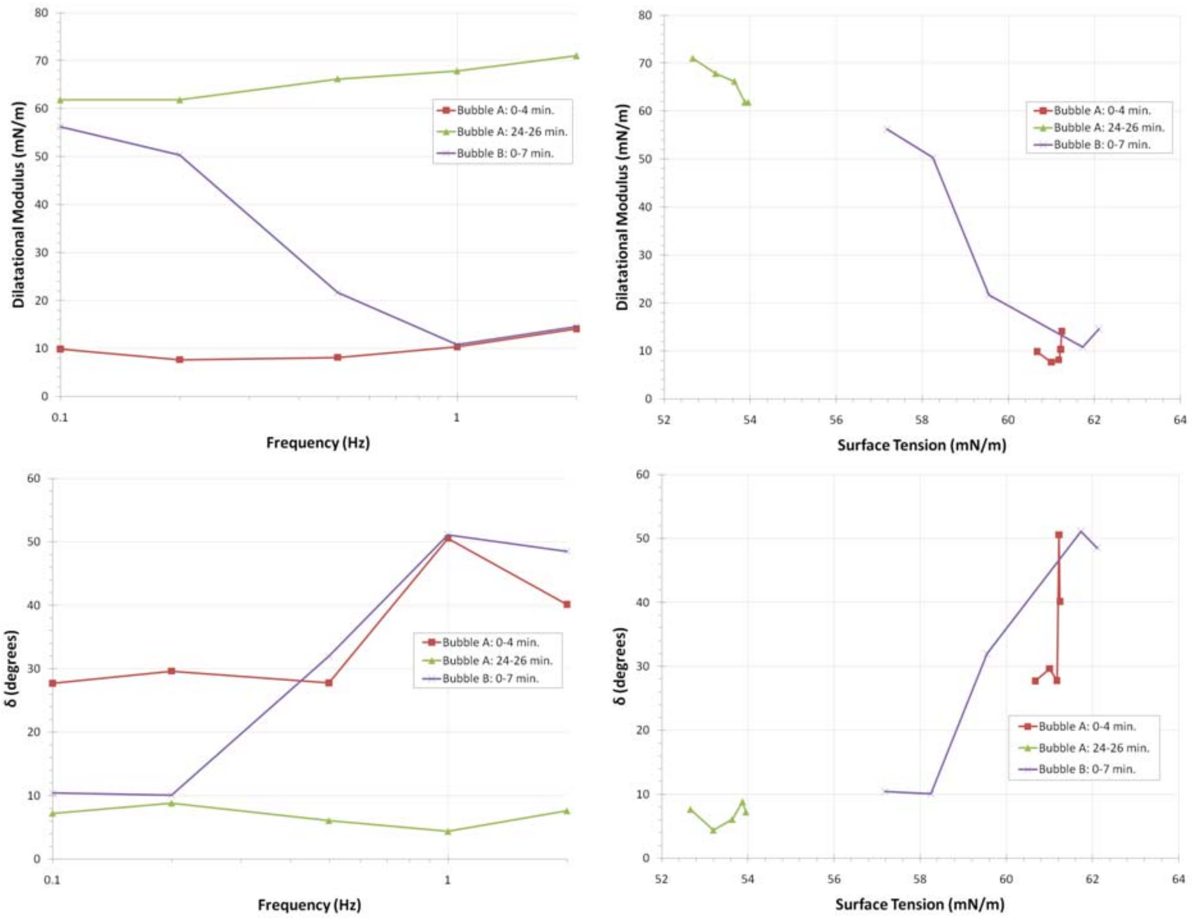

Figure 42: $|K_s^*|$ and phase angle vs. frequency and surface tension measured with the SDR. Air bubble inside a solution of 0.02 wt.% BSA in 0.2 mM NaCl.

We also performed measurements on liquid drops of 0.1 wt.% BSA in 1 mM NaCl at a fixed frequency of 0.5 Hz (Figure 43). Surface dilatational values obtained in this configuration are not as consistent as with the air bubble measurements, but are the same order of magnitude, ~10 mN/m, with phase angles approaching zero, as expected for an elastic interface. As mentioned earlier for the Pluronic® L31, the high surface to volume ratio of the drop configuration may result in a depletion of the surfactant form the bulk as it adsorbs to the interface. The increased reduction in the droplet case may be due to the higher concentration of BSA in the bulk. Unfortunately we do not have data on liquid drops at the 0.02 wt.% BSA concentration.

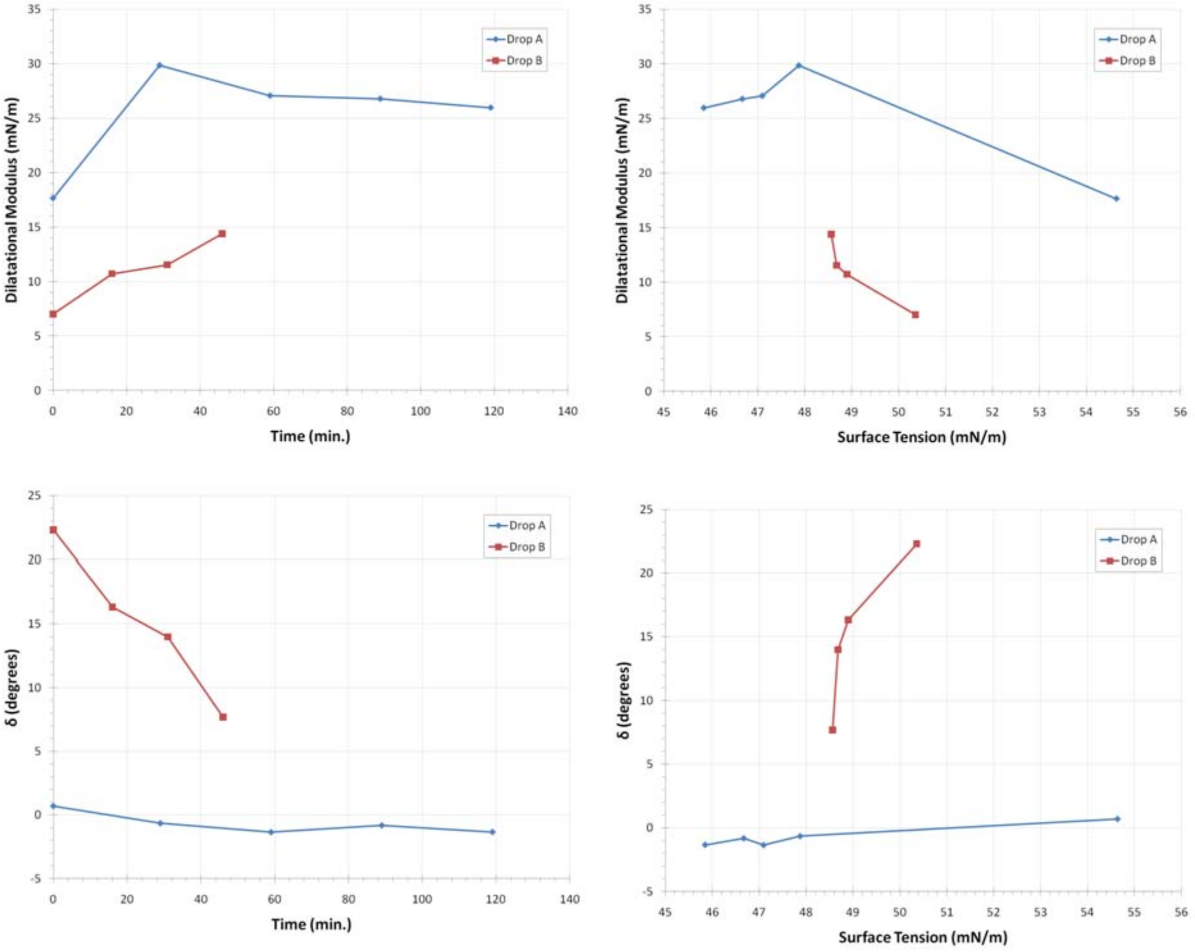

Figure 43: $|K_s^*|$ and phase angle vs. time and surface tension measured with the SDR at 0.5 Hz. Pendant drop of a solution of 0.1 wt.% BSA in 1 mM NaCl.

3.3.3. Du Noüy Ring Interfacial Rheology of Other Protein Interfaces

In order to investigate the influence of surface rheology on foam stability we have chosen to study a series of proteins with differing surface moduli, as well as introducing particles into our BSA solution. We have focused our efforts on β-lactoglobulin and β-casein as these two proteins have been previously studied with interfacial rheology [Bantchev & Schwartz 2003, Blijdenstein et al. 2010]. Time-dependent interfacial moduli are shown in Figure 44. We show a clear differentiation between the various proteins with β-lactoglobulin forming the stiffest film followed by BSA and β-casein having the weakest surface film. For all proteins, the elastic interfacial modulus is higher than the viscous component with the exception of β-casein where at short times, the viscous component is larger until 500 seconds. The measured phase angles for β-casein continue to be larger (33° at 2 hours) than those measured for BSA and β-lactoglobulin (both 15°). Because the surface film for β-casein is not as stiff, the signal is noisier. Also, inertial effects are more important. For the data shown in Figure 44, the raw phase angles are between 100° and 135°. This is higher than we prefer, but still well below the point where the measured signal is dominated by inertial interference (i.e. raw phase of 180°).

Our measurements agree very well with measurements on 0.1wt% β-casein and 0.1wt% β-lactoglobulin by Blijdenstein et al. (2010). Those measurements were performed with a bicone fixture (Anton Paar Physica MCR 300 rheometer). Our results for β-casein are less consistent with Bantchev & Schwartz (2003) using an interfacial stress rheometer, though their results are for much lower concentrations than we studied, so we cannot make a direct comparison. In their measurements, they also noted that for short times the viscous modulus was higher than the elastic modulus, but that the elastic component dominated at later times.

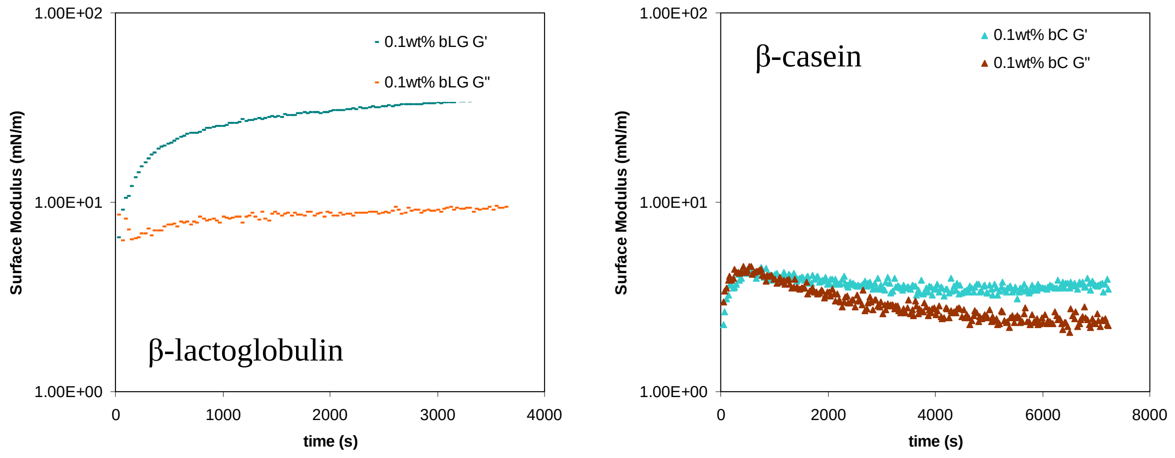

Figure 44: Time dependence of interfacial moduli for 0.1wt% β-lactoglobulin (left) and 0.1wt% β-Casein (right) at a frequency of 0.1Hz and a strain of 0.6%. Data for β-Casein had raw phase angles between 100-135°.

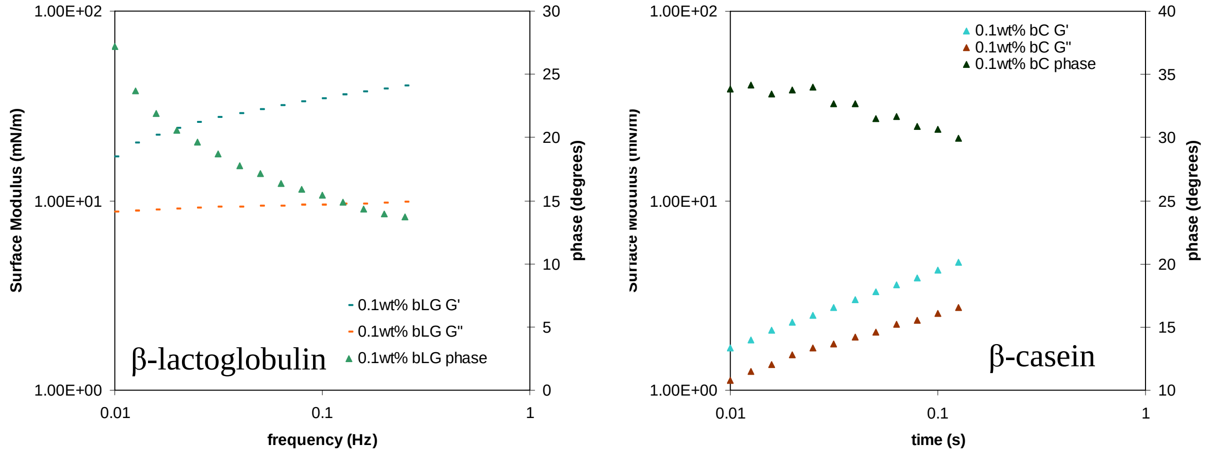

Figure 45: Frequency sweep for a strain of 0.6% for β-lactoglobulin (left) and β-casein (right). The raw phase angle for the 3 highest frequencies for β-casein are higher than 90° but below the inertial dominated regime (<145°).

Many of foams used for manufacturing applications at Sandia also contain small amounts of particle filler which have been observed to improve the quality of the foam. There is some debate over the mechanism for the improvement [Mondy et al. 2009]. Initial assumptions were that the filler acted at a nucleating agent, but microstructural studies of foam nucleation showed that these epoxy foams blow through heterogeneous nucleation caused by air bubbles entrained during foam precursor mixing. Here we have examined the effect of particle filler on the surface rheology of BSA solutions. Cabosil M5 fumed silica was added to a solution of 0.1 wt% BSA in 1 mM NaCl solution. The mixture was stirred overnight to dissolve the BSA and disperse the particles prior to being tested.

Results of the aging study as well as a frequency sweep are shown in Figure 46. The addition of 0.5 wt% Cabosil M5 particles has a clear and detrimental effect on the measured interfacial rheology, lowering both elastic and viscous moduli by at least a factor of 2. Additionally, the solution containing Cabosil particles did not approach equilibrium as quickly. This slowing down of the absorption dynamics is similar to that observed in the lower concentration BSA solution. Perhaps the addition of particle has bound some of the free BSA proteins in solution. But the substantial decrease in the magnitude of the moduli suggests that is not the only impact of the particles. It may be that the particles are also penetrating the adsorbed film of protein at the interface and somehow disrupting the formation of an elastic network or potentially changing the protein conformation at the interface.

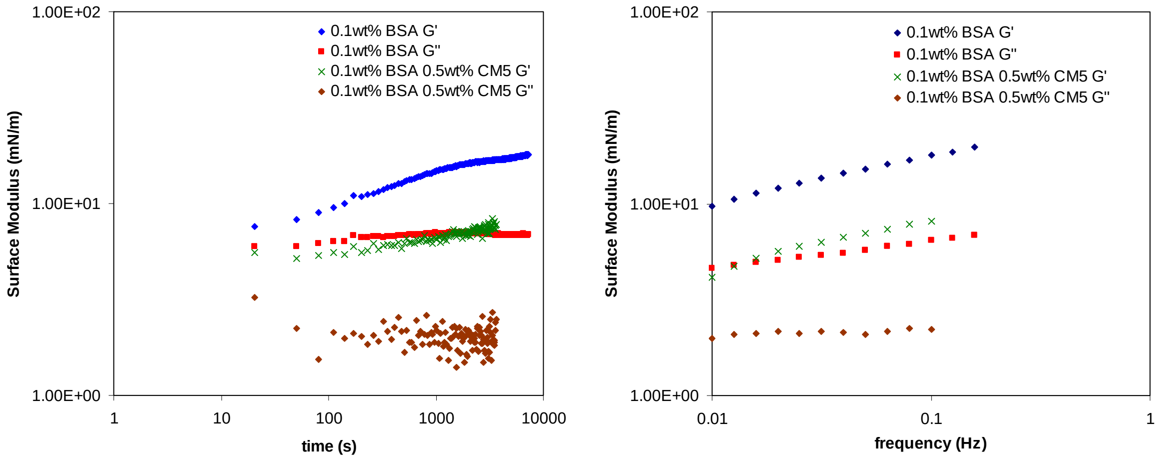

Figure 46: Effect of Cabosil M5 particle additive on surface rheology: left) time dependence at a frequency of 0.1Hz and a strain of 0.6%, right) frequency dependence (strain = 0.6%).

To summarize the overall stiffness of the interface of each of these protein films, it is useful to consider the complex modulus |G*|. In our final Figure 47, we summarize the relative interfacial rheology of all of the protein systems investigated. By varying the type of protein, concentration and particle additive, we have a series of protein solutions which span over an order of magnitude in the complex surface modulus for shearing deformations. We will now investigate dilatational modulus prior to studying the foamability and stability of these systems.

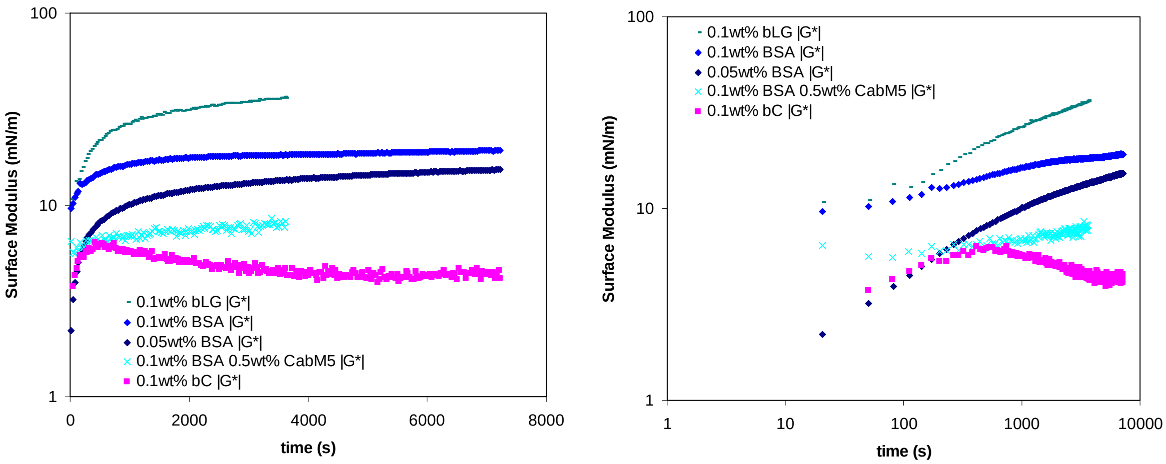

Figure 47: Comparison of the complex modulus |G*| for all protein solutions tested. Listed in order of largest complex modulus, the solutions are 0.1wt% β-lactoglobulin, 0.1wt% BSA, 0.05wt% BSA, 0.1wt% BSA with 0.5wt% Cabosil and 0.1wt% β-casein.

3.4. Effect of surfactant concentration on surface dilatational rheology measurements of oppositely charged polyelectrolyte-surfactant aggregates at the air-liquid interface

For the past several years, polyelectrolyte-surfactant (PES) systems have been an area of intense research due to their ability to modify both bulk and interfacial rheological properties. Recent publications have focused on mechanical properties of the air-liquid interface, as it applies to foam stability [Folmer & Kronberg 2000, Monteux et al. 2004, Kristin & von Klitzing 2010, Bergeron et al. 1996] and films [Cooke et al. 1998, Purcell et al. 1998, Purcell et al. 1995]. A study by Monteux, et al. utilizes ellipsometry, oscillatory pendant-drop tensiometry, a Ross-Miles type foam test, and interfacial shear rheology to characterize an oppositely charged system of polystyrene sulfonate and dodecyl trimethyl ammonium bromide [Monteux et al. 2004]. Results from the Monteux study indicate that at a 1:1 ratio of surfactant to polyelectrolyte monomer, there exists a clear peak in the Gibbs surface elasticity, as well as in foam stability. Here, we seek to similarly correlate the Gibbs elasticity from pendant-bubble measurements with foam stability for a system of polyvinylbenzoate and cetyl trimethyl ammonium bromide (pCTVB). This system was chosen as it has well known bulk-solution structural and rheological behavior [Kuntz & Walker(2007,2008)], is known to be surface active [Hodges et al 2009, Biggs et al. 2004], and most importantly, is nominally synthesized at the 1:1 surfactant-to-polyelectrolyte monomer ratio. We find that the pCTVB system experiences a peak in elasticity at the 1:1 ratio, which directly correlates to a decrease in foam stability over a range of ratios. Thus, our system behaves as a foam destabilizer and is characteristically different than that presented by Monteux in 2004.

3.4.1. Background

Polyelectrolytes are a useful class of polymers consisting of charged monomer units; they are readily synthesized in the lab, but many examples exist in nature (such as DNA and many proteins) that add to the need to fully understand their properties. When combined with surfactants, polyelectrolytes will exhibit widely varying behavior that can result in modified surface activity, alterations in structural conformation, drastically altered solution stability, and even starkly contrasting foam stability. If the polyelectrolyte-surfactant (PES) mixture is formed with charged surfactants, then the interactions become even more complex. Thus, there exists a desire to expand the current understanding of these materials and elucidate any trends.

Monteux, et al. demonstrated for a widely studied oppositely charged PES system, polystyrene sulfontate (PSS, anionic) and dodecyl trimethyl ammonium bromide (DTAB, cationic), that at a 1:1 ratio of monomer units to surfactant molecules, there is a peak in both the Gibbs surface elasticity and foam stability, as well as in relative film thickness. The serendipitous nature of the 1:1 ratio suggests that this may be the case for several oppositely charged PES systems, and could thus present a general rule for dealing with these systems. Thus, it is important to continue similar work on oppositely charged PES systems. Espinosa and Langevin subsequently produced a publication looking at DNA, polyacrylamide propane sulfonate, and carboxymethylcellulose, but did not find any relevance to the 1:1 point [Espinosa & Langevin 2009]. However, these measurements were completed only with a bicone interfacial rheometer, which measures interfacial shear stress, and not a dilatational tensiometer. The system we present here, the PES aggregate poly cetyltrimethyl-ammonium 4-vinylbenzoate (pCTVB), is a well-characterized system that has previously been shown to be surface active, and will provide more insight into the interfacial behavior of PES systems.

To determine the Gibbs elasticity, a pendant-bubble setup was utilized as in previous work by several authors [Espinosa & Langevin 2009, Tsay et al. 2004, Hsu et al. 2000]. The Gibbs elasticity is defined by the following equation,

$$K_s = \frac{\partial \sigma}{\partial \ln A} = A\frac{\partial \sigma}{\partial A} \tag{3.4.1}$$

Thus, a change in surface tension resulting from a change in surface area is a mechanical elasticity. For an oscillating surface area, one can directly measure the in-phase and out-of-phase components to the elasticity, whereas:

$$K_s^* = K_s^{'} + iK_s^{''} \tag{3.4.2}$$

$$K_s^{'} = \Delta\sigma \frac{A_0}{\Delta A}\cos\delta \tag{3.4.3}$$

$$K_s^{''} = \Delta\sigma \frac{A_0}{\Delta A}\sin\delta \tag{3.4.4}$$

In this setup, the pressure in the bubble oscillates according to a sine wave at some frequency ω, and the elastic (ε’, in-phase) and viscous (ε”, out-of-phase) components sum according to eqn. 3.4.2.

For foaming experiments, a simple Ross-Miles type test was used; surfactant solution is forcefully injected into a graduated cylinder containing the same solution and foam volume is measured after a set amount of time. While it gives only little quantitative information, qualitatively it is effective in determining relative stability as compared to other systems measured in the exact same device.

3.4.2. Materials and Methods

The creation of the pCTVB aggregates has been described previously [Kline 1999], with all materials coming from the same sources identified. Additional cetyl trimethyl ammonium bromide (CTAB) surfactant was purchased from Fluka, and was thrice recrystalized in ethanol and acetone to ensure purity. Water was passed through a Barnstead deionizer, yielding a resistivity of 18.2 MΩ-cm prior to use.

Initially, pCTVB samples were prepared at a 1:1 ratio and at 1 mg/mL. To achieve higher than 1:1 ratios, CTAB was added as necessary. A previous study demonstrated that this affects both surface tension and aggregate structure, and that introducing small amounts of bromide counter-ions has little effect on solution properties [Kuntz & Walker 2009]. Lower than 1:1 ratios were achieved by dialyzing the sample through a porous membrane (rated at 5,000 grams per mole, where the polymer is 300,000 grams per mole and the surfactant is 364 grams per mol, thus allowing only the surfactant to pass through) until the polymer crashes out of solution. After this limit, CTAB is added until the polymer resolubilizes. Actual ratios of surfactant are determined by working through a range of added surfactant from the bottom limit, and correlating the data to elasticities and foam volumes with a precisely known ratio after the 1:1 point. Each sample was prepared at a constant 0.1 mg/mL of polymer, with only the surfactant varying in concentration.

A pendant-bubble tensiometer setup was utilized to determine the Gibbs elasticity of pCTVB at varying ratios of surfactant and polyelectrolyte. A simplified schematic is pictured in Figure 22.The hook syringe was filled with air from the lab and immersed in solution within a glass holding cell. Backlighting was achieved with an LED spotlight and images were collected with a Basler 622fm firewire camera in conjunction with a zoom lens purchased from Edmund Optics. The general procedure is as follows: first, the camera frame capture was initiated. Then, a fresh bubble was produced in solution by forcing the linear actuator, and held for one thousand seconds. After, the linear actuator was oscillated at 1 Hz, causing the bubble to compress and expand. A 0.1 Hz test followed, and immediately following the test, the camera was stopped. Appropriate frame rates were used for each step so as to prevent over-sampling and bogging down image analysis. These images were post-processed with an edge detection technique, and drop profiles were fit to the Young-Laplace equation, as in previous papers [Tsay et al. 1997, Lin et al. 1995, Lin et al. 1996], to determine the bubble area and surface tension. Tension data for the first 1000 seconds was used to give information about the dynamics of the system; tension and area data for the oscillations were fit to sine waves and elasticities were calculated according to the equations presented in Monteux et al. (2004).

Foaming experiments were conducted with a Harvard Apparatus syringe pump positioned upright and above a 50 mL graduated cylinder. A 10 mL syringe was loaded fully with sample, and sprayed at 3 mL per second into the graduated cylinder, which also contained 10 mL of sample. The foam volume was recorded after 5 minutes.

3.4.3. Results

For simplification, the ratios presented are “X:1”, where X is the molar amount of surfactant relative to the molar amount of polymerized monomer, or C16TA+ to VB-. The dynamic tension results are presented first (Figure 48).

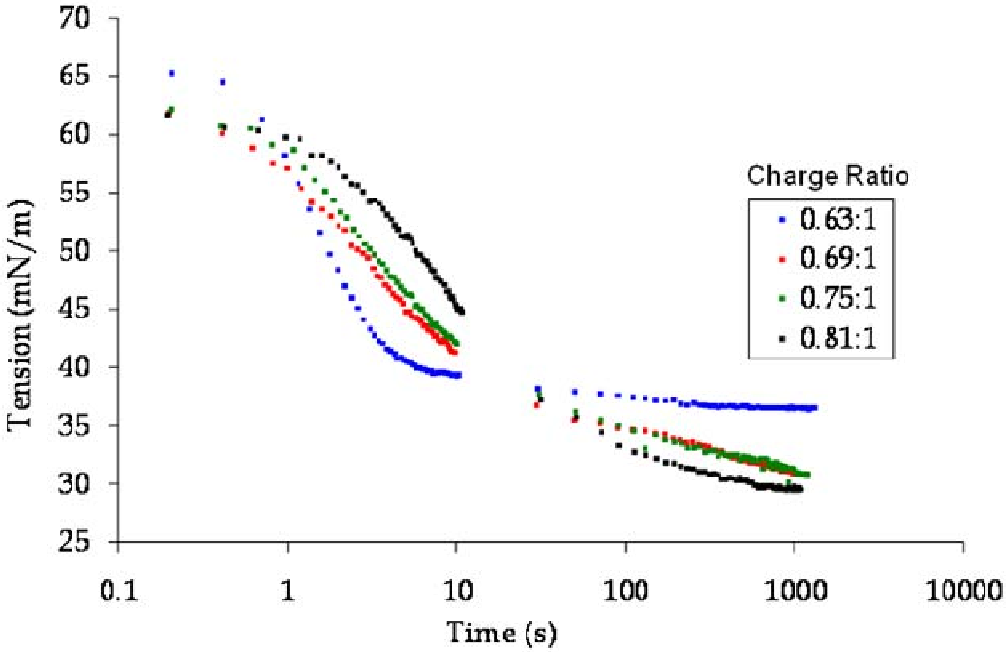

Figure 48: Dynamic surface tension of freshly created air bubbles in varying ratios of C16TA+ to polymerized VB- below the 1:1 point.

It should be noted that in no case, except for the lowest ratio, is equilibrium obviously achieved. We do not believe that this significantly affects the subsequent oscillatory experiments, given the reproducibility of the data, but it should be noted that there is not a current agreement in the literature as to what constitutes an equilibrium surface tension for PES systems, and in many cases the value chosen is essentially arbitrary. In our case, consistent aging times are relevant. Also, the gap in this and all dynamic tension plots in this report is due to a sudden switch in acquisition frame rate. For each case in Figure 49, the tension decreases significantly with time as more of the PES system diffuses to the interface. As the concentration of surfactant increases, the tension values at 1000 seconds decreases. Clean tension values of 72.5 mN/m are not achieved, likely due to pre-adsorbed material at the air-liquid interface before the bubble is completely enlarged. This is performed at relatively high PES concentrations, so clean values are not necessarily expected. Higher ratios of surfactant behaved somewhat differently (Figure 49).

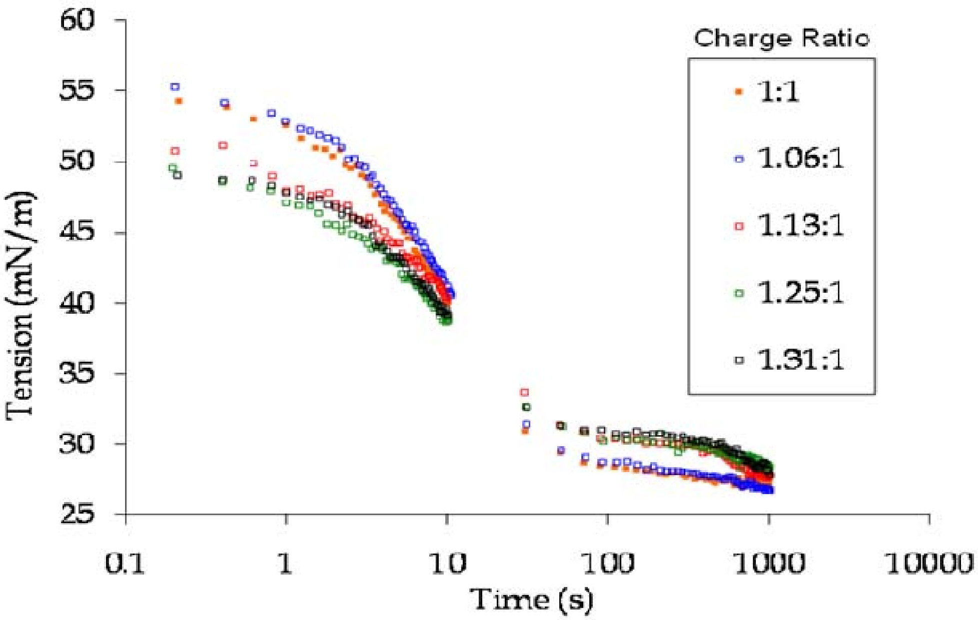

Figure 49: Dynamic surface tension of freshly created air bubbles in varying ratios of C16TA+ to polymerized VB- at and above the 1:1 point.

Once the 1:1 point is achieved, the tension at 1000 seconds hits its lowest value. After this, a clear and reproducible plateau is exhibited, starting at approximately 100 seconds for each test. This is not unlike the plateau shown for dilute ionic surfactant systems [Bonfillon et al. 1994], and it is possible that this is due to a presumed electrostatic barrier caused by free surfactant that is not associated with the aggregate. A previous study using a surfactant-specific electrode determined that above the 1:1 ratio, there are increasing amounts of free surfactant in the bulk, albeit existing at millimolar concentrations [Kuntz & Walker 2009]. The obvious way to test this is to add a significant amount of salt to screen charge interactions, which was performed for a ratio of 1.19:1 (Figure 50).

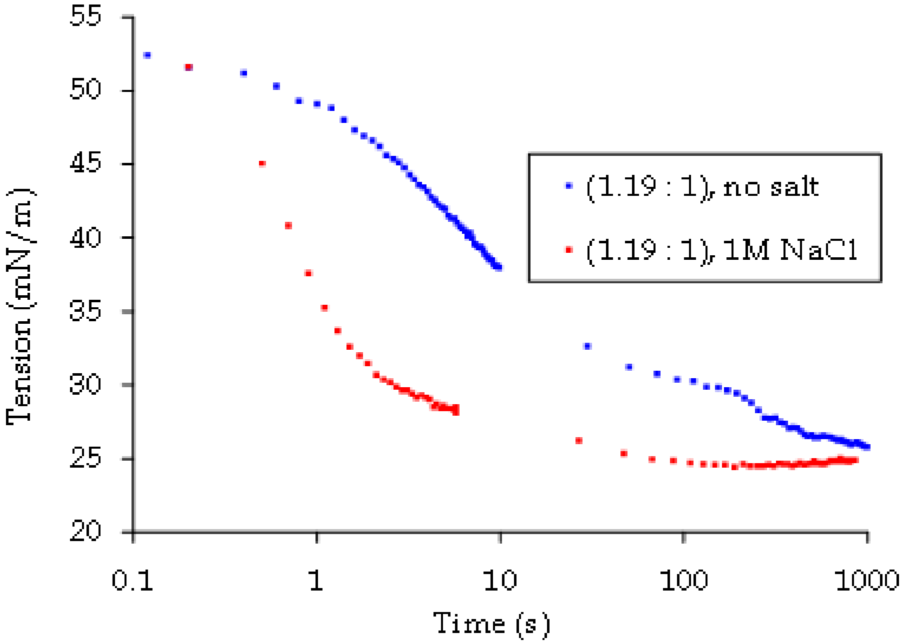

Figure 50: Comparison of dynamic surface tensions for a 1.19:1 ratio of C16TA+:VB- with no salt and 1 M NaCl.

Clearly, the added salts remove any possibility of an electrostatic barrier, and potentially prevent the plateau that might have been caused by free CTAB in solution. This in no way proves the hypothesis, but at least suggests behavior that could have implications for the foam stability and Gibbs elasticity. To effectively capture this behavior, the tension values at 100 and 1000 seconds were plotted as a function of the ratio (Figure 51).

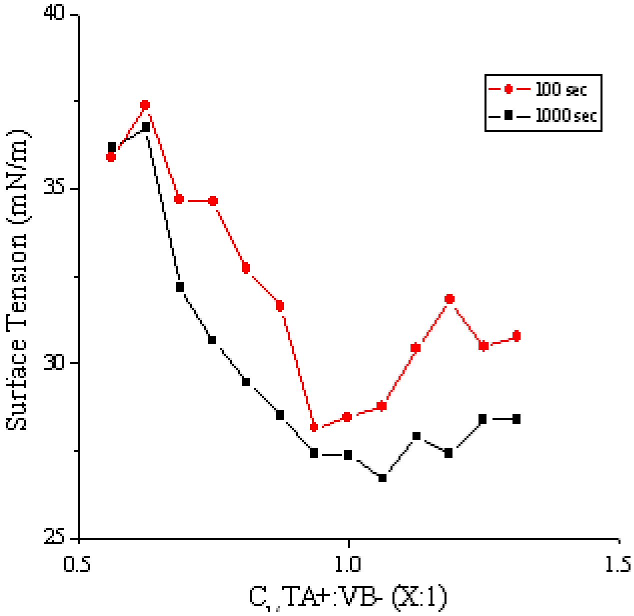

Figure 51: Surface tensions at 100 and 1000 seconds for each ratio of CTA+ to VB-.

Note that near the 1:1 ratio, there is a minimum in the surface tension values reported at 100 seconds, corresponding to the plateau in the dynamic data. While the cause of this plateau is not clear (though potentially electrostatic), Figure 52 shows how the existence of the plateau links to the measured Gibbs elasticities as measured at 1 Hz (0.1 Hz data showed qualitatively identical results).

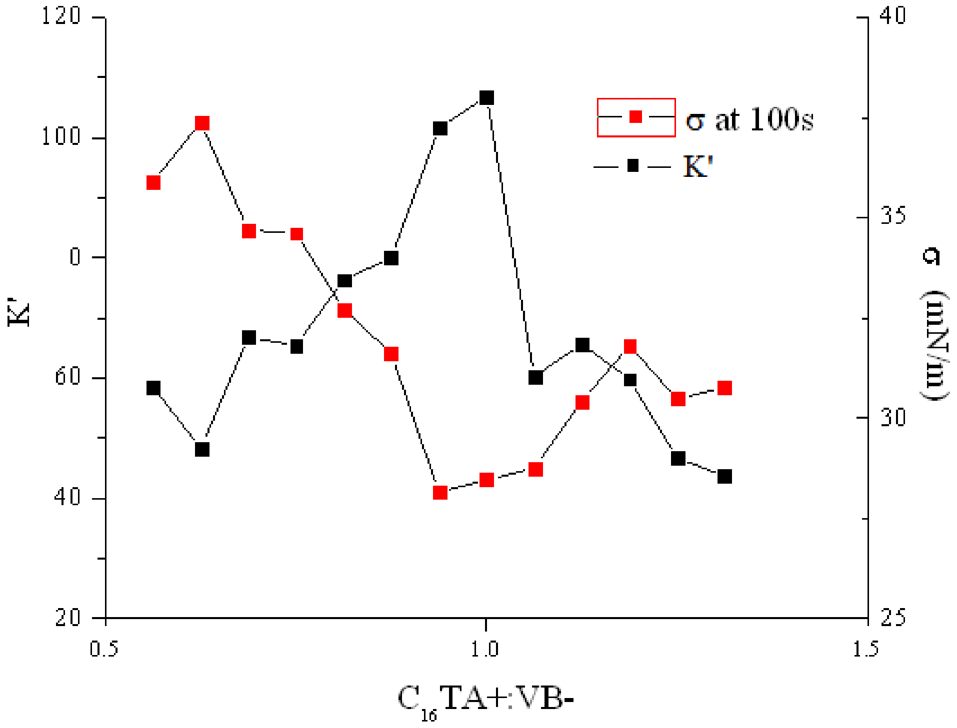

Figure 52: Comparison plot of the surface tension at 100 seconds and Gibbs elasticity for various ratios of CTA+ to VB-.

Strikingly, there is a clear correlation between surface tension at 100 seconds and the elasticity, both before and after the 1:1 point. Prior, of course, the tension moves downward while the elasticity increases as a function of added surfactant. Once the 1:1 point is reached, the tension increases as the elasticity decreases. Additionally, there is a clear peak in the elasticity at the 1:1 point, which agrees with Monteux's observation for the C12TAB/PSS system. The obvious question is thus- does the existence of a plateau in the dynamics have any impact on the elasticity, which is measured after the plateau ceases? A full study into the cause of the plateau would be necessary to answer this, and is not within the scope of this project. However, it is possible that the plateau indicates that material is prevented from adsorbing to the interface for some period of time, and that this further prevents restructuring in adsorbed PES aggregates that could yield a higher elasticity. A full study would include measurement of the elastic properties during and after the plateau, coupled with dynamic ellipsometry measurements and a study on salt effects. For now, however, it is clear that surfactant to monomer ratio, dynamics, and elasticity are linked and are consistent with Monteux's observation for a different system.

Foaming tests, though, do not agree with the previous work, and are presented in Figure 53 and Figure 54.

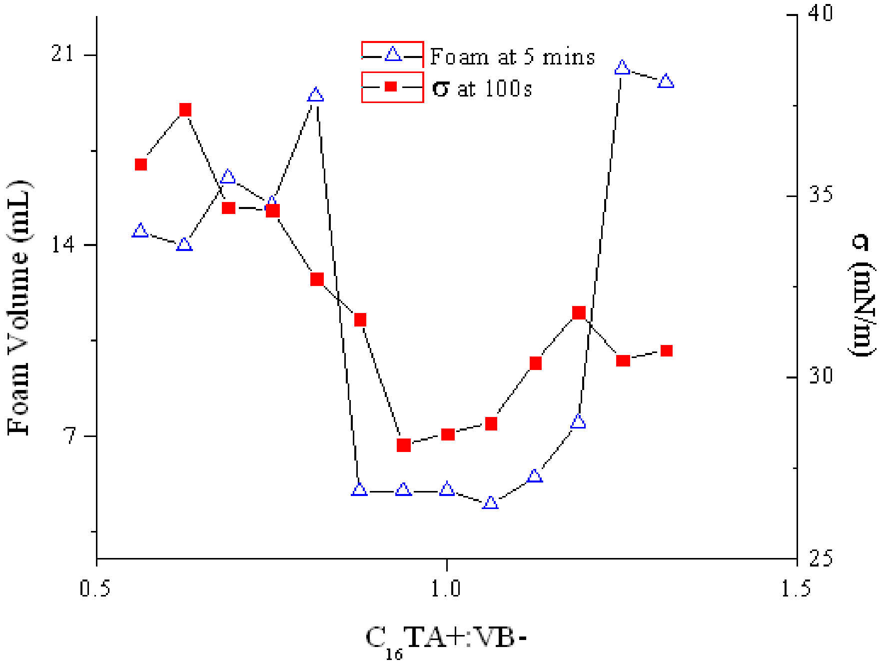

Figure 53: Foam volume at 5 minutes (Ross-Miles type test) and surface tension at 100 seconds (dynamic data).

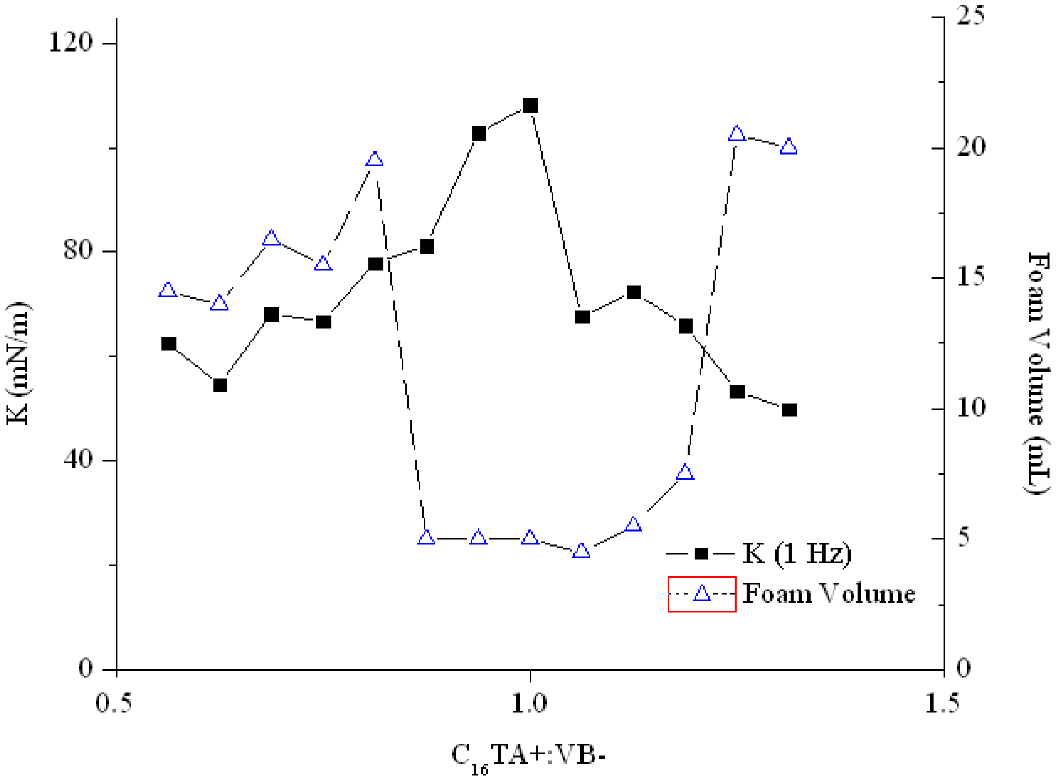

Figure 54: Foam volume at 5 minutes (Ross-Miles type test) and Gibbs elasticity at 1 Hz.

Interestingly, the foam volume reaches a minimum when the elasticity is the greatest. Equivalently, there is a direct correlation with the dynamic tension results and the foam volume.

Thus, while partially corroborating Monteux's results in that the elasticity peaks at the 1:1 point, we have found a system whose foaming response is in stark contrast to that of the C12TAB/PSS system. There are several differences between the studies that could lead to this result, most notably being the molecular weights of the polymers. This study uses a 330 kDa polymer, while the previous work uses a polymer around 43 kDa. Such a difference could lead to similar elasticity phenomenon, while the extremely long, rigid polymer might work against a stable foam. The surfactant alkyl chain length is slightly larger in our system, as well. Finally, PSS is known to create precipitates with certain amounts of surfactant, whereas pCTVB has yet to demonstrate such behavior (not for lack of testing).

3.4.4. Conclusions

The interfacial properties of the oppositely charged polyelectrolyte and surfactant system pCTVB were tested in a pendant-bubble tensiometer and in a Ross-Miles type foaming test. A previous study on a similar system indicates that at a 1:1 surfactant to monomer ratio, a peak exists in the Gibbs elasticity and foaming stability. The results presented here suggest that while a peak does exist in the Gibbs elasticity at the 1:1 ratio for pCTVB, this peak in fact translates to foam instability, and is thus in contrast to the previous system. Additionally, an interesting plateau exists in the dynamic surface tension for greater than 1:1 ratios, and more work must be performed to determine both the causes and effects such a plateau entails.

3.5. Soaps

We also had the opportunity to evaluate three body wash samples from a commercial vendor to see if we could observe any significant differences in the surface rheological behavior. All samples were tested for surface shear rheology on ISR, but unfortunately the solution with its low surface tension and good wetting characteristics completely wet the Teflon coated needle, causing it to not attach to the interface and sink to the bottom of the trough. Testing was also done on sample B using the du Noüy ring on the AR-G2 and the response was below the lower detection limits of the device.

We were able to get results for surface dilatational rheology using the SDR. Results for $|K_s^*|$ are plotted versus frequency for the three samples in Figure 55-Figure 57. We only report the magnitude of the surface dilatational modulus since the phase angles were difficult to determine accurately since the signal-to-noise ratio the surface tension response fits was low (0.4 to 4). Samples A and B were measured only in air bubble mode, whereas sample B was done with the air bubble and liquid drop mode. No dynamic surface tension response was observed with these samples, and surface rheology measurements were performed shortly after generating a bubble/drop. The results for samples A and C were similar: the surface dilatational modulus increased linearly from 3 to 7 mN/m over a frequency range of 0.25 to 1 Hz. An air bubble immersed in sample B gave more variable results from 2- 8 mN/m over the same frequency range, whereas the limited amount of data with a liquid drop showed a similar linear trend with frequency from 2 to 5 mN/m.

The values of $|K_s^*|$ at a frequency of 0.5 Hz are plotted against surface tension in Figure 58. Here again, samples A and C appear very similar with respect to surface tension (24.9-26.4 mN/m) and surface dilatational modulus (3.7-5.9 mN/m). Sample B yields values that are similar, but the surface dilatational modulus measured with the air bubble is more variable (1.9-7.7 mN/m).

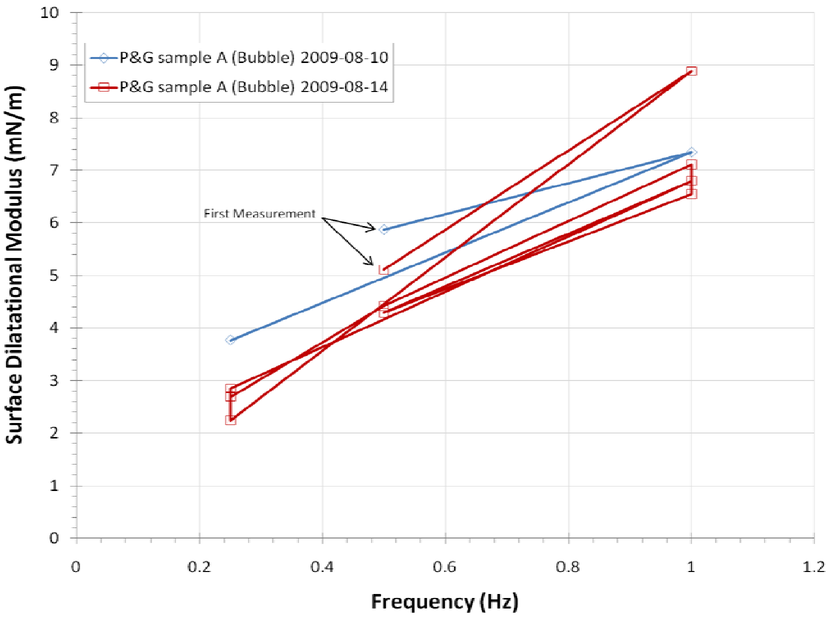

Figure 55: $|K_s^*|$ for Sample A

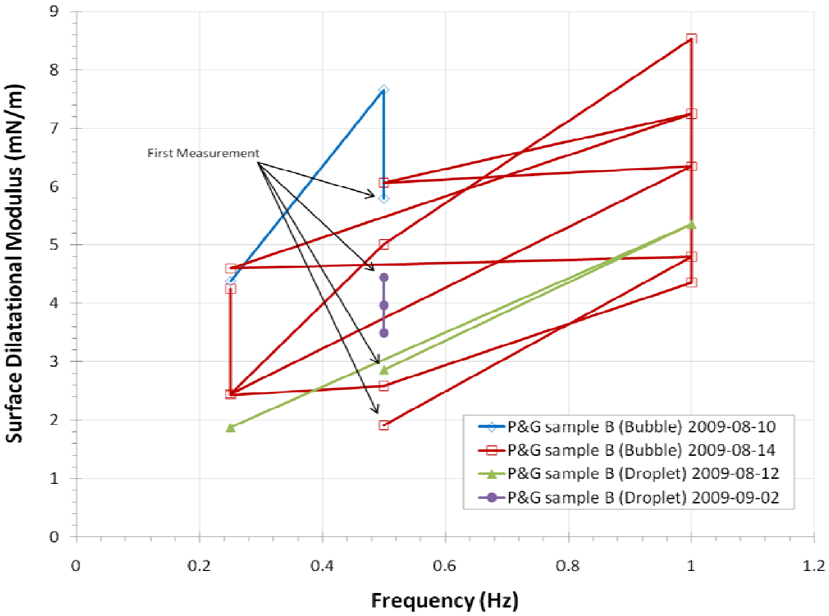

Figure 56: $|K_s^*|$ for Sample B

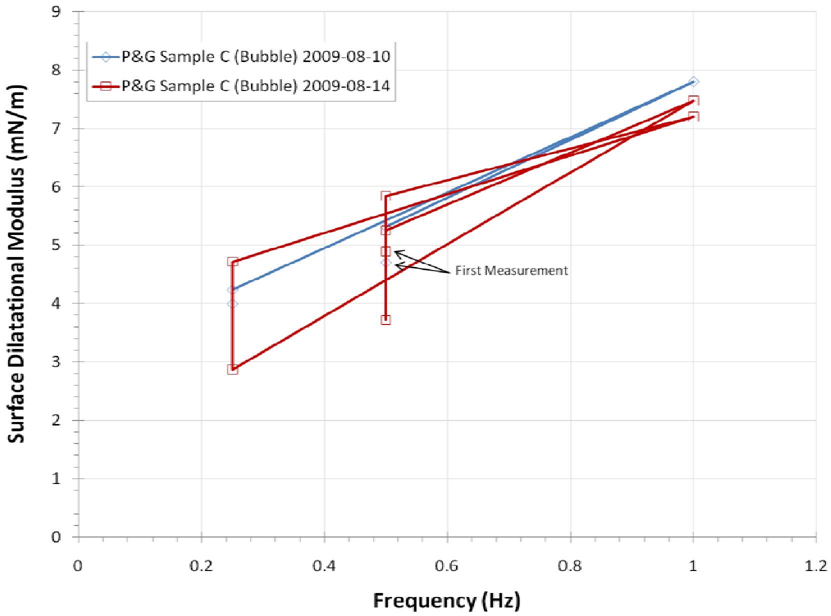

Figure 57: $|K_s^*|$ for Sample C

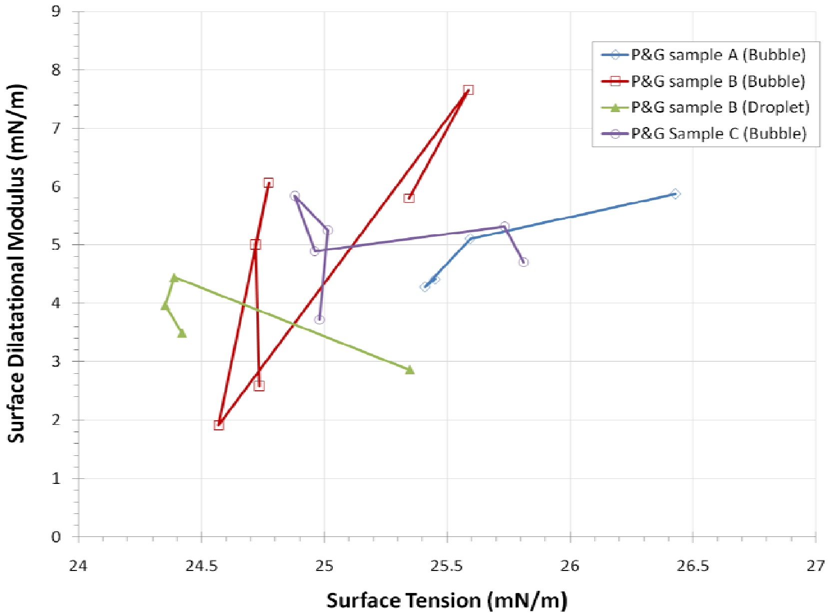

Figure 58: $|K_s^*|$ for Samples A, B, and C at a frequency of 0.5 Hz.

4. FOAMING STUDIES

Foams evolve by three basic processes: gravitational drainage of the continuous phase liquid, coalescence of bubbles because of rupture of the films separating them, and Ostwald ripening, which is the tendency of gas to diffuse from small bubbles to larger bubbles. Although all three processes are happening, each tends to dominate at a different time, with drainage occurring first, coalescence dominating later, and ripening happening on the diffusion time scale. Liquid drainage can be slowed by increasing the viscosity of the continuous phase liquid or the surface elasticity or viscosity [Pugh 1996, Monteux et al. 2004]. Slowing coalescence can be accomplished by making the liquid films in the foam more resistant to breakage, which many have argued can be accomplished with a high surface viscoelasticity [e.g. Tamura et al. 1995, Stubenrauch et al. 2009, Geogieva et al. 2009]. Finally, the rate of Ostwald ripening is also thought to be reduced with an increase in surface viscoelasticity [Wilson 1996, Blijdenstein et al. 2010], presumably by reducing the gas permeability across the film lamella. A few relevant studies are highlighted below.

Fruhner et al. (1999) used an oscillating bubble method to examine the surface dilatational properties of soluble surfactant solutions and foam stability. Although their results indicated that the dilatational viscosity played an important role in stabilizing foams, a direct relationship between elasticity values and foam stability was not detected. Monteux et al. (2004) looked at both shear surface rheology, using an ISR, and dilatational surface rheology, using an oscillating drop method, of oppositely charged polyelectrolyte/surfactant mixtures. Both the surface shear moduli exhibited a maximum at the molar ratio of polymer monomers and surfactant where foam volumes exhibited a maximum, indicating that the structure formed at the interface inhibits foam drainage and bubble coalescence. However, the peak dilatational moduli occurred at lower surfactant concentrations than the shear moduli, so did not appear to be as clearly related to the foam stability.[3]

In contrast, and more recently, Tan et al. (2009) ,Georgieva et al. (2009), Stubenrauch et al (2009) and Blijdenstein et al. (2010) all linked the dynamic surface dilatational moduli with foam stability. The work of Tan and colleagues on polypropylene glycol solutions suggests that increasing surface dilatational viscosity can be key to reducing liquid drainage rate. They estimated the surface dilatational viscosity from measurements of the dynamic surface tension at a dilating surface flowing over the top of an open cylinder. In this geometry the flow is of a pure dilatational nature without any shear effects coming into play [Prins 1999]. Stubenrauch and coworkers used systems of non-ionic surfactants and measured foamability and foam stability with two home-built instruments and with one commercially available one. They concluded that the difference in stability of foams generated with various concentrations of $C_{12}E_{6,}$ $C_{12}G_2$ and their 1:1 mixture was mainly due to differences in the rate of coalescence, and that, in turn, was controlled by surface viscoelasticity: the higher the value of the high frequency limit of the surface elasticity the more stable the foam. Georgieva et al. worked with the same non-ionic surfactants as well as two Pluronic® surfactants (F-68 and F-127). They concluded that the foams evolve with time first by Ostwald ripening controlled by the low frequency elasticity, and

---

[3] Freer et al. (2004) also compared shear and dilatational surface rheology, in their case of globular and flexible proteins at a hexadecane/water interface, and showed that the two can indicate structure at the interface, but that the response can be complex. They did not compare to foamability or foam stability.

then by bubble coalescence again found to be controlled by the high frequency limit. Both studies used oscillating drop techniques to measure the dilatational elasticity. Blijdenstein and coworkers' experimental design eliminated effects of coalescence and drainage to primarily observe Ostwald ripening. To measure surface dilatational viscosity, they used a Langmuir trough in which a layer spread at the air-liquid interface could be compressed with moving barriers and then relaxed. This resulted in a large deformation geometry that they argued was relevant to the process of disproportionation in a foam, although the frequency possible was much lower than with the oscillating drop method. They also measured surface shear rheology using a shear rheometer equipped with a biconical geometry placed right in the interface between air and liquid. Included in their study were the surface active proteins β-lactoglobulin and β-casein, and their behavior was contrasted with that of hydrophobin HFBII. Blijdenstein et al. found that K_s had the power to predict bubble stability against shrinkage and, hence, foam ripening. They also found the same trend with surface shear moduli, but argued that it was an indirect link that existed because all the surface parameters were interdependent and monotonic functions of surface adsorption of the proteins. All of the above studies report K_s to be much larger than G_s which is not surprising based on the fundamental relationship between the different surface moduli (see Appendix D). Many [e.g. Tamara et al. 1995, Tan et al. 2009] have argued that the Marangoni effect dominates the foam stability and is controlled by the surface dilatational viscosity (because that is the largest contributor).

In summary, although the studies of the relationship between foam stability and interface rheology are somewhat limited, and at times conflicting, the current thoughts on the importance of surface rheology in foam stability seem to be:

- Surface dilatational properties
  - Measured at high frequency influences coalescence rate,
  - Measured at low frequency influences Ostwald ripening,
  - May dominate the Marangoni effect and, hence, control drainage.
- Surface shear viscosity helps control drainage and is correlated with coalescence and ripening.

We wanted to perform a consistent study of foamability and foam stability of the materials described in Section 3 and correlate these with the surface properties also discussed in Section 3. Therefore, we could examine this correlation across families of surfactants.

4.1. Experimental

To generate the foam we forced house air through a metal air stone inserted in the solution. Ten stones with 0.5 μm pore diameter (NorthernBrewer.com), were tested in water prior to the study, and the one producing the most uniform distribution and size of bubbles was chosen. The pressure of the air was controlled to 8 psig in all tests and run until the foam reached a set height. Video recording of the experiment allowed the use of image processing and measurement of the foam and liquid height for any frame.

Figure 59 shows typical frames of video taken during foaming. The time was recorded when the gas was started and stopped and the video synchronized so that the time since foaming started and foaming was stopped was known for every frame. After the gas was stopped video recording at standard rate of 30 frames/s was continued until the foam disappeared or the change in liquid and foam height slowed significantly (Figure 60). At this time, if necessary, interval recording continued at a rate of approximately one frame every minute until the foam disappeared.

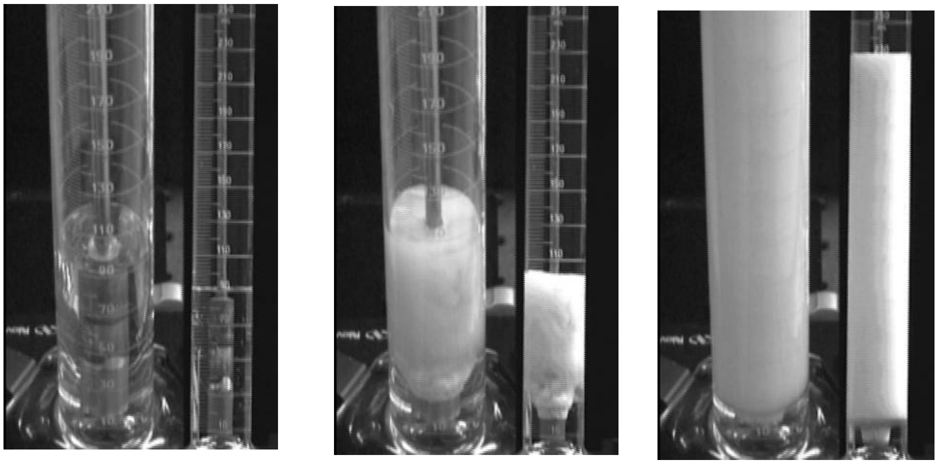

Time=0 1.2 s 6.6 s

Figure 59: Selected frames taken during foaming of L31

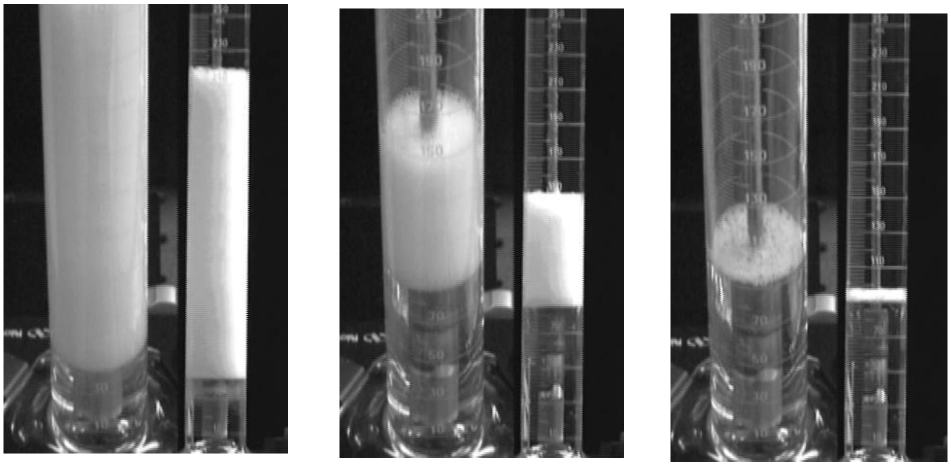

Time$_{\text{defoaming}}$ = 7.2 s 25.9 s 44.9 s

Figure 60: Selected frames taken as the L31 foam collapses

The initial liquid fraction of the foam was determined from the difference between the initial height of the liquid and that immediately upon cessation of air flow (giving the amount of liquid in the foam layer) and the height of the foam layer. All of the foams had an initial liquid fraction of about 0.30, and so can be considered "wet" foams in which liquid drainage will be significant at early times.

If the foam produced was initially stable against film rupture and foam collapse, the drainage of liquid could lead to much coarser bubbles at the top (Figure 61). Sometimes it was difficult to tell if the foam was just becoming very coarse or whether there was only a layer of bubbles clinging to the wall. The second view was helpful in this determination; nevertheless, the foam height should be considered less accurate for foams that clung to the walls, notably F108 and BSA.

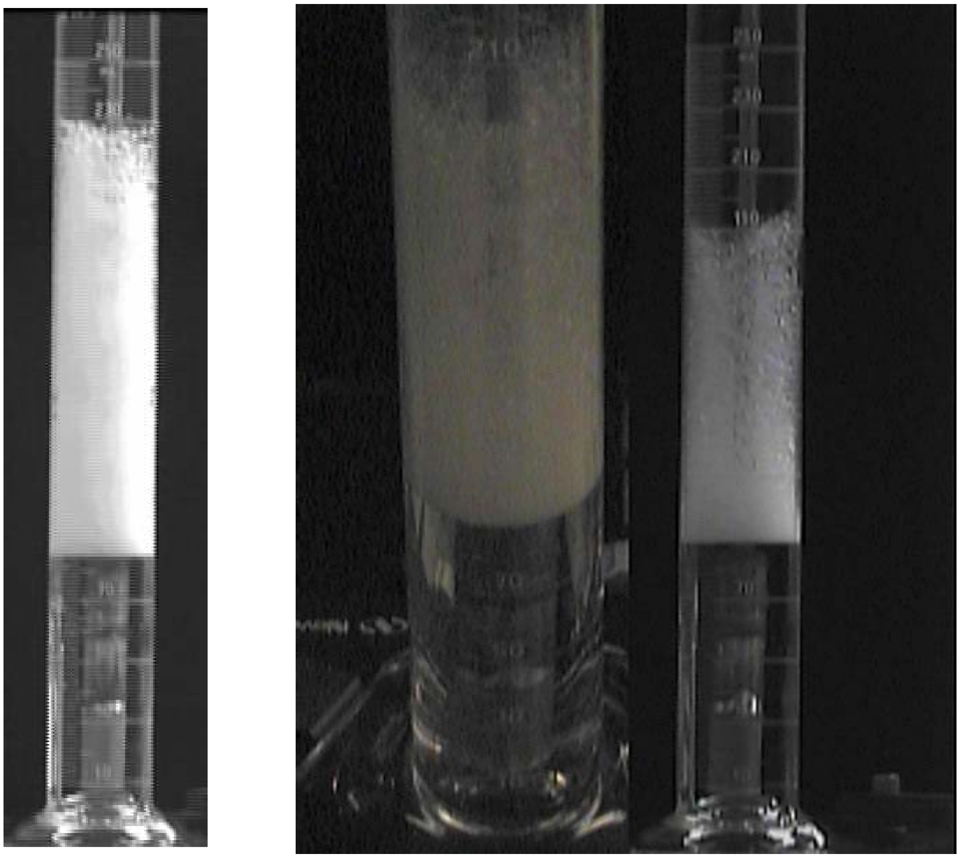

Figure 61: Coarsening at the top could lead to difficulty in measuring the foam height accurately for long-lived foams such as the F108 shown here.

4.2. Foaming and Defoaming Rates

4.2.1. Pluronic® Surfactants

As shown in Figure 62 and Figure 63, the L31 foamed quickly but was the least stable. Although the initial water content of the L31 was approximately that of the F108, and, to the eye, the bubble size looked about the same as those formed in the other Pluronic® foams, the L31 also collapsed much faster when the air was turned off (Figure 63). This pattern, in which solutions that collapse faster also foam faster, held for all the solutions tested, as will be seen in the following subsections, except one case (see next subsection, $C_{12}E_8$ at $2.5*10^{-3}$mol/m^3) where a foam that reached the top of our observation area could not be formed at all. This seems counterintuitive, because during foaming of an unstable foam, the bubble walls will be breaking while other bubbles are forming, and the competition between phenomena should lead to a slower foam growth but faster collapse when no air is being supplied. More careful observation of foam bubble size during foaming is suggested for future studies.

As another note, the shape of the foam volume with time during foam collapse was consistent with all non-ionic surfactants if plotted on the appropriate time scale. This shape can be seen in Figure 63 for P65, where one can see that the foam collapse is slow, then fast, then slow again.

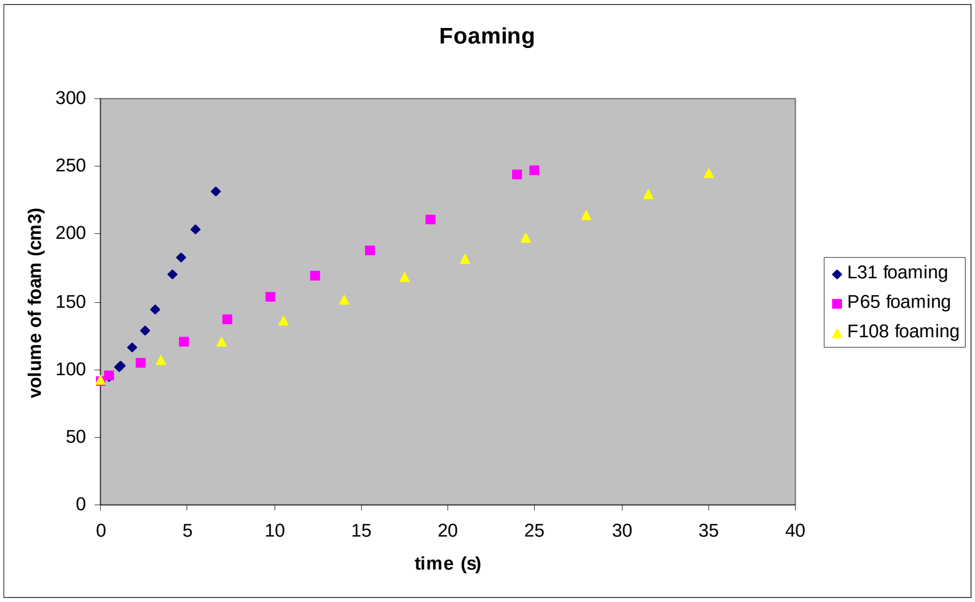

Figure 62: Foaming of three Pluronic® solutions, each at a concentration of 1 μM. Volume of foam" includes the unfoamed liquid at the bottom, and, hence does not start at zero but at the initial height of the liquid.

`

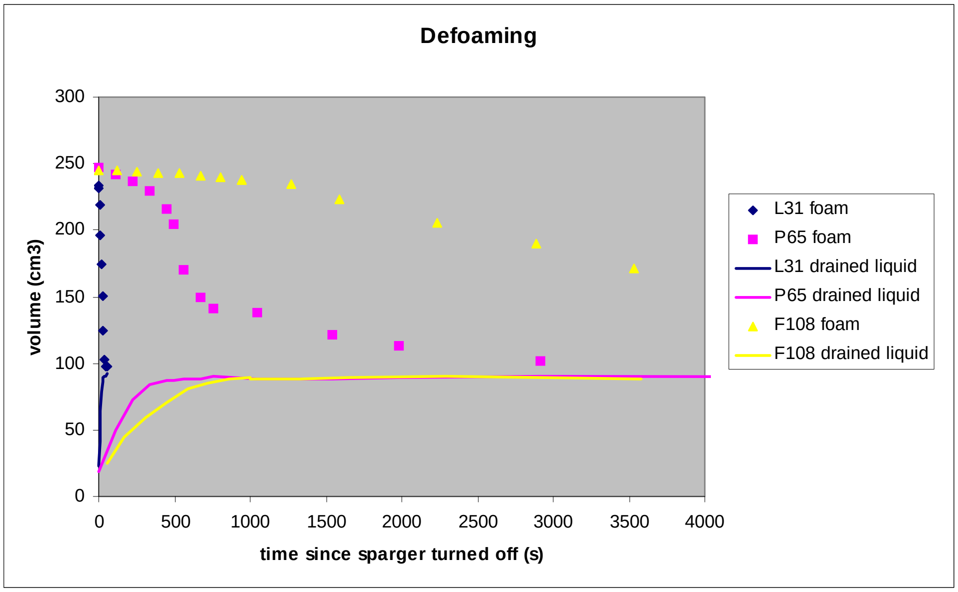

Figure 63: Liquid level and foam level as Pluronic® foams age

4.2.2. Octaethylene glycol monododecyl ether ($C_{12}E_8$)

The three concentrations of $C_{12}E_8$ were tested for foamability and foam stability: 1 x 10^{-2} mol/m^3, 6 x 10^{-3} mol/m^3, and 2.5 x 10^{-3} mol/m^3 (10, 6, and 2.5 µM). The solution with the lowest concentration never reached the height we had arbitrarily set as the maximum foam height to study (equivalent to about 250 mL in volume). Instead, after about 20 s the foam leveled off to a volume of about 175 mL, and when the air was at that point turned off, the foam collapsed within 3 seconds. This was the one example we saw where competition between foam bubble formation and foam collapse led to slower growth but fast collapse.

Figure 64 shows the rate of foam volume growth of the two higher concentrations of $C_{12}E_8$ and, for comparison, the rate of L31. Likewise, Figure 65 shows the rate of collapse once the air flow is stopped. Here the solution with the higher concentration of surfactant foams slightly slower yet takes roughly twice as long to collapse. The Pluronic® L31 also foams slightly slower than either concentration and collapses much slower. Clearly, even the “defoamer” L31 is more stable than these two concentrations of $C_{12}E_8$.

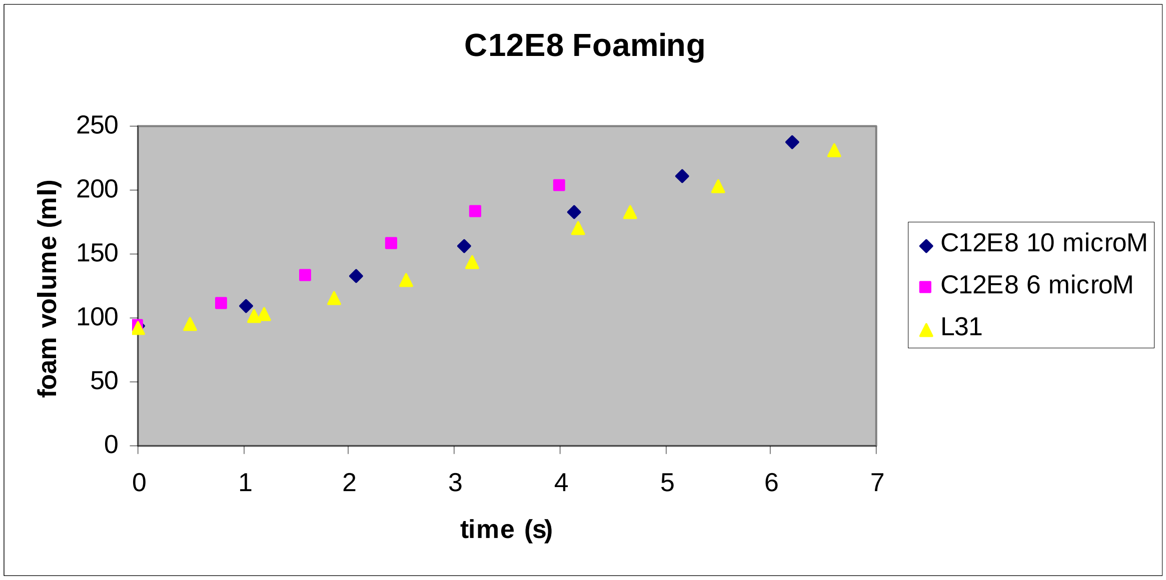

Figure 64: Foaming of $C_{12}E_8$ and compared to L31

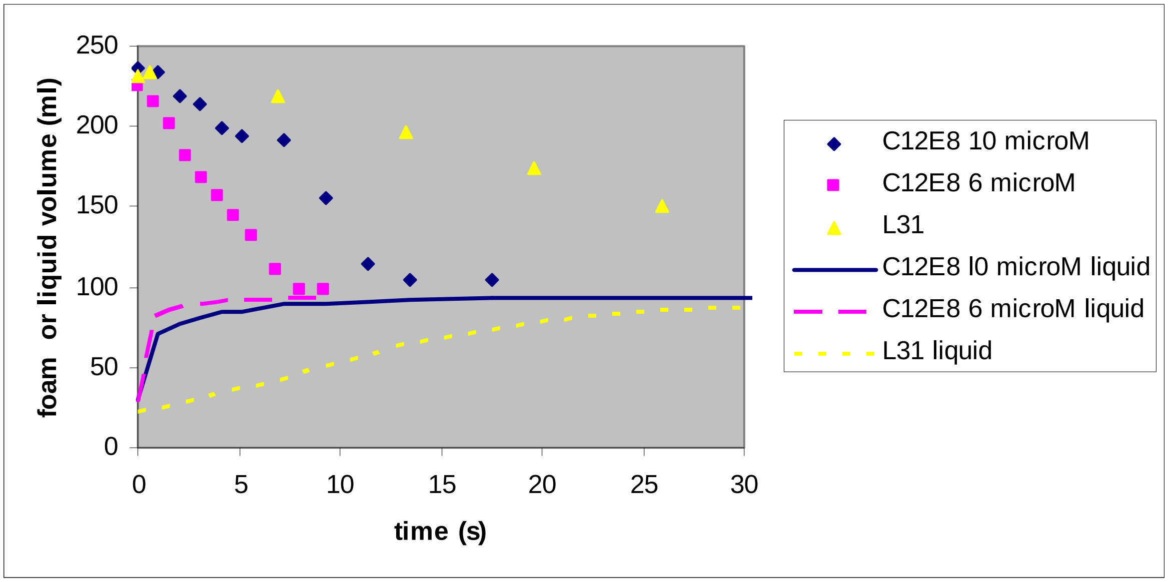

Figure 65: Foam and liquid volumes during foam collapse of $C_{12}E_8$ with data for L31 shown for comparison.

4.2.3. Proteins

Macromolecular surfactants were also used to create foams. The proteins BSA, β-lactoglobulin, and β-casein were compared, as were two concentrations of BSA. First, as shown in Figure 66 and Figure 67, the higher concentration of BSA (0.1 wt% BSA in 1 mM NaCl) may have been slightly more stable than the solution when diluted in half with Milli-Q water, as seen by the slightly slower initial collapse. The BSA foam stuck to the walls, making a determination of the foam volume very difficult. The higher concentration has slightly slower liquid drainage, which is a more accurate measurement than the foam volume. The two concentrations of BSA foamed almost identically. When compared to two Pluronic® surfactants, it is interesting to note that the BSA foams more like the L31, but drains and collapses slower (although not as slow as the P65).

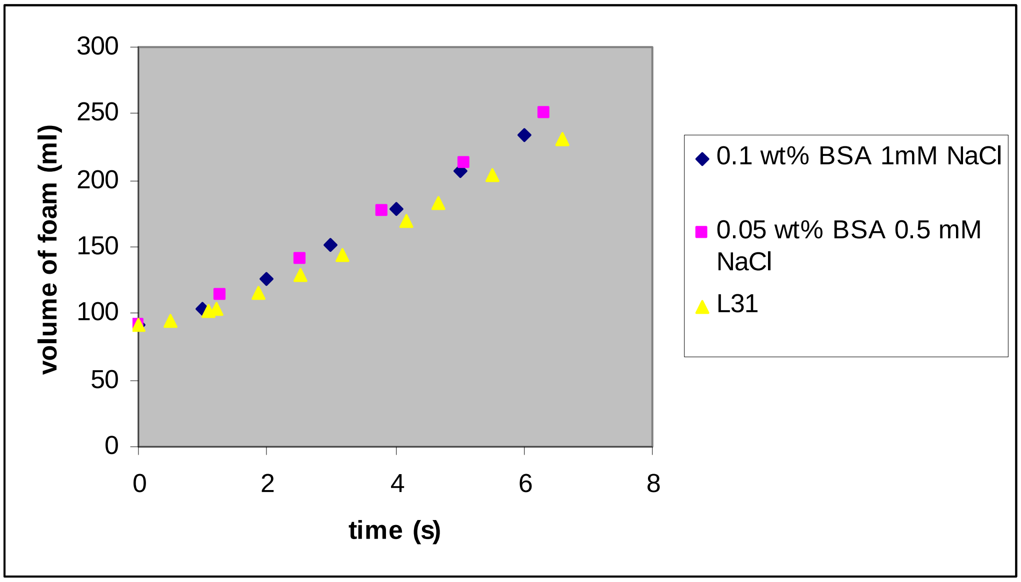

Figure 66: Foaming of BSA compared to L31

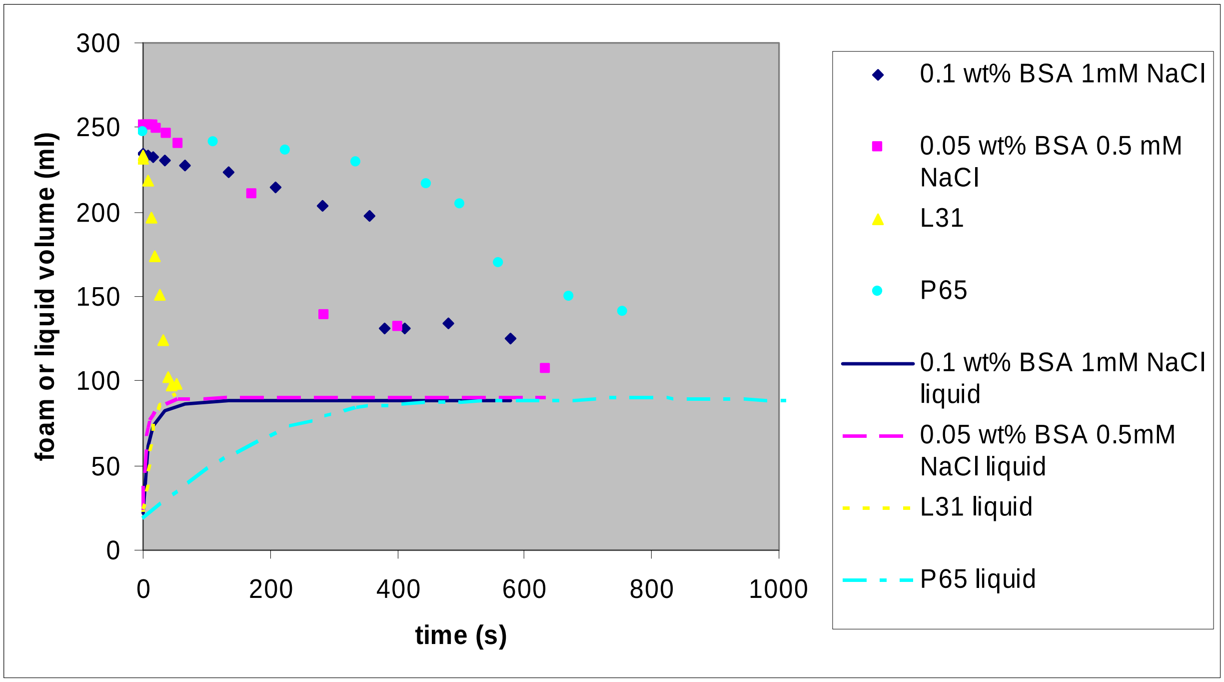

Figure 67: Foam and liquid height evolving in time during the foam collapse of two concentrations of BSA compared to two Pluronic® surfactants.

We also compared foaming across the families of Proteins. As can be seen in Figure 68, all three protein solutions, BSA in 1mM NaCl, β-lactoglobulin in water, and β-casein in water, all at a protein concentration of 0.1wt%, had similar foaming behavior. The sparger was accidentally stopped too early for the β-lactoglobulin foam, which may have caused the last point to be slightly below the others. Within experimental error there is no difference in the rate of foaming of these solutions.

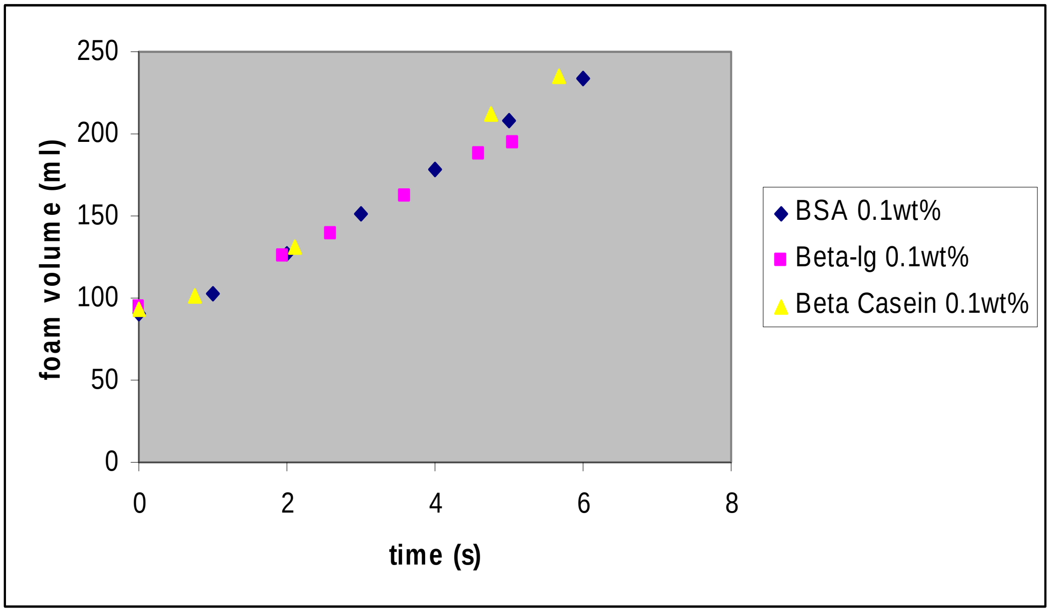

Figure 68: Rate of foaming of three protein solutions.

On the other hand, the β-casein clearly makes a more stable foam (Figure 69). Here, because the final volume of the β-lactoglobulin foam was significantly less, we normalized by the final volumes of each of the foams. The BSA, as mentioned earlier, made a foam that stuck to the walls, making the foam volume difficult to determine after the first 70 seconds after the air was stopped. F108 is also plotted, and though it also stuck to the walls making the foam volume approximate at later times, one can see that the ß-casein is about as stable as the “good foamer” F108.

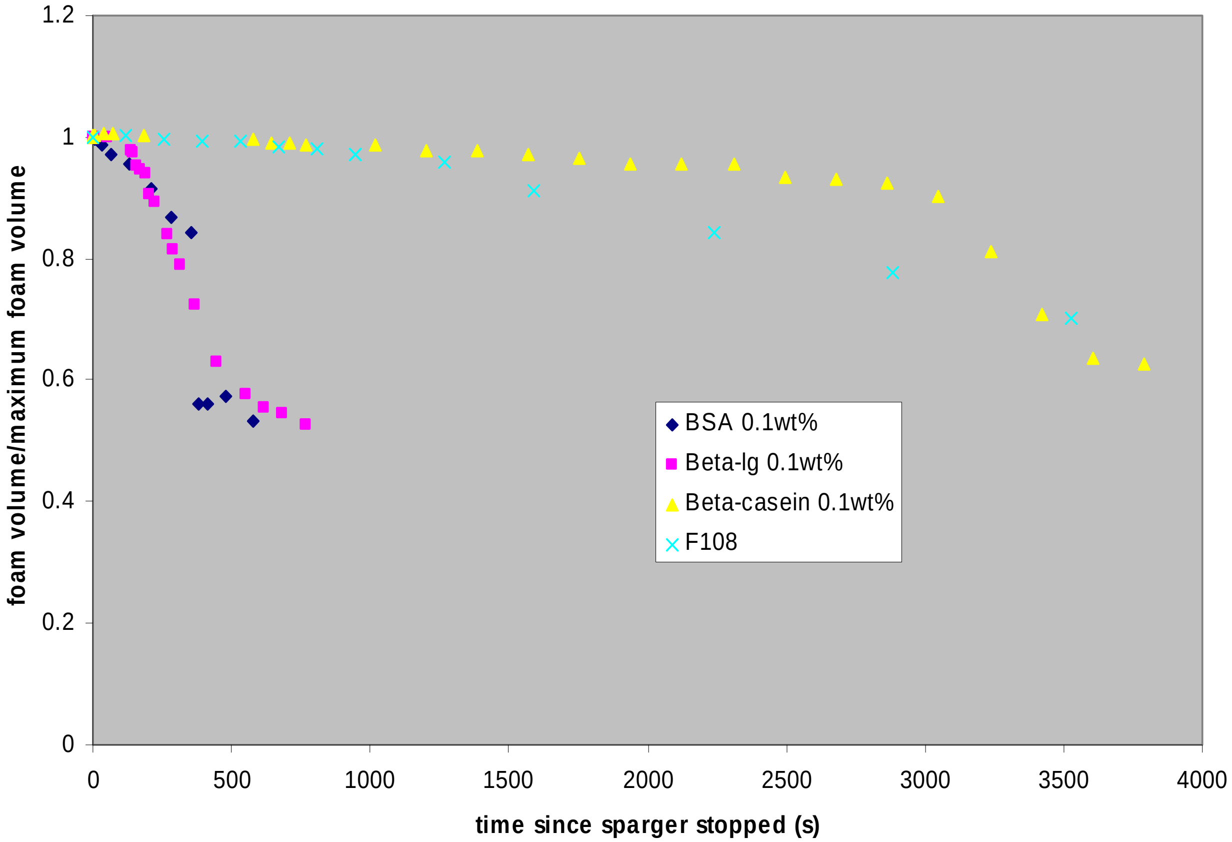

Figure 69: The rate of foam collapse of three protein solutions, with Pluronic® F108 plotted for comparison.

4.2.4. Particle-Surfactant System

Next we looked at the effect on foamability and foam stability when 0.5 wt% of Cabosil MS was added to 0.1wt% BSA in 1 mM NaCl. Again the foaming rate was indistinguishable (Figure 70). The particles did stabilize the foam however, leading to a collapsing rate of about half of the solution without particles (Figure 71). However, the particle solution was not as stable as the β-casein (compare to Figure 69). Interestingly the liquid drainage rate was faster with the addition of Cabosil M5 (Figure 72).

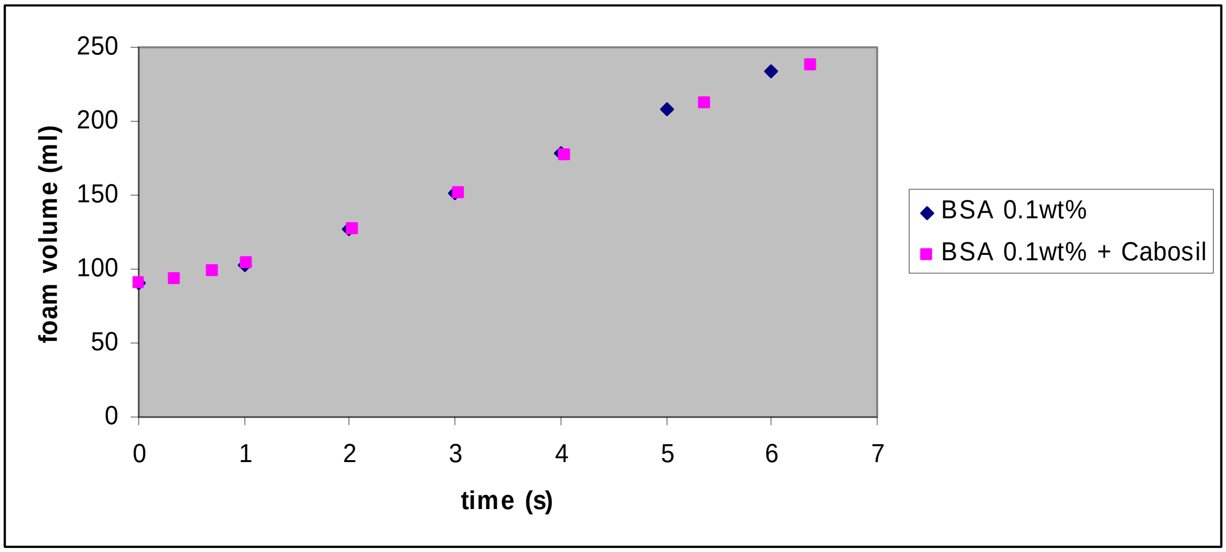

Figure 70: Foaming rate of BSA solution with and without added Cabosil M5.

Figure 71: Rate of foam collapse of BSA solution with and without added Cabosil M5.

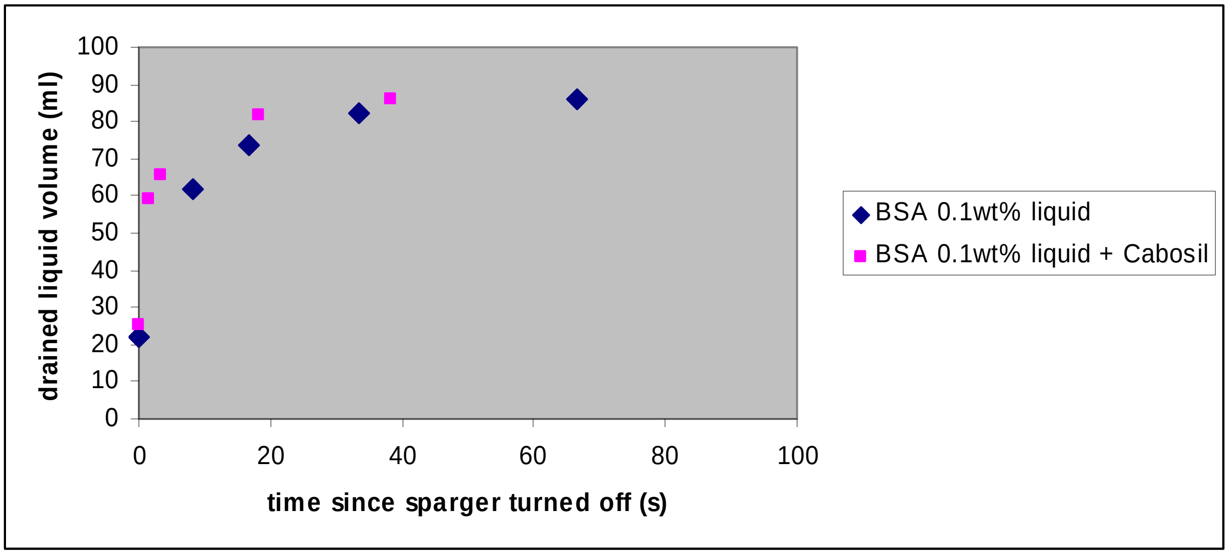

Figure 72: Rate of liquid drainage of BSA solution with and without Cabosil.

4.3. The Influence of Surface Rheology

Table 3 shows a summary of the foaming and rheology studies. An indication of a foam's resistance to drainage is the time for the initial water fraction in the foam to reduce by one-half. Likewise, an indication of a foam's resistance to bubble breakage is the time for the foam to collapse to half of its initial height. Also in the table are approximate values of shear modulus at long times (approximately 1 hour) and a frequency of 0.1 Hz and dilatational modulus at long times and a frequency of 0.5 Hz, where these measurements are available. Of course, it is debatable whether measurements taken after aging of a surfactant layer and after shearing for another length of time should be relevant to the relatively fast processes of foaming and foam collapse. Nevertheless, some interesting observations can be made.

One can see that across families of surfactants the dilatational modulus is not a good predictor of foam stability (Table 3, Figure 73, Figure 74). For example, F108 without a doubt makes a more stable foam than $C_{12}E_8$ at any of the concentrations studied. However, $C_{12}E_8$ has a higher dilatational modulus. However, increasing the concentration of a particular surfactant also increases the measured surface moduli and the foam stability in general. This lack of correlation between different surfactant species indicates that there are multiple factors in addition to the surface rheology that affect the foam stability (gas permeability, repulsion between parallel gas-liquid interfaces, surface tension, etc.). When the concentration of a single surfactant is increased, maintaining similar chemical interactions, the foam rate decreases, drainage slows, and the foam stability increases.

Of the three types of proteins, foams stabilized with β-casein were the longest lasting. This is in contrast to Blijdenstein and colleagues (2010) who observed, for foams of approximately 50% air, where they were trying to minimize effects of drainage and coalescence, that β-casein foams coarsened in 40 minutes while β-lactoglobulin foams coarsened in 70 minutes. However, the main mechanism our foams are undergoing seems to be collapse rather than coarsening:

Although we did not directly measure the bubble sizes of the protein stabilized foams with time, to the eye the bubble sizes did not increase greatly before the foam totally collapsed. Bubble size measurements are recommended in the future. Moreover, Blijdenstein's solution of β-lactoglobulin contained five times the amount of protein as ours in order to reach the desired volume fraction of air. Again for these systems, Blijdenstein reported a surface shear modulus an order of magnitude lower for β-casein than β-lactoglobulin. Although the weight fraction of the two proteins were the same, our measurements for the shear modulus agree fairly well with Blijdenstein's. For the dilatational modulus at 0.01Hz Blijdenstein report a value of 43 for β-lactoglobulin and 25 for β-casein. Unfortunately, we did not measure dilatational properties of these two systems.

Summarizing these results, it appears that for a constant weight of protein, increasing shear modulus increase the time it takes for the foam to drain for BSA and β-lactoglobulin. However, the β-casein is very stable and has the smallest shear modulus. Germick et al. (1994) also observed that globular proteins such as BSA drained faster than casein. An interesting anomaly is also seen in the addition of particles to the BSA solution. The particles increase the foam lifetime overall, but also increase the rate of liquid drainage initially. The surface shear modulus is again lower with the particles. Within a family of surfactants like the $C_{12}E_8$ and the Pluronics, a higher dilatational modulus is associated with longer lasting foams, both slowing liquid drainage and foam collapse. However, one cannot predict foam longevity with surface rheology across family lines.

We also observe that, in general, if the surfactant adsorbs irreversibly to the interface it results in increased stability. Large macromolecules like F108 or proteins that denature when they adsorb reside permanently at the surface, whereas small molecules like L31 and $C_{12}E_8$ can rapidly hop on and off the interface.

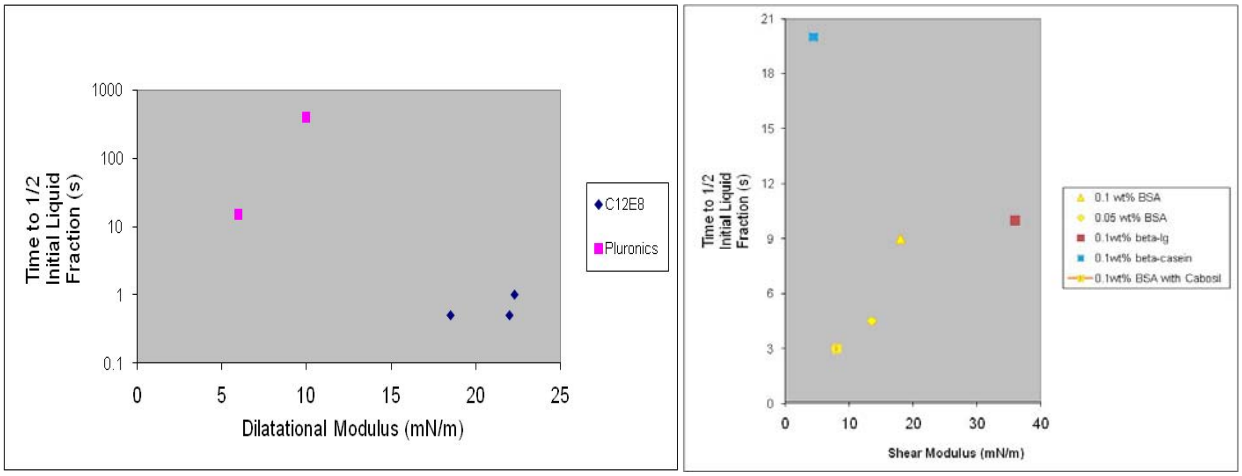

Figure 73. The liquid drainage rate of foams compared to the rheological properties (dilatational modulus, left, and shear modulus, right) measured of the surfactant solution.

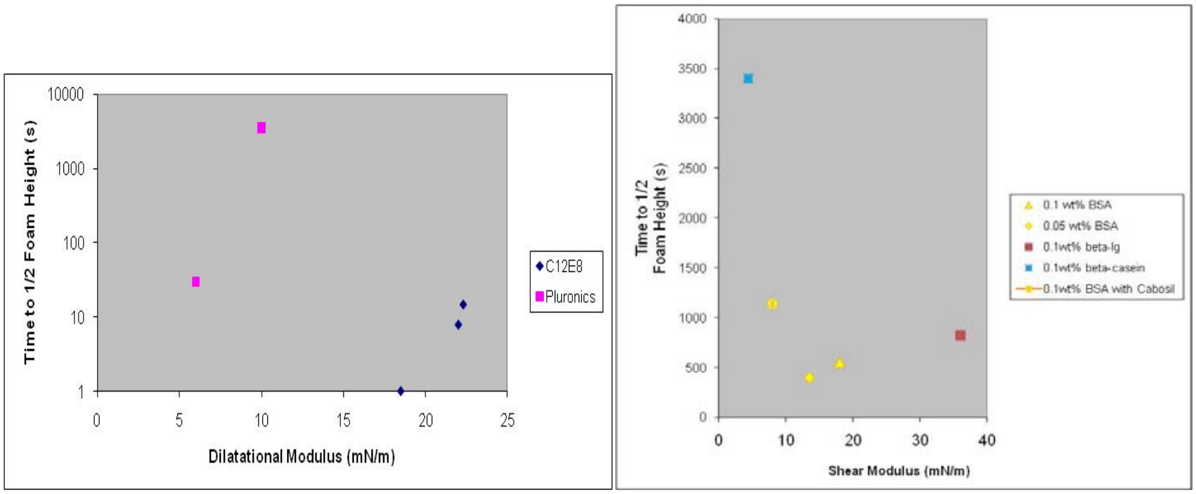

Figure 74. The time for foam to collapse compared to the rheological properties measured of the surfactant solution.

Table 3. Summary of Foaming Studies

Material	**Conc.**	G_s **(mN/m) (0.1 Hz)**	K_s **(mN/m) (0.5 Hz)**	**Initial H_2O fraction**	**Foam time (s)**	**Drain time to ½ initial H_2O fraction (s)**	**Foam collapse time to ½ height (s)**
L31	1 mM		6	0.32	5	15	30
P65	1 mM			0.21	25	150	600
F108	1 mM		10	0.31	55	400	3500
$C_{12}E_8$	2.5 µM		18.5	0.45	N/A	0.5	1
	6 µM		22	0.33	5	0.5	8
	10 µM		22.3	0.3	6	1	15
BSA	0.05 wt.%	13.5	60	0.3	6	4.5	400
	0.1 wt.%	18 8 (ISR)	30	0.32	6	9	550
	0.1 wt. % with 0.5 wt.% Cabosil	8		0.31	6	3	1140
β-lactoglobulin	0.1 wt%	36		0.42	5	10	820
β-casein	0.1 wt%	4.4		0.33	6	20	3400

5. MODELING

This project undertook two primary modeling tasks. The first was to help analysis of data obtained with the ISR. Here, we hope to refine the ability to separate out the bulk rheological response of the system from the surface rheological response. One of the issues that was left unaddressed in earlier studies [Brooks 1999] was the effect of the meniscus on the response of the system. Thus, as one of the initial tasks in this, we undertook to model the curved interfaces with the rheometer within Goma. The details of this work are contained in Appendix C.

Secondly, and the main goal of the numerical work in this project, was to develop the capability to include surface rheological effects in a finite element code, again primarily to be able to separate out the bulk rheological response of a system from the surface rheological response. This capability would help us to interpret the measurements obtained from our equipment, especially in the case of the oscillating drop/bubble apparatus, where a pure dilatational flow field is not produced. Details of the progress made in this area are contained in Appendix D.

It became clear at the end of the program that there were unresolved issues in the formulation that prevented the oscillating bubble problem from being solved correctly. In particular it was found using a heuristic approach that a sign on one of the surface rheology terms had to be flipped in order for the equations to be solved successfully.

$$\boldsymbol{n}\cdot\left(\boldsymbol{T_{in}}-\boldsymbol{T_{ext}}\right)=\begin{aligned}&2H\sigma\boldsymbol{n}+\nabla_s\sigma+2H\boldsymbol{n}(\kappa_s+\mu_s)(\nabla_s\cdot\boldsymbol{v})+(\kappa_s+\mu_s)\nabla_s(\nabla_s\cdot\boldsymbol{v})\\&+\mu_s\{\boldsymbol{n}\times\nabla_s[(\nabla_s\times\boldsymbol{v})\cdot\boldsymbol{n}]\}\\&+\mu_s\{2[(\boldsymbol{b}-2H\boldsymbol{I_s}):(\nabla_s\boldsymbol{v})]\boldsymbol{n}-2[(\boldsymbol{b}-2H\boldsymbol{I_s})\cdot(\nabla_s\boldsymbol{v})\cdot\boldsymbol{n}]\}\end{aligned}\tag{5.1}$$

It’s recommended that an approach based on returning to a raw formulation of the surface stresses be used. The starting condition for this formulation would be the following equation.

$$\boldsymbol{n}\cdot\left(\boldsymbol{T_{in}}-\boldsymbol{T_{ext}}\right)=\nabla_s\left\{\sigma\boldsymbol{I_s}+(\kappa_s-\mu_s)(\boldsymbol{I_s}:\boldsymbol{D_s})\boldsymbol{I_s}+2\mu_s\boldsymbol{D_s}\right\}\tag{5.2}$$

In this formulation the shell variables to be used would be the individual components of $\boldsymbol{D}_s$, of which there are 6 (because it’s symmetric). We are guessing here that using the raw surface strain components $\boldsymbol{D}_s$ should be less problematic just as using the raw bulk strain tensor is less problematic for bulk viscosity formulations.

6. CONCLUSIONS AND OUTLOOK

Interfacial properties are distinct from bulk properties on either side of the boundary, are not well understood, and are difficult to predict. Although interfacial properties have been studied for some time, the complexities of interactions among surfactant molecules, adsorption characteristics, dependence on the geometry of the interface, and the inherent multiscale nature of interfaces mean that much interfacial physics remains a mystery. This project aimed to extend our knowledge by developing experimental and numerical techniques to probe the rheology of interfaces.

We established unique laboratory capabilities by coupling information obtained using shear and dilatational interfacial stress rheometers with optical trapping and manipulation of microparticles (a novel Micro-Interfacial Rheometer) to provide cutting-edge experimental discovery necessary to extend current computational models. Gathering data with multiple techniques was shown to be a necessity in many cases, as each technique had different limitations and sensitivities.

We experimentally investigated the surface rheological properties of surfactant solutions, as well as the stability of foams made with these solutions, to extend our physical knowledge of multiphase flows and guide the development of constitutive models for the mechanical behavior of interfaces. We attempted to correlate the measured surface rheology to the foamability of various surfactant systems. The addition of particles increase the foam stability of a protein surfactant. Increasing the concentration of surfactant increased the dilatational rheology and foam stability, but comparisons between different families/classes of surfactant indicate no clear requirements (e.g. a minimum dilatational or shear modulus). This indicates that there are multiple mechanisms that affect the stability of foams in addition to the surface rheology.

Newly developed constitutive models were incorporated into Sandia's multiphysics codes; however, the computations proved difficult to converge. Suggestions for improvements to the implementation were made. Currently, no commercially available code can include surface rheological effects; therefore, when completed this work will result in a unique capability for Sandia. The new experimental techniques can provide future measurements important to other computational capability development in progress such as the ability to predict interactions between emulsifying agents used in foam processes or nanoparticle interactions in suspensions, where the physics is dominated by the thin films of the continuous phase.

7. OTHER PUBLICATIONS PRODUCED AS PART OF THIS PROJECT

H. K. Moffat and R. R. Rao, memo to Distribution, “Calculating the Meniscus in the Magnetic Rod Interfacial Stress Rheometer,” January 13, 2008.

H. K. Moffat and R. R. Rao, memo to Distribution, “Exercising the Surface Rheology Capabilities in Goma,” April 20, 2008.

S. Reynaert, C.F. Brooks, P. Moldenaers, J. Vermant, G.G. Fuller “Analysis of the Magnetic Rod Interfacial Stress Rheometer,” *Journal of Rheology* **52**, 261-285 (2008).

“Physics of Liquid Interfaces,” *Science Matters*, Sandia National Laboratories, August 2008.

T. P. Koehler, C. M. Brotherton, and A. M. Grillet, “Comparison of Interparticle Force Measurement Techniques Using Optical Trapping,” submitted to Langmuir.

T. P. Koehler, M. A. Yaklin, E. S. Wong, C. F. Brooks, A. M. Grillet and L. A. Mondy, “Experimental Measurements of Interfacial Rheology,” Joint 83rd CSSS and 13th IACIS International Conference on Surface and Colloid Science (ICSCS), Columbia University, New York, NY, June 14-19, 2009.

C. Brooks, A. Grillet, L. Mondy, M. Yaklin, T. Koehler, R. Cote, “Experimental Rheological Measurements at Gas-Liquid Interfaces,” 81st Meeting of the Society of Rheology, Madison, WI, October 18-22, 2009.

A. Grillet, C. Brooks, T. Koehler, M. Yaklin, L. Mondy, M. Reichert, R. Cote, J. Castaneda “Interfacial Rheology and Foam Stability,” Gordon Research Conference on Colloidal, Macromolecular & Polyelectrolyte Solutions, Ventura, CA, February 21-26, 2010.

M. Reichert, L. Walker, C. Brooks, A. Grillet, and L. Mondy, “Effect of surfactant concentration on surface dilatational rheology measurements of oppositely charged polyelectrolyte-surfactant aggregates at the air-liquid interface,” 84th Annual American Chemical Society Colloids Meeting, Akron, OH, June 21-23, 2010.

M. Reichert, L. Walker, C. Brooks, A. Grillet, and L. Mondy, “Connecting surface dilatational rheology with surfactant diffusion to and from the air-liquid interface,” 84th Annual American Chemical Society Colloids Meeting, Akron, OH, June 21-23, 2010.

Lisa Mondy, Carlton Brooks, Anne Grillet, Timothy Koehler, Melissa Yaklin, Jaime Castañeda, Ray Cote, Matt Reichert, Lynn Walker, “Experimental Measurements of Interfacial Rheology Using Several Techniques,” 5th Pacific Rim Conference on Rheology, Sapporo, Japan, August 1-6, 2010.

L. Mondy, C. Brooks, A. Grillet, T. Koehler, M. Yaklin, M. Reichert, R. Cote, J. Castaneda, “Surface Rheology and Interface Stability,” LDRD Day Symposium, Albuquerque, NM, September 9, 2010.

8. REFERENCES

1. Al-Hadithi, T.S.R.; Barnes, H.A.; Walters, K.; *Colloid and Polymer Science* **270**, 40 (1992).
2. Alvarez, N.; Walker, L.; Anna, S.; *Phys. Rev. E* **82**, Issue #1 (2010).
3. Atencia, Javier and Beebe, D.; *Nature* **437**, 648-654 (2005).
4. Bantchev, G. B.; Schwartz, D. K.; *Langmuir* **19**, 2673 (2003).
5. Bergeron, V. ; Langevin, D. ; Asnacios, A.; *Langmuir* **12**, 1550 (1996).
6. Biggs, S.; Kline, S. R.; Walker, L. M.; *Langmuir* **20**, 1085 (2004).
7. Bonfillon, A.; Sicoli, F.; Langevin, D.; J. *Colloid and Interface Sci.* **168**, 497 (1994).
8. Blijdenstein, T. B. J.; de Groot, P. W. N.; Stoyanov, S. D.; *Soft Matter* **6**, 1799 (2010).
9. Brooks, C.F.; Fuller, G.G.; Frank, C.W.; Robertson, C.R.; *Langmuir* **15**, 2450 (1999).
10. Brooks, C.F.; "An Interfacial Stress Rheometer to Study the Shear Rheology of Langmuir Monolayers", Ph.D. Thesis, Stanford University, Stanford, 1999.
11. Clint, Neustadter, Jones; *Dev. Petro. Sci.* **13**, 135 (1981).
12. Cooke, D. J.; Dong, C. C.; Lu, J. R., Thomas; R. K., Simister, E. A., and Penfold, J., *J. Phys. Chem. B* **102**, 4912 (1998).
13. Crocker, J.C., Valentine, M.T.; Weeks, E.R.; Gisler, T.; Kaplan, P.D.; *Phys. Rev. Lett.* **85**, 888 (2000).
14. Espinosa, G and Langevin, D.; *Langmuir* **25**, 12201 (2009).
15. Folmer, B. M. and Kronberg, B.; *Langmuir* **16**, 5987 (2000).
16. Franck, A. ; TA Instruments Application Note APN012 (2010).
17. Freer, E. M.; Svitova, T.; Radke, C. J.; *J. Petroleum Sci. and Eng.* **39**, 137 (2003).
18. Freer, E. M.; Yim, K. S; Fuller, G. G.; Radke, C. J.; *J. Phys. Chem. B* **108**, 3835 (2004).
19. Fruhner, H.; Wantke, K.-D.; Lunkenheimer, K.; *Coll. and Surf. A*, **162**, 193 (1999).
20. Georgieva, D.; Cagna, A.; Langevin, D.; *Soft Matter* **5**, 2063 (2009).
21. Germick, R. J; Rhehill, A. S.; and Narsimhan G, *J. Food Eng.* **23**, 555 (1994).
22. Gottier, G.; Amundson, N.; Flumerfelt, R.; *J. Coll. Int. Sci.* **114**, 106 (1986).
23. Grillet, A.M.; Koehler, T.P.; Brotherton, C.M.; Bell, N.S.; Gorby, A.D.; Reichert, M.D.; Molecke, R.A.; Brinker, C.J.; Bogart, K.A.; Dufresne, E.; Merrill, J.; Sainis, S.; Park, J.-G.; Dunn, E.; Furst, E.M.; Mittal, M.; Lele, P.; Singh, J.; SAND2009-6163 (2009).
24. Hodges, C. S.; Biggs, S.; Walker, L. M.; *Langmuir* **25**, 4484 (2009).
25. Hsu, C. T.; Shao, M. J.; Lee, Y. C.; Lin, S. Y.; *Langmuir* **16**, 4846 (2000).
26. Kline, S.; *Langmuir* **15**, 2726 (1999).
27. Kristen, N. and von Klitzing, R.; *Soft Matter* **6**, 849 (2010).
28. Kropka, J. M.; Celina, M.; Mondy, L. A.; "Rheological Characterization of Foam Morphology and Methods to Control the Morphological Stability," APS March Meeting, Pittsburgh, March 16-20, 2009.
29. Kuntz, D. M. and Walker, L. M.; *J. Phys. Chem. B* **111**, 6417 (2007).
30. Kuntz, D. M. and Walker, L. M.; *Soft Matter* **4**, 286 (2008).
31. Kuntz, D. M. and Walker, L. M.; *Ind. Eng. Chem. Res.* **48**, 2430 (2009).
32. Liggieri, L.; Ferrari, M.; Massa, A.; Ravera, F.; *Coll. and Surf. A* **156**, 455 (1999).
33. Lin, S. Y. ; Chen, L. J. ; Xyu, J. W. ; Wang, W. J. ; *Langmuir* **11**, 4159 (1995).
34. Lin, S. Y.; Wang, W. J.; Lin, L. W.; Chen, L. J; *Colloids Surf.* **114** (1996).

35. Lin, S.; Lin, Y.; Chen, E.; Hsu, C.; Kwan, C.; *Langmuir* **15**, 4370 (1999).
36. MacLeod, C.; Radke, C.; *J. Coll. Int. Sci.* **166**, 73 (1994).
37. Mason, T. G.; Weitz, D.A.; *Phys. Rev. Lett.* **74**,1250 (1995).
38. Moffat, H. K.; Rao, R. R.; memo to Distribution, “Calculating the Meniscus in the Magnetic Rod Interfacial Stress Rheometer,” January 13, 2008a.
39. Moffat, H. K.; Rao, R. R.; memo to Distribution, “Exercising the Surface Rheology Capabilities in Goma,” April 20, 2008b.
40. Mondy, L. A.; Celina, M.; Kropka, J.; Rao, R. R.; Russick, E.; Giron, N.; Cote, R.; Castaneda, J.; Aubert, J.; SAND2010-6868 (2010).
41. Monteux, C. ; Fuller, G. ; Bergeron, V. ; *J. Phys. Chem. B* **108**, 16473 (2004).
42. Nararajan, R.; Wasan, D; *J. Coll. Int. Sci.* **159**, 164 (1993).
43. Pan, R.; Green, J.; Maldarelli, C.; *J. Coll. Int. Sci* **205**, 213 (1998).
44. Park, B. J.; Patina J. P.; Furst, E. M.; Oettel, M.; Reynaert, S.; Vermant, J.; *Langmuir* **24**, 1686 (2008).
45. Prasad, V.; Weeks, E.R.; *Phys. Rev. Lett.* **102**, 178302 (2009).
46. Prins, A; *Coll. And Surf A* **149**, 467 (1999).
47. Purcell, I. P.; Lu, J. R.; Thomas, R. K.; Howe, A. M.; and Penfold, J.; *Langmuir* **14**, 1637 (1998).
48. Purcell, I. P., Thomas, R. K., Penfold, J., and Howe, A. M., *Colloids Surf.* **94**, 125 (1995).
49. Pugh, R. J.; *Adv. Colloid Interface Sci.* **64**, 67 (1996).
50. Ravera, F.; Liggieri, L.; LoglioV; Dilatational Rheology of Adsorbed Layers by Oscillating Drops and Bubbles, in “Interfacial Rheology”, R. Miller and L. Liggieri (Eds.), Brill, Leiden, 2009.
51. Renardy, M.; *J. Non-Newt. Fluid Mech.* **68**, 125 (1997).
52. Reynaert, S.; Brooks, C.F.; Moldenaers, P.; Vermant, J.; Fuller, G.G.; *J. Rheology* **52**, 261 (2008).
53. Saffman, P.G.; *J. Fluid Mech.* **73**(4), 593 (1976).
54. Squires T.M.; Mason, T.G.; *Annu. Rev. Fluid Mech.* **42**, 413 (2010).
55. Stubenrauch, C.; Shrestha, L. K.; Varade, D.; Johansson, I.; Olanya, G.; Aramaki, K.; Claesson, P.; *Soft Matter*, **5**, 3070, 2009.
56. Svitova, T. F.; Wetherbee, M. J.; Radke, C. J.; *J. Colloid and Interface Sci.* **261**, 170 (2003).
57. Takei H.; Shimizu, N.; *Langmuir* **13**(7), 1865 (1997).
58. Tamura, T.; Kaneko, Y.; Ohyama, M.; *J. Colloid and Interface Sci.* **173**, 493 (1995).
59. Tan, S. N.; Jiang, A.; Liau, J. J.; Grano, S. R.; Horn, R. G., *Int. J. Miner. Process.* **93**, 194 (2009).
60. Tsay, R. Y.; Lin, S. Y. ; Lin, L. W. ; Chen, S. I. ; *Langmuir* **13**, 3191 (1997).
61. Tsay, R. Y.; Wu, T. F.; Lin, S. Y.; *J. Phys. Chem. B* **108**, 18623 (2004).
62. Wilson, A. J.; Experimental Techniques for the Characterization of Foams, in “Foams: Theory, Measurments, and Applications,” R. K. Prud’homme and S. A. Khan (Eds.), Marcel Dekker, Inc., New York, 1996.
63. Zholob, S.A.; Kovalchuk, V.I.; Makievski, A.V.; Krägel, J.; Fainerman, V.B.; Miller, R.; Determination of the Dilatational Elasticity and Viscosity from the Surface Tension Response to Harmonic Area Perturbations, in “Interfacial Rheology”, R. Miller and L. Liggieri (Eds.), Brill, Leiden, 2009.

APPENDIX A: MEASURING SURFACE TENSION FROM PENDANT DROP PROFILES

Figure 75 shows a cross-sectional view of a pendant drop. Due to symmetry we choose a cylindrical coordinate system,with z the axial coordinate and x the radial coordinate, and for convenience we locate the origin at the apex of the drop. In addition, we also define an arc length coordinate, s, which is the distance of the drop controur from the origin (apex). The x-z coordinates of the droplet profile can be expressed as functions of the parameter s. The angle that the surface tangent makes with the x-axis is ϕ, which is also the angle of the surface normal with respect to the z-axis.

The Young-Laplace equation states that the pressure drop across a curved interface is

$$\Delta P = P_{\mathrm{int}\,ernal} - P_{external} = \sigma\left(\frac{1}{R_1}+\frac{1}{R_2}\right) \tag{A.1}$$

Where R_1 and R_2 are the principal radii of curvature. For our purposes we will choose R_1 to be the principal curvature in the x-z plane and R_2 the principal curvature perpendicular to this plane.

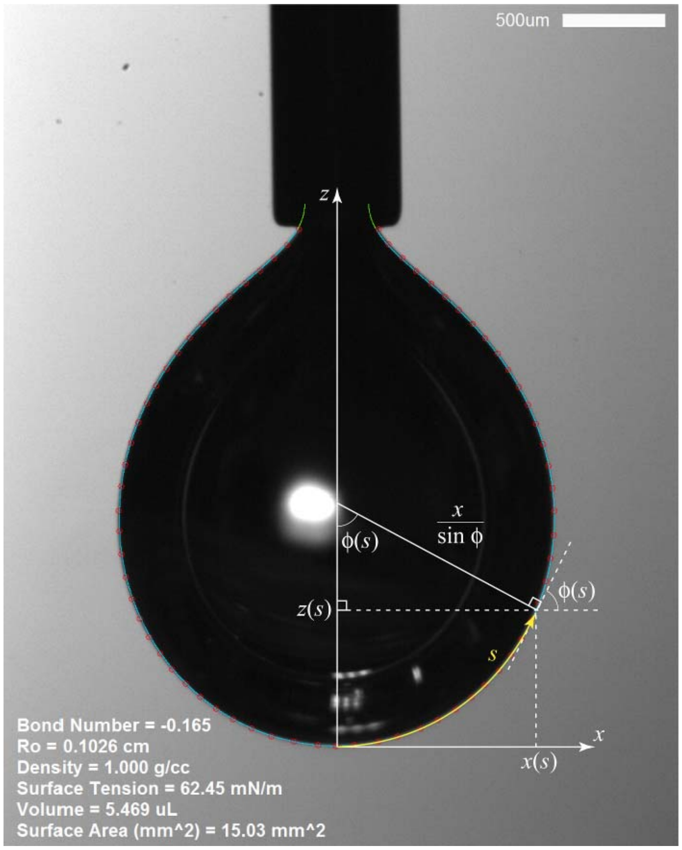

Figure 75: A pendant drop image indicating the coordinate system used for determining the surface tension. The drop shape is fit to a solution of the Young-Laplace equation. The red circles are the subset of points used for the curve fit and the blue curve is the resulting fit.

At the apex (s=0), both radii of curvature are equal to a value we will call R_0.

$$\Delta P(s=0)=\frac{2\sigma}{R_0} \tag{A.2}$$

At higher elevations from the apex, there will be an additional hydrostatic term due to gravitational effects arising from the difference in densities

$$\Delta P(s)=\frac{2\sigma}{R_0}+g\Delta\rho z(s) \tag{A.3}$$

Where $\Delta\rho=\rho_{external}-\rho_{\mathrm{int}\,ernal}$. Equations A.1 and A.3 for the pressure drop are equivalent:

$$\Delta P(s)=\frac{2\sigma}{R_0}+g\Delta\rho z(s)=\sigma\left(\frac{1}{R_1}+\frac{1}{R_2}\right). \tag{A.4}$$

Substituting in expressions for the two principal radii of curvature $\frac{1}{R_1}=\frac{d\phi}{ds}$ and $\frac{1}{R_2}=\frac{\sin\phi}{x}$ into eqn. A.4

$$\frac{2\sigma}{R_0}+g\Delta\rho z(s)=\sigma\left(\frac{d\phi}{ds}+\frac{\sin\phi}{x(s)}\right), \tag{A.5}$$

and solving for $d\phi/ds$ yields

$$\frac{d\phi}{ds}=\frac{2}{R_0}+\frac{g\Delta\rho}{\sigma}z(s)-\frac{\sin\phi}{x(s)}. \tag{A.6}$$

From the geometry, we can also write

$$\frac{dx}{ds}=\cos\phi \tag{A.7}$$

$$\frac{dz}{ds}=\sin\phi \tag{A.8}$$

Equations A.6-A.8 make a first order system of non-linear differential equations, with initial conditions $x(0)=z(0)=\phi(0)=0$. When these are integrated we obtain the equilibrium drop profile.

It is convenient to choose R_0 as a characterisitic length scale. If we let $\bar{x}=x/R_0$, $\bar{z}=z/R_0$, and $\bar{s}=s/R_0$ eqns. A.6-A.8 become

$$\frac{d\phi}{d\bar{s}}=2+N_{\mathrm{Bd}}\bar{z}(\bar{s})-\frac{\sin\phi}{\bar{x}(\bar{s})} \tag{A.9}$$

$$\frac{d\bar{x}}{d\bar{s}}=\cos\phi \tag{A.10}$$

$$\frac{d\bar{z}}{d\bar{s}} = \sin\phi \tag{A.11}$$

where we have defined a dimensionless Bond number as:

$$N_{\mathrm{Bd}} = \frac{g\Delta\rho R_0^2}{\sigma} \tag{A.12}$$

Integrating A.9-A.11 with the rescaled initial conditions, $\bar{x}(0) = \bar{z}(0) = \phi(0) = 0$, generates a series of curves that are only a function of N_{Bd}. Figure 76 shows a series of profiles for pendant drops ($N_{\mathrm{Bd}} < 0$).

Drop profiles are fit using an optimization routine [Rotenberg et al. 1983] that determines the location of the apex (offsets for the *x* and the *z* coordinates), scaling factor (R_0), and shape (N_{Bd}). With these optimized values of R_0 and N_{Bd} and knowledge of the density difference and gravity, the surface tension can be calculated from eqn. A.12:

$$\sigma = \frac{g\Delta\rho R_0^2}{N_{\mathrm{Bd}}} \, . \tag{A.13}$$

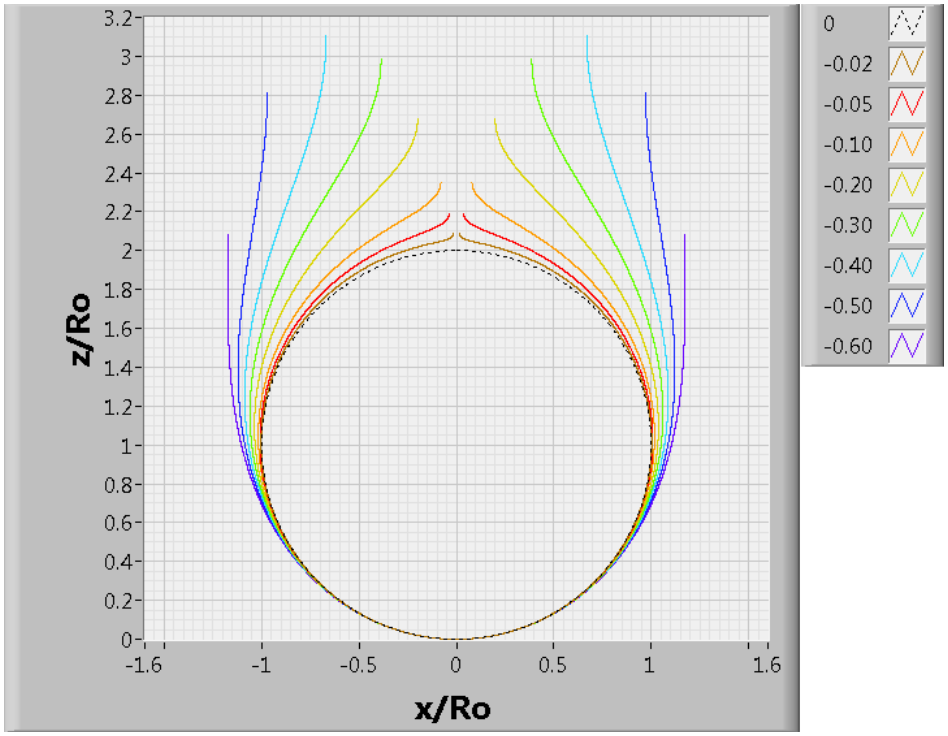

Figure 76: Pendant drop profiles for different values of N_{Bd}.

The same set of equations can be used to determin the shapes of sessile droplets, where the buoyancy force is pushing the drop toward a flat surface. Figure 77 shows a series of profiles for sessile drops ($N_{\mathrm{Bd}} > 0$).

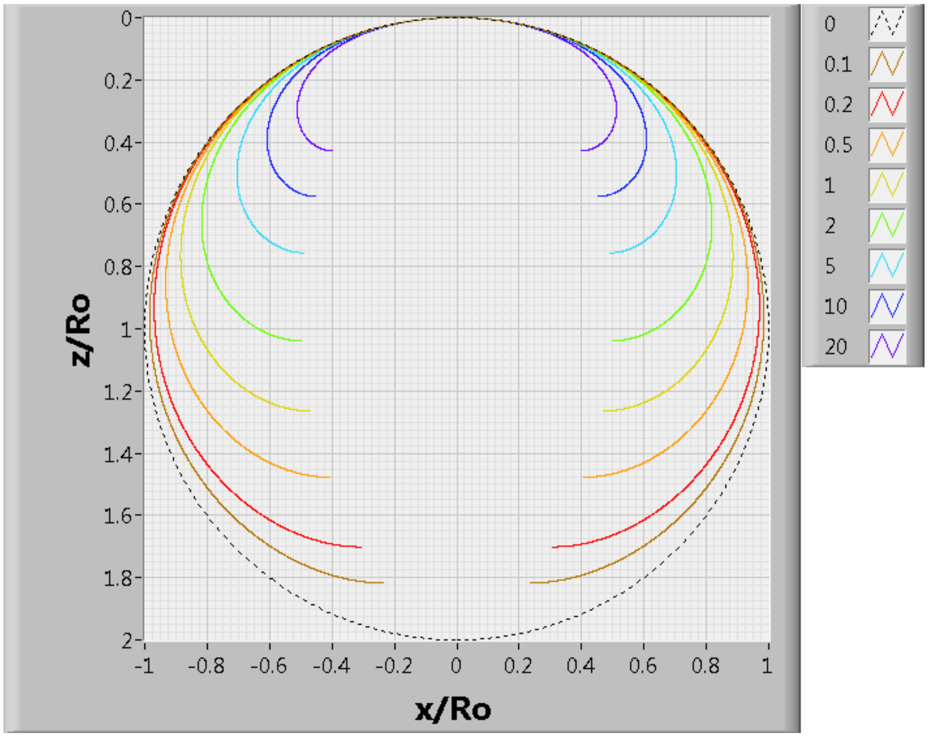

Figure 77: Sessile drop profiles for different values of N_{Bd}.

References

- F. Bashforth, J.C. Adams, An Attempt to Test the Theories of Capillary Action, University Press, Cambridge, 1883.
- H.M. Princen, The Equilibrium Shape of Interfaces, Drops, and Bubbles. Rigid and Deformable Particles at Interfaces, in “Surface and Colloid Science”, vol. 2, E. Matijević (Ed.), Wiley-Interscience, New York, **1969**.
- Y. Rotenberg , L. Boruvka, A.W. Neumann *J. Colloid and Interface Sci.* **1983**, *93*, 169.
- S.H. Anastasiadis, J.-K. Chen, J.T. Koberstein, A.F. Siegel, J.E. Sohn, J.A. Emerson *J. Colloid and Interface Sci.* **1983**, *119*, 55
- D.B. Thiessen, D.J. Chione, C.B. McCreary, W.B. Krantz *J. Colloid and Interface Sci.* **1996**, *177*, 658.
- N.J. Alvarez, L.M. Walker, S.L. Anna *J. Colloid and Interface Sci.* **2009**, *333*, 557.

APPENDIX B: RELATIONSHIPS AMONG SURFACE MODULI AND THE SURFACE POISSON'S RATIO

There are relationships between the tensile modulus (*E*), shear modulus (*G*), bulk modulus (*K*), and Poisson's ratio for isotropic bulk materials. If you know any two of these parameters, the other two can be determined. Here we derive similar relationships for an isotropic 2D surface.

Hooke's law for 2D surfaces can be expressed as:

$$\underline{\underline{\varepsilon_s}} = \frac{1}{E_s}\underline{\underline{\sigma_s}} - \frac{\nu_s}{E_s}\left[tr\left(\underline{\underline{\sigma_s}}\right)\underline{\underline{I}} - \underline{\underline{\sigma_s}} \right] \tag{B.1}$$

where $\underline{\underline{\varepsilon_s}}$ is the surface strain tensor, $\underline{\underline{\sigma_s}}$ is the surface stress tensor, E_s is the surface tensile modulus, and ν_s is the surface Poisson's ratio. In component form the two normal and the single shear strains are:

$$\varepsilon_{11}^s = \frac{1}{E_s}\sigma_{11}^s - \frac{\nu_s}{E_s}\sigma_{22}^s \tag{B.2}$$

$$\varepsilon_{22}^s = \frac{1}{E_s}\sigma_{22}^s - \frac{\nu_s}{E_s}\sigma_{11}^s \tag{B.3}$$

$$\varepsilon_{12}^s = \frac{1+\nu_s}{E_s}\sigma_{12}^s \tag{B.4}$$

This can be rewritten in matrix form, using the engineering shear strain $\gamma_{12}^s = 2\varepsilon_{12}^s$

$$\frac{1}{E_s}\begin{bmatrix} 1 & -\nu_s & 0 \\ -\nu_s & 1 & 0 \\ 0 & 0 & 2(1+\nu_s) \end{bmatrix}\begin{bmatrix} \sigma_{11}^s \\ \sigma_{22}^s \\ \sigma_{12}^s \end{bmatrix} = \begin{bmatrix} \varepsilon_{11}^s \\ \varepsilon_{22}^s \\ 2\varepsilon_{12}^s = \gamma_{12}^s \end{bmatrix} \tag{B.5}$$

This can be inverted to solve for the surface stress components in terms of the surface strain components.

$$\frac{E_s}{(1+\nu_s)(1-\nu_s)}\begin{bmatrix} 1 & \nu_s & 0 \\ \nu_s & 1 & 0 \\ 0 & 0 & \dfrac{(1-\nu_s)}{2} \end{bmatrix}\begin{bmatrix} \varepsilon_{11}^s \\ \varepsilon_{22}^s \\ \gamma_{12}^s \end{bmatrix} = \begin{bmatrix} \sigma_{11}^s \\ \sigma_{22}^s \\ \sigma_{12}^s \end{bmatrix} \tag{B.6}$$

We observe that the shear stress component in eqn. B.6 is

$$\sigma_{12}^s = \frac{E_s}{2(1+\nu_s)}\gamma_{12}^s \,. \tag{B.7}$$

From the definition of the shear modulus $\sigma_{12}^s = G_s\gamma_{12}^s$ we obtain an expression of the surface shear modulus in terms of the surface tensile modulus and surface Poisson's ratio

$$\boxed{G_s = \frac{E_s}{2(1+\nu_s)}} \tag{B.8}$$

For positive and finite G_s, eqn. B.8 requires that $\nu_s \geq -1$.

The surface dilatational strain is $\alpha_s = tr(\underline{\underline{\varepsilon_s}}) = \varepsilon_{11}^s + \varepsilon_{22}^s$, and for uniform dilation, $\varepsilon_{11}^s = \varepsilon_{22}^s = \frac{\alpha_s}{2}$. From the definition of the surface dilatational modulus the normal stresses are proportional to the surface dilatational strain

$$\sigma_{11}^s = \sigma_{22}^s = K_s \alpha_s \tag{B.9}$$

Taking the σ_{11}^s normal stress component in eqn. B.6

$$\sigma_{11}^s = \frac{E_s}{(1+\nu_s)(1-\nu_s)}\left(\varepsilon_{11}^s + \nu_s \varepsilon_{22}^s\right) = \frac{E_s}{2(1-\nu_s)}\alpha_s \tag{B.10}$$

Comparing to eqn B.9 we can determine the surface dilatational modulus in terms of the surface tensile modulus and surface Poisson's ratio

$$\boxed{K_s = \frac{E_s}{2(1-\nu_s)}} \tag{B.11}$$

For positive and finite K_s, this requires that $\nu_s \leq 1$. From eqn. B.8 and B.11 the surface Poisson's ratio can be determined in terms of the surface dilatational and shear moduli.

$$\boxed{\nu_s = \frac{K_s - G_s}{K_s + G_s}} \tag{B.12}$$

For an incompressible interface ($K_s \to \infty$), $\nu_s \to 1$. It is also interesting to note that for positive values of ν_s, which is typical for bulk materials and we would expect the same for interfaces, requires that $K_s > G_s$. This is in excellent agreement with values of K_s and G_s for interfaces reported in the literature in the instances where both values are reported.

Also from eqn. B.8 and B.11 the surface tensile modulus can be determined in terms of the surface dilatational and shear moduli.

$$\boxed{E_s = \frac{4K_s G_s}{K_s + G_s}} \tag{B.13}$$

For an incompressible interface ($K_s \to \infty$), $E_s \to 4G_s$, which gives rise to a 2D Trouton's rule. Another interesting observation is that of the three surface moduli, for $0<\nu_s<1$, G_s will always be smaller than both E_s and K_s. Since it is more typical and experimentally convenient to measure K_s and G_s , these relationships can be used to determine E_s and ν_s.

APPENDIX C: EXERCISING THE SURFACE RHEOLOGY CAPABILITIES IN GOMA

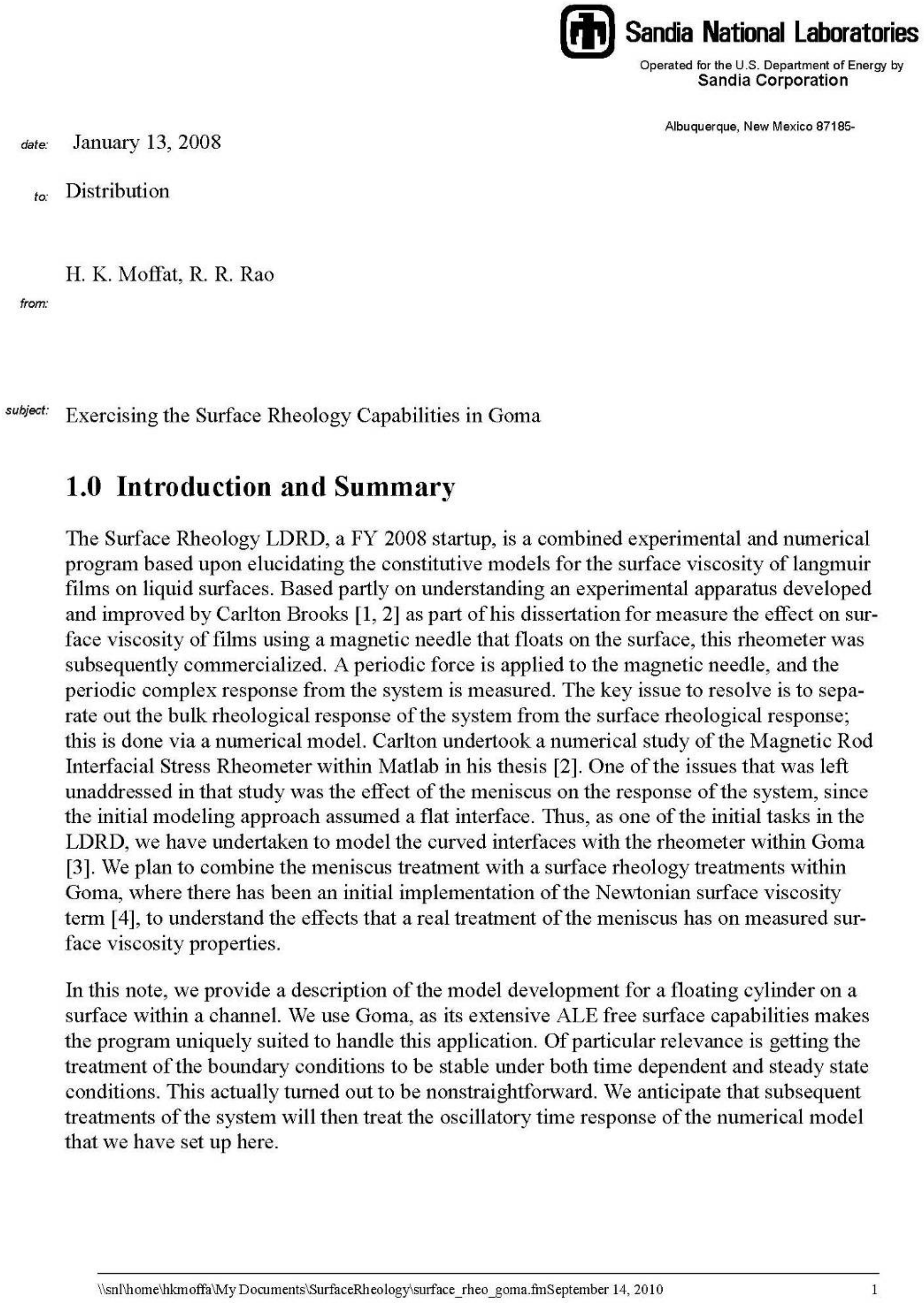

Sandia National Laboratories
Operated for the U.S. Department of Energy by
Sandia Corporation

Albuquerque, New Mexico 87185-

date: January 13, 2008

to: Distribution

from: H. K. Moffat, R. R. Rao

subject: Exercising the Surface Rheology Capabilities in Goma

1.0 Introduction and Summary

The Surface Rheology LDRD, a FY 2008 startup, is a combined experimental and numerical program based upon elucidating the constitutive models for the surface viscosity of langmuir films on liquid surfaces. Based partly on understanding an experimental apparatus developed and improved by Carlton Brooks [1, 2] as part of his dissertation for measure the effect on surface viscosity of films using a magnetic needle that floats on the surface, this rheometer was subsequently commercialized. A periodic force is applied to the magnetic needle, and the periodic complex response from the system is measured. The key issue to resolve is to separate out the bulk rheological response of the system from the surface rheological response; this is done via a numerical model. Carlton undertook a numerical study of the Magnetic Rod Interfacial Stress Rheometer within Matlab in his thesis [2]. One of the issues that was left unaddressed in that study was the effect of the meniscus on the response of the system, since the initial modeling approach assumed a flat interface. Thus, as one of the initial tasks in the LDRD, we have undertaken to model the curved interfaces with the rheometer within Goma [3]. We plan to combine the meniscus treatment with a surface rheology treatments within Goma, where there has been an initial implementation of the Newtonian surface viscosity term [4], to understand the effects that a real treatment of the meniscus has on measured surface viscosity properties.

In this note, we provide a description of the model development for a floating cylinder on a surface within a channel. We use Goma, as its extensive ALE free surface capabilities makes the program uniquely suited to handle this application. Of particular relevance is getting the treatment of the boundary conditions to be stable under both time dependent and steady state conditions. This actually turned out to be nonstraightforward. We anticipate that subsequent treatments of the system will then treat the oscillatory time response of the numerical model that we have set up here.

2.0 Equation System

2.1 Consitutive Modeling For Systems with Excess Surface Properties

A couple of definitions are useful. The surface gradient operator is defined as

$$\nabla_s = (\mathbf{I} - \boldsymbol{nn}) \bullet \nabla \tag{1}$$

We may think of the unity tensor in the above formulation as a combination of three dyadics

$$I = \boldsymbol{nn} + \boldsymbol{t_1 t_1} + \boldsymbol{t_2 t_2} \tag{2}$$

$\boldsymbol{n}$ is the local normal to the surface. Where there is an inner surface and an exterior domain, $\boldsymbol{n}$ is defined within Goma as always pointing from the inner domain out into the outer domain (or exterior). $\boldsymbol{t_1}$ and $\boldsymbol{t_2}$ are local tangents to the surface defined in such a way that $\boldsymbol{n}$, $\boldsymbol{t_1}$, and $\boldsymbol{t_2}$ form an orthonormal basis at every point. Frequently, the symbol $\mathbf{I}_s$, the surface idemfactor tensor, is defined to represent direction which are in the plane of the surface.

$$\mathbf{I}_s = \mathbf{I} - \boldsymbol{nn} = \boldsymbol{t_1 t_1} + \boldsymbol{t_2 t_2} \tag{3}$$

The interfacial shear, $\mathbf{D}_s$, is a tensor defined in the plane of the surface and may be expressed as

$$\mathbf{D}_s = \frac{1}{2}[(\nabla_s \boldsymbol{v}) \cdot \mathbf{I}_s + \mathbf{I}_s \cdot (\nabla_s \boldsymbol{v})^T] \tag{4}$$

Note the dot product within Eqn. (4) combines the inner indeces of the two tensors, $(\nabla_s \boldsymbol{v})$ and $\mathbf{I}_s$ to create another tensor. This inner product is needed in order to crop the velocity changes in the normal direction which $\nabla_s \boldsymbol{v}$ actually contains. An example is useful. For cartesian coordinates, with the surface oriented in the **x** direction, $\mathbf{D}_s$ is equal to

$$\mathbf{D}_s = \begin{bmatrix} 0 & 0 & 0 \\ 0 & \dfrac{dv_y}{dy} & \dfrac{1}{2}\left(\dfrac{dv_y}{dz} + \dfrac{dv_z}{dy}\right) \\ 0 & \dfrac{1}{2}\left(\dfrac{dv_z}{dy} + \dfrac{dv_y}{dz}\right) & \dfrac{dv_z}{dz} \end{bmatrix} \tag{5}$$

The Boussinesq Scriven model for surface rheological properties for a Newtonian approximation to the surface is given by the following formulation. $\underline{\boldsymbol{\Upsilon}}_s$ is the surface stress tensor.

$$\underline{\boldsymbol{\Upsilon}}_s = \sigma \mathbf{I}_s + \boldsymbol{\tau}_s = \sigma \mathbf{I}_s + (\kappa_s - \mu_s)(\mathbf{I}_s : \mathbf{D}_s)\mathbf{I}_s + 2\mu_s \mathbf{D}_s \tag{6}$$

The expression $\mathbf{I}_s : \mathbf{D}_s$ is actually identified as the trace of $\mathbf{D}_s$, i.e., the diagonal components oriented in the surface plane summed up.

$$\mathbf{I}_s : \mathbf{D}_s = tr(\mathbf{D}_s) = \nabla_s \cdot \boldsymbol{v} \tag{7}$$

For the example mentioned in Eqn. 5, the trace would be equal to Eqn. (8).

$$\mathbf{I}_s : \mathbf{D}_s = tr(\mathbf{D}_s) = \nabla_s \cdot \boldsymbol{v} = \frac{dv_y}{dy} + \frac{dv_z}{dz} \tag{8}$$

We note that in contrast to the full divergence of the velocity for incompressible flows, the surface divergence will easily allow for nonzero cases. A good example of dilatational flow would be a balloon expanding and contracting.

The surface excess stress tensor, also called the surface excess pressure, may be related to the bulk fields by the following expression obtained from Edward's book.

$$-(\boldsymbol{n} \cdot \|\boldsymbol{T}\|) = \boldsymbol{F}_s + \nabla_s \cdot \underline{\boldsymbol{\Upsilon}}_s = \boldsymbol{n} \cdot (\boldsymbol{T}_{in} - \boldsymbol{T}_{ext}) \tag{9}$$

Note, the Edwards book uses the nomenclature $\|\boldsymbol{T}\| = T_{n=0+} - T_{n=0-}$, where the normal $\boldsymbol{n}$ dictate the direction of the interface. $\boldsymbol{T}_{in}$ is the bulk-fluid stress tensor in the $n = 0-$ direction of the interface. This is usually thought as tthe inside of the domain. $\boldsymbol{T}_{ext}$ is the stress tensor in the exterior of the domain.

2.2 Goma's Base Treatment : No Surface Excess Properties

We find it's useful to start off by describing Goma's base treatment where the surface "only" exhibits an isotropic surface tension, σ. The surface tension may be a function of the state of the two bulk fluids, 1 and 2, that are on either side of the interface $\sigma = \sigma(T, P, X_1, X_2)$. We start with the fluid momentum equation where the mesh is moving with velocity $\boldsymbol{v}_m$.

$$\rho\frac{d\boldsymbol{v}}{dt} + \rho(\boldsymbol{v} - \boldsymbol{v}_m) \cdot \nabla\boldsymbol{v} = \nabla \cdot \boldsymbol{T} + \boldsymbol{f} \tag{10}$$

where

$$\boldsymbol{T} = -p\boldsymbol{I} + 2\mu\boldsymbol{D} - \left(\frac{2}{3}\mu - \kappa\right)(\nabla \cdot \boldsymbol{v})\boldsymbol{I} \tag{11}$$

and the symmetric shear tensor, $\boldsymbol{D}$, may be represented by Eqn. (12).

$$\boldsymbol{D} = \frac{1}{2}(\nabla\boldsymbol{v} + (\nabla\boldsymbol{v})^T) \tag{12}$$

Residual equations for the β^{th} component of the momentum equations are then created by setting the momentum equation's error orthogonal to a set of basis functions, ϕ_i, and then integrating by parts to formulate an expression for the residual of the β^{th} component of the momentum equation with respect to the basis function ϕ_i, $R_i^{m,\beta}$, Eqn. (13).

$$\begin{aligned} R_i^{m,\beta} &= -\int_V \left(\phi_i \boldsymbol{e}_\beta \cdot \left(\rho \frac{d\boldsymbol{v}}{dt} + \rho(\boldsymbol{v} - \boldsymbol{v}_m) \cdot \nabla \boldsymbol{v} - \boldsymbol{f}\right)\right) dV \\ &\quad - \int_V ((\nabla(\phi_i \boldsymbol{e}_\beta))^T : \boldsymbol{T}) dV + \int_\Gamma (\phi_i \boldsymbol{e}_\beta \boldsymbol{n} : \boldsymbol{T}) d\Gamma \end{aligned} \tag{13}$$

Note, that we have multiplied by -1 to reach Eqn. (13). Goma's residuals formally have negative terms outside their time derivatives (in contrast to about every other code in existence). $\boldsymbol{e}_\beta$ is the unit norm directed in the β component direction, where β may represent a curvilinear coordinate system. Coming from the residual expression in Eqn. (13) the following surface term falls out, involving the stress tensor at the inside of the interface, $\boldsymbol{T}_{in}$.

$$R_i^{m,\beta} = \ldots + \int_{d\Gamma} \phi_i(\boldsymbol{e}_\beta \boldsymbol{n} : \boldsymbol{T}_{in}) d\Gamma \tag{14}$$

In Eqn. (14), $R_i^{m,\beta}$ is the momentum residual for the i^{th} basis function for the coordinate direction, β. The double dot notation in Eqn. (14) is the inner product notation, where the inner indices are contracted by an inner product before the outer indices are contracted.

At an interface with no surface excess properties, the following equation holds from a simpliefication of Eqn. (9) (Note, ref. [7] contains many sign errors and is not to be trusted).

$$\boldsymbol{n} \cdot (\boldsymbol{T}_{in} - \boldsymbol{T}_{ext}) = \nabla_s \cdot (\mathbf{I}_s \sigma) = 2H\sigma \boldsymbol{n} + \nabla_s \sigma \tag{15}$$

Here, $\boldsymbol{T}_{in}$ is the stress tensor within the interior of the fluid. $\boldsymbol{T}_{ext}$ is the stress tensor on the exterior of the other fluid. $\mathbf{I}_s$ is the surface dyadic defined in Eqn. (3), and ∇_s is the surface gradient operator defined in Eqn. (1). $\boldsymbol{n}$ points out of the domain.

Frequently, the fluid in the exterior domain is a gas where the shear stress is negligible, and the value of $\boldsymbol{T}_{ext}$ reduces to $\boldsymbol{T}_{ext} = -\mathbf{I} p_{ext}$, where the minus sign is due to the definition of $\boldsymbol{T}$ (see Eqn. (11)). In this case Eqn. (15) reduces to

$$\boldsymbol{n} \cdot (\boldsymbol{T}_{in}) = -\boldsymbol{n} \cdot \mathbf{I} p_{ext} + 2H\sigma \boldsymbol{n} + \nabla_s \sigma \tag{16}$$

H is the surface mean curvature. It can be related to the surface divergence of the normal vector to the surface [7], and in fact we used this relation in deriving Eqn. (15).

$$2H = -\nabla_s \bullet \boldsymbol{n} \tag{17}$$

We may plug Eqn. (16) into Eqn. (14) to yield Eqn. (18).

$$\int_{d\Gamma} \phi_i(\boldsymbol{e}_\beta \boldsymbol{n} : \boldsymbol{T}_{in}) d\Gamma = -\int_{d\Gamma} \phi_i(\boldsymbol{e}_\beta \bullet n) p_{ext} d\Gamma + \int_{d\Gamma} \phi_i(\boldsymbol{e}_\beta \bullet n) 2H\sigma d\Gamma + \int_{d\Gamma} \phi_i(\boldsymbol{e}_\beta \bullet \nabla_s \sigma) d\Gamma \tag{18}$$

It is desirable to simplify Eqn. (18) to remove explicit calculation of the surface tension gradient and the curvature. The surface divergence theorm relates surface and volume integrals of vector fields on a curved surface. Let Γ be a two dimensional surface. Let C be the one-dimensional line surrounding that surface. Let $\boldsymbol{m}$ be the normal tangent to the surface Γ along the line C that points out of the surface; $\boldsymbol{m}$ is called a binormal. Then, for an arbitray vector field, $\boldsymbol{v}$:

$$\int_{\Gamma} (\nabla_s \cdot \boldsymbol{v}) d\Gamma = \int_{C} (\boldsymbol{v} \cdot \boldsymbol{m}) dC - \int_{\Gamma} 2H(\boldsymbol{v} \cdot n) d\Gamma \tag{19}$$

We may apply this to yield

$$\int_{d\Gamma} \phi_i(\boldsymbol{e}_\beta \bullet n) 2H\sigma d\Gamma = \int_{C} \phi_i \sigma(\boldsymbol{e}_\beta \cdot \boldsymbol{m}) dC - \int_{\Gamma} (\nabla_s \cdot (\boldsymbol{e}_\beta \phi_i \sigma)) d\Gamma \tag{20}$$

Then, we may combine to yield

$$\int_{d\Gamma} \phi_i(\boldsymbol{e}_\beta \bullet n) 2H\sigma d\Gamma + \int_{d\Gamma} \phi_i(\boldsymbol{e}_\beta \bullet \nabla_s \sigma) d\Gamma = \int_{C} \phi_i \sigma(\boldsymbol{e}_\beta \cdot \boldsymbol{m}) dC - \int_{\Gamma} \sigma(\nabla_s \cdot (\boldsymbol{e}_\beta \phi_i)) d\Gamma \tag{21}$$

Thus, we have replaced some nasty terms with relatively easy terms that may be calculated explicitly. The final expression becomes

$$\begin{aligned} \int_{d\Gamma} \phi_i(\boldsymbol{e}_\beta \bullet n) 2H\sigma d\Gamma + \int_{d\Gamma} \phi_i(\boldsymbol{e}_\beta \bullet \nabla_s \sigma) d\Gamma &= \\ \int_{C} \phi_i \sigma(\boldsymbol{e}_\beta \cdot \boldsymbol{m}) dC - \int_{\Gamma} \sigma(((\mathbf{I} - \boldsymbol{nn}) \cdot \nabla) \cdot (\boldsymbol{e}_\beta \phi_i)) d\Gamma& \end{aligned} \tag{22}$$

Plugging that back into Eqn. (18) yields Eqn. (23).

$$\begin{aligned} \int_{d\Gamma} \phi_i(\boldsymbol{e}_\beta \boldsymbol{n} : \boldsymbol{T}_{in}) d\Gamma &= -\int_{d\Gamma} \phi_i(\boldsymbol{e}_\beta \bullet n) p_{ext} d\Gamma \\ &- \int_{\Gamma} \sigma((\mathbf{I} - \boldsymbol{nn}) : \nabla(\boldsymbol{e}_\beta \phi_i)) d\Gamma + \int_{C} \phi_i \sigma(\boldsymbol{e}_\beta \cdot \boldsymbol{m}) dC \end{aligned} \tag{23}$$

Note we have replaced the two dot product operations in Eqn. (23) with a single double dot operation, because they are equivalent operations. The double dot operator contracts the inner indecies of the dyadic products first, before it contracts the outer indecies. Eqn. (23) is the expression that Goma has traditionally solved for when handling free surface problems. This includes the treatment of the signs. The surface integral for Eqn. (23) and its derivatives is solved for in the function `fn_dot_T()` in the file `mm_ns_bc.c`. The signs in that function agree with the signs in Eqn. (23). The point boundary condition term in Eqn. (23) is applied on the ends of free surfaces where needed. It is not needed when the contact angle is specified for the free surface.

2.2.1 Reconciliation of Signs

We may prove Eqn. (23) and especially the signs by assuming spherical symmetry, i.e., a bubble geometry. Within that geometry it's widely known that the pressure within the bubble is greater than the pressure outside the bubble.

In spherical coordinates, and assuming symmetry in the θ and ϕ direction, the value of $\nabla(\boldsymbol{e}_r\phi_i)$ may be written as ([9] BSL, p. 837):

$$\nabla(\boldsymbol{e}_r\phi_i) = \frac{\boldsymbol{e}_\theta\boldsymbol{e}_\theta}{r} + \frac{\boldsymbol{e}_\phi\boldsymbol{e}_\phi}{r} \tag{24}$$

We may plug this value into Eqn. (23) using $\boldsymbol{n} = \boldsymbol{e}_r$ to show that

$$\int_\Gamma \sigma((\mathbf{I} - \boldsymbol{nn}) : \nabla(\boldsymbol{e}_\beta\phi_i))d\Gamma = \frac{2\sigma}{r}$$

and therefore Eqn. (23) becomes

$$-p_{in} = -p_{ext} - \frac{2\sigma}{r} \tag{25}$$

This is the expected result for a sphere. Note, for the sphere geometry, the mean curvature H is negative when the normal points out of the sphere. Again, this may be shown, because

$$\nabla(\boldsymbol{n}) = \nabla(\boldsymbol{e}_r) = \frac{\boldsymbol{e}_\theta\boldsymbol{e}_\theta}{r} + \frac{\boldsymbol{e}_\phi\boldsymbol{e}_\phi}{r}$$

$$H = \frac{-\nabla_s \bullet \boldsymbol{n}}{2} = -\frac{1}{2}(I - nn) : \nabla(\boldsymbol{e}_r) = \frac{-1}{r}$$

Plugging the value of H into Eqn. (15) yields the expected relationship.

2.3 Surface Excess Properties: Linkage

Treatment for surfaces with excess properties starts with an expansion of a generalization of Eqn. (15) to include the full Boussinesq-Scriven model, Eqn. (6), for the excess surface stress tensor, $\underline{\boldsymbol{\Upsilon}}_s$. The proof starts with a derivation of the the two dimensional Cauchy's theorum, essentially a force balance on a surface eleemtn. We then ignore the acceleration term and any other body force term which may be acting on the surface element, which is pertinent if the surface phase has an unimportant amount of surface density. The resulting equation is given in Eqn. (26).

$$\boldsymbol{n} \cdot (\boldsymbol{T}_{in} - \boldsymbol{T}_{ext}) = \nabla_s \cdot (\underline{\boldsymbol{\Upsilon}}_s) \tag{26}$$

Note, if the acceleration of surface phase isn't ignored the following equation would hold [2].

$$\frac{d(\rho_s \boldsymbol{v}_s)}{dt} + \nabla_s \bullet (\rho_s \boldsymbol{v}_s \boldsymbol{v}_s) = \nabla_s \cdot (\underline{\boldsymbol{\Upsilon}}_s) - (\boldsymbol{n} \cdot (\boldsymbol{T}_{in} - \boldsymbol{T}_{ext})) \tag{27}$$

Thus,

$$\boldsymbol{n} \cdot (\boldsymbol{T}_{in} - \boldsymbol{T}_{ext}) = \nabla_s \cdot (\sigma \mathbf{I}_s + (\kappa_s - \mu_s)(\mathbf{I}_s : \mathbf{D}_s)\mathbf{I}_s + 2\mu_s \mathbf{D}_s) \tag{28}$$

This expression needs to be linked with experimental quantities.

Changes in the surface tension are called the surface pressure, Π.

$$\Pi = \sigma_o - \sigma \tag{29}$$

σ is the surface tension of a surfactant covered interface, whose concentration may vary with time and position. σ_o is the surface tension of a pure interface at isothermal and isobaric external conditions. For example, the surface tension of a pures water gas phase at 20C is 72.8 nM m^{-1}.

There are three modes for surface deformation. The first mode is dilation. The dilational modulus, E_s, may be defined as

$$E_s = \frac{d\sigma}{d\ln A} \ . \tag{30}$$

The other two modes of in-plane deformations preserve the surface area. These two are shear and extension.

2.4 Goma's Treatment : Surface Excess Properties

Goma's treatment for surfaces with excess properties starts with an expansion of a generalization of Eqn. (15) to include the full Boussinesq-Scriven model, Eqn. (6), for the excess surface stress tensor, $\boldsymbol{P}_s$, after ignoring a lot of terms in the full analysis that are unimportant for

$$\boldsymbol{n} \cdot (\boldsymbol{T}_{in} - \boldsymbol{T}_{ext}) = \nabla_s \cdot (\underline{\boldsymbol{\Upsilon}}_s) \tag{31}$$

Thus,

$$\boldsymbol{n} \cdot (\boldsymbol{T}_{in} - \boldsymbol{T}_{ext}) = \nabla_s \cdot (\sigma \mathbf{I}_s + (\kappa_s - \mu_s)(\mathbf{I}_s : \mathbf{D}_s)\mathbf{I}_s + 2\mu_s \mathbf{D}_s) \tag{32}$$

Now, the first term can be manipulated with the relation

$$\nabla_s \cdot (\mathbf{I}_s) = 2H\boldsymbol{n}$$

to yield

$$\boldsymbol{n} \cdot (\boldsymbol{T}_{in} - \boldsymbol{T}_{ext}) = 2H\sigma\boldsymbol{n} + \nabla_s\sigma + \nabla_s \cdot ((\kappa_s - \mu_s)(\mathbf{I}_s : \mathbf{D}_s)\mathbf{I}_s + 2\mu_s\mathbf{D}_s) \tag{33}$$

The second term may be reduced via the previously derived expression

$$\boldsymbol{n} \cdot (\boldsymbol{T}_{in} - \boldsymbol{T}_{ext}) = 2H\sigma\boldsymbol{n} + \nabla_s\sigma + \nabla_s \cdot ((\kappa_s - \mu_s)(\nabla_s \cdot \boldsymbol{v})\mathbf{I}_s + 2\mu_s\mathbf{D}_s) \tag{34}$$

We should pause for a moment and reflect on Eqn. (34), as it may represent an alternative formulation to the one that will follow below. Let’s rewrite Eqn. (34) in the following way

$$\boldsymbol{n} \cdot (\boldsymbol{T}_{in} - \boldsymbol{T}_{ext}) = 2H\sigma\boldsymbol{n} + \nabla_s\sigma + \nabla_s \cdot (\underline{\underline{\boldsymbol{\tau}}}_s) \tag{35}$$

We can see that the first two terms on the rhs are consistent with the previous treatment of interfacial surface tension within Goma. The last term introduces a new tensor, $\underline{\underline{\boldsymbol{\tau}}}_s$, defined as

$$\underline{\underline{\boldsymbol{\tau}}}_s = ((\kappa_s - \mu_s)(\nabla_s \cdot \boldsymbol{v})\mathbf{I}_s + 2\mu_s\mathbf{D}_s) \tag{36}$$

$\underline{\underline{\boldsymbol{\tau}}}_s$ is a symmetric tensor with 6 unique entries. One thought would be to calculate these six intermediate entries on shell equations. Then we may use Eqn. (36) to calculate the excess contribution to the momentum balance due to the surface phase. We need to introduce intermediate variables within Eqn. (35), because Eqn. (35) involves second derivatives in the velocities, and these can not be resolved with accuracy using our current biquadratic finite element formulations. On consideration of all the issues we haver faced so far, the direct calculation of $\mathbf{D}_s$ or $\underline{\underline{\boldsymbol{\tau}}}_s$ via shell equation may well be the best approach, especially for non-newtonian rheology. However, that was not our initial approach in this treatment.

Well, continuing on with regrets. The second term on the rhs may be simplified assuming that κ_s and μ_s are constants (even if they aren’t, the extensions to nonconstant expressions are relatively straightforward) and using the expression $\mathbf{I}_s \cdot \nabla_s = \nabla_s$:

$$\nabla_s \cdot (\mathbf{I}_s(\kappa_s - \mu_s)(\nabla_s \cdot \boldsymbol{v})) = 2H\boldsymbol{n}(\kappa_s - \mu_s)(\nabla_s \cdot \boldsymbol{v}) + (\kappa_s - \mu_s)\nabla_s(\nabla_s \cdot \boldsymbol{v}) \tag{37}$$

The last term may be expanded, taking care of flipping the transpose where needed, to ensure the correct idenceses are used:

$$\begin{aligned} \nabla_s \cdot (2\mu_s\mathbf{D}_s) &= \mu_s\nabla_s \cdot [(\nabla_s\boldsymbol{v}) \cdot \mathbf{I}_s + \mathbf{I}_s \cdot (\nabla_s\boldsymbol{v})^T] \\ &= \mu_s[(\nabla_s \cdot \nabla_s\boldsymbol{v})\mathbf{I}_s + ((\nabla_s\boldsymbol{v})^T : \nabla_s\mathbf{I}_s)] \\ &\quad + \mu_s[2H(\nabla_s\boldsymbol{v}) \cdot \boldsymbol{n} + \nabla_s \cdot (\nabla_s\boldsymbol{v})^T] \end{aligned} \tag{38}$$

Below we will make heavy use of the surface curvature dyadic, $\boldsymbol{b}$, defined as

$$\boldsymbol{b} = -\nabla_s\boldsymbol{n} \tag{39}$$

which expresses the change of the local surface normal with respect to the position (q^1, q^2) on the surface. $\boldsymbol{b}$ lies in the plane of the surface, is symmetric, and can be reduced to

$$b = \kappa_1 e_1 e_1 + \kappa_1 e_2 e_2,$$

where κ_1 and κ_2 are the principle moments of the curvature of the surface and e_α, which are orthogonal to one another, are the principle directions, i.e., the eigenvectors of b. Also,

$$H = \frac{1}{2}(\mathbf{I}_s : b) = \frac{1}{2}(\kappa_1 + \kappa_1) \tag{40}$$

Ok, then we use the following identities:

$$\nabla_s \mathbf{I}_s = bn + nb$$

So that

$$\begin{aligned} ((\nabla_s v)^T : \nabla_s \mathbf{I}_s) &= ((\nabla_s v)^T : bn) + (\nabla_s v)^T : nb \\ &= (b : (\nabla_s v))n + b \cdot (\nabla_s v) \cdot n \end{aligned} \tag{41}$$

given that b is symmetric. And we may use

$$\nabla_s \cdot (\nabla_s v)^T = \nabla_s(\nabla_s \cdot v) - (b \cdot (\nabla_s v) \cdot n) + (b : (\nabla_s v))n \tag{42}$$

so that we may obtain Eqn. (43) from plugging Eqn. (41) and Eqn. (42) into Eqn. (38).

$$\begin{aligned} \nabla_s \cdot (2\mu_s \mathbf{D}_s) &= \mu_s[(\nabla_s \cdot \nabla_s v)\mathbf{I}_s + 2(b : (\nabla_s v))n \\ &\quad + 2H(\nabla_s v) \cdot n + \nabla_s(\nabla_s \cdot v)] \end{aligned} \tag{43}$$

Collecting terms, the rhs of Eqn. (34) becomes.

$$\begin{aligned} &= 2H\sigma n + \nabla_s \sigma + 2Hn(\kappa_s - \mu_s)(\nabla_s \cdot v) + (\kappa_s - \mu_s)\nabla_s(\nabla_s \cdot v) \\ &\quad + \mu_s[(\nabla_s \cdot \nabla_s v)\mathbf{I}_s + 2(b : (\nabla_s v))n] \\ &\quad + \mu_s[2H(\nabla_s v) \cdot n + \nabla_s(\nabla_s \cdot v)] \end{aligned} \tag{44}$$

$$\begin{aligned} &= 2H\sigma n + \nabla_s \sigma + 2Hn(\kappa_s - \mu_s)(\nabla_s \cdot v) + (\kappa_s + \mu_s)\nabla_s(\nabla_s \cdot v) \\ &\quad + \mu_s[(\nabla_s \cdot \nabla_s v)\mathbf{I}_s + 2(b : (\nabla_s v))n] \\ &\quad + \mu_s[2H(\nabla_s v) \cdot n - \nabla_s(\nabla_s \cdot v)] \end{aligned} \tag{45}$$

$$
\begin{aligned}
&= 2H\sigma\boldsymbol{n} + \nabla_s\sigma + 2H\boldsymbol{n}(\kappa_s+\mu_s)(\nabla_s\cdot\boldsymbol{v}) + (\kappa_s+\mu_s)\nabla_s(\nabla_s\cdot\boldsymbol{v}) \\
&\qquad + \mu_s[(\nabla_s\cdot\nabla_s\boldsymbol{v})\mathbf{I}_s + 2(\boldsymbol{b} : (\nabla_s\boldsymbol{v}))\boldsymbol{n}] \\
&\qquad + \mu_s[2H(\nabla_s\boldsymbol{v})\cdot\boldsymbol{n} - \nabla_s(\nabla_s\cdot\boldsymbol{v}) - 4H(\boldsymbol{n}(\mu_s)(\nabla_s\cdot\boldsymbol{v}))]
\end{aligned}
\tag{46}
$$

$$
\begin{aligned}
&= 2H\sigma\boldsymbol{n} + \nabla_s\sigma + 2H\boldsymbol{n}(\kappa_s+\mu_s)(\nabla_s\cdot\boldsymbol{v}) + (\kappa_s+\mu_s)\nabla_s(\nabla_s\cdot\boldsymbol{v}) \\
&\qquad + \mu_s[(\nabla_s\cdot\nabla_s\boldsymbol{v})\mathbf{I}_s + 2H(\nabla_s\boldsymbol{v})\cdot\boldsymbol{n}] \\
&\qquad + \mu_s[2(\boldsymbol{b} : (\nabla_s\boldsymbol{v}) - 2H(\nabla_s\cdot\boldsymbol{v}))\boldsymbol{n} - \nabla_s(\nabla_s\cdot\boldsymbol{v})]
\end{aligned}
\tag{47}
$$

$$
\begin{aligned}
&= 2H\sigma\boldsymbol{n} + \nabla_s\sigma + 2H\boldsymbol{n}(\kappa_s+\mu_s)(\nabla_s\cdot\boldsymbol{v}) + (\kappa_s+\mu_s)\nabla_s(\nabla_s\cdot\boldsymbol{v}) \\
&\qquad + \mu_s[(\nabla_s\cdot\nabla_s\boldsymbol{v})\mathbf{I}_s + 2H(\nabla_s\boldsymbol{v})\cdot\boldsymbol{n}] \\
&\qquad + \mu_s\Big[2\Big(\boldsymbol{b} : (\nabla_s\boldsymbol{v}) - 2H\Big(\mathbf{I}_s : (\nabla_s\boldsymbol{v})\Big)\Big)\boldsymbol{n} - \nabla_s(\nabla_s\cdot\boldsymbol{v})\Big]
\end{aligned}
\tag{48}
$$

Then, we may use the following relation

$$
\begin{aligned}
\boldsymbol{n}\times\nabla_s[(\nabla_s\times\boldsymbol{v})\cdot\boldsymbol{n}] &= (\nabla_s\cdot\nabla_s\boldsymbol{v})\mathbf{I}_s - \nabla_s(\nabla_s\cdot\boldsymbol{v}) \\
&\qquad + (2\boldsymbol{b} - 2H\mathbf{I}_s)\cdot(\nabla_s\boldsymbol{v})\cdot\boldsymbol{n}
\end{aligned}
\tag{49}
$$

to rearrange the terms on the rhs of Eqn. (48).

$$
\begin{aligned}
&= 2H\sigma\boldsymbol{n} + \nabla_s\sigma + 2H\boldsymbol{n}(\kappa_s+\mu_s)(\nabla_s\cdot\boldsymbol{v}) + (\kappa_s+\mu_s)\nabla_s(\nabla_s\cdot\boldsymbol{v}) \\
&\qquad + \mu_s[\boldsymbol{n}\times\nabla_s[(\nabla_s\times\boldsymbol{v})\cdot\boldsymbol{n}] + 2H(\nabla_s\boldsymbol{v})\cdot\boldsymbol{n}] \\
&\qquad + \mu_s\Big[2\Big(\boldsymbol{b} : (\nabla_s\boldsymbol{v}) - 2H\Big(\mathbf{I}_s : (\nabla_s\boldsymbol{v})\Big)\Big)\boldsymbol{n} - ((2\boldsymbol{b} - 2H\mathbf{I}_s)\cdot(\nabla_s\boldsymbol{v})\cdot\boldsymbol{n})\Big]
\end{aligned}
\tag{50}
$$

Combining terms:

$$
\begin{aligned}
\boldsymbol{n}\cdot(\boldsymbol{T}_{in} - \boldsymbol{T}_{ext}) &= 2H\sigma\boldsymbol{n} + \nabla_s\sigma + 2H\boldsymbol{n}(\kappa_s+\mu_s)(\nabla_s\cdot\boldsymbol{v}) + (\kappa_s+\mu_s)\nabla_s(\nabla_s\cdot\boldsymbol{v}) \\
&\qquad + \mu_s[\boldsymbol{n}\times\nabla_s[(\nabla_s\times\boldsymbol{v})\cdot\boldsymbol{n}]] \\
&\qquad + \mu_s\Big[2\Big((\boldsymbol{b} - 2H\mathbf{I}_s) : (\nabla_s\boldsymbol{v})\Big)\boldsymbol{n} - (2(\boldsymbol{b} - 2H\mathbf{I}_s)\cdot(\nabla_s\boldsymbol{v})\cdot\boldsymbol{n})\Big]
\end{aligned}
\tag{51}
$$

Eqn. (51) is in agreement with Eqn. 4.2-20 on p. 110 of Edwards et al.[6]

2.4.1 Case Study: Cartesian Coordinates with flat interface with $\boldsymbol{n} = \boldsymbol{k}$.

The flat interface simplifies Eqn. (51) greatly. First, $H = 0$ and $\boldsymbol{b} = \boldsymbol{0}$, so only the second, fourth, and fifth term in Eqn. (51) is nonzero. The fourth term is

$$(\kappa_s + \mu_s)\nabla_s(\nabla_s \cdot \boldsymbol{v}) = (\kappa_s + \mu_s)\left(\boldsymbol{i}\frac{d}{dx}\left(\frac{dv_x}{dx} + \frac{dv_y}{dy}\right) + \boldsymbol{j}\frac{d}{dy}\left(\frac{dv_x}{dx} + \frac{dv_y}{dy}\right)\right) \tag{52}$$

The fifth term is a bit complicated. First, let's calculate $\nabla_s \times \boldsymbol{v}$. The key formula to remember for taking cross products within orthonormal coordinate systems is Eqn. (53).

$$\boldsymbol{\delta_i} \times \boldsymbol{\delta_j} = \sum_{k=1}^{3} \varepsilon_{ijk}\boldsymbol{\delta}_k \tag{53}$$

where ε_{ijk} is the permutation operator. Then, considering that $\boldsymbol{n} = \boldsymbol{k}$,

$$\begin{aligned}\nabla_s \times \boldsymbol{v} &= ((\boldsymbol{I} - \boldsymbol{nn}) \cdot \nabla) \times \boldsymbol{v} = \left(\boldsymbol{i}\frac{d}{dx} + \boldsymbol{j}\frac{d}{dy}\right) \times (\boldsymbol{i}v_x + \boldsymbol{j}v_y + \boldsymbol{k}v_z) \\ &= \boldsymbol{i}\left(\frac{dv_z}{dy}\right) + \boldsymbol{j}\left(-\frac{dv_z}{dx}\right) + \boldsymbol{k}\left(\frac{dv_y}{dx} - \frac{dv_x}{dy}\right)\end{aligned} \tag{54}$$

Then, taking the dot product with the surface normal again yields

$$(\nabla_s \times \boldsymbol{v}) \cdot \boldsymbol{n} = \frac{dv_y}{dx} - \frac{dv_x}{dy} \tag{55}$$

The surface gradient of Eqn. (55) is a vector oriented in the plane of the surface:

$$\nabla_s\left(\frac{dv_y}{dx} - \frac{dv_x}{dy}\right) = \boldsymbol{i}\frac{d}{dx}\left(\frac{dv_y}{dx} - \frac{dv_x}{dy}\right) + \boldsymbol{j}\frac{d}{dy}\left(\frac{dv_y}{dx} - \frac{dv_x}{dy}\right) \tag{56}$$

so

$$\begin{aligned}\boldsymbol{n} \times \nabla_s[(\nabla_s \times \boldsymbol{v}) \cdot \boldsymbol{n}] &= k \times \left(\boldsymbol{i}\frac{d}{dx}\left(\frac{dv_y}{dx} - \frac{dv_x}{dy}\right) + \boldsymbol{j}\frac{d}{dy}\left(\frac{dv_y}{dx} - \frac{dv_x}{dy}\right)\right) \\ &= \boldsymbol{i}\left(\frac{d}{dy}\left(\frac{dv_x}{dy} - \frac{dv_y}{dx}\right)\right) + \boldsymbol{j}\left(\frac{d}{dx}\left(\frac{dv_y}{dx} - \frac{dv_x}{dy}\right)\right)\end{aligned} \tag{57}$$

Putting this all together yields

$$\begin{aligned} -\boldsymbol{n}\cdot(\boldsymbol{T}_{in}-\boldsymbol{T}_{ext}) \;=\; & \nabla_s\sigma+(\kappa_s+\mu_s)\Big(\boldsymbol{i}\frac{d}{dx}\Big(\frac{dv_x}{dx}+\frac{dv_y}{dy}\Big)+\boldsymbol{j}\frac{d}{dy}\Big(\frac{dv_x}{dx}+\frac{dv_y}{dy}\Big)\Big) \\ & +\boldsymbol{i}\Big(\frac{d}{dy}\Big(\frac{dv_x}{dy}-\frac{dv_y}{dx}\Big)\Big)+\boldsymbol{j}\Big(\frac{d}{dx}\Big(\frac{dv_y}{dx}-\frac{dv_x}{dy}\Big)\Big) \end{aligned} \tag{58}$$

This formula agrees with Edwards, p. 112.

2.4.2 Case Study: Cylindrical Coordinates with a perfectly cylindrical interface $\boldsymbol{n} = \boldsymbol{r}$.

Let's assume that the fluid is a cylinder with $R = R(t)$ Then $\boldsymbol{n} = \boldsymbol{e_r}$ and the surface curvature tensor, $\boldsymbol{b}$, becomes:

$$\begin{aligned} \boldsymbol{b} &= -\nabla_s\boldsymbol{n} = -((\boldsymbol{I}_s-\boldsymbol{e}_r\boldsymbol{e}_r)\cdot\nabla)\boldsymbol{n} \\ &= -\Big(\boldsymbol{e}_z\frac{d}{dz}+\boldsymbol{e}_\theta\frac{1}{r}\frac{d}{d\theta}\Big)\boldsymbol{e}_r \qquad , \\ &= -\boldsymbol{e}_\theta\boldsymbol{e}_\theta\frac{1}{R_o} \end{aligned} \tag{59}$$

and

$$H = \frac{1}{2}\boldsymbol{I}_s : \boldsymbol{b} = -\frac{1}{2R_o} \tag{60}$$

so $\boldsymbol{b}-2H\mathbf{I}_s = -\boldsymbol{e}_\theta\boldsymbol{e}_\theta\frac{1}{R_o}+\frac{1}{R_o}(\boldsymbol{e}_\theta\boldsymbol{e}_\theta+\boldsymbol{e}_z\boldsymbol{e}_z) = \frac{1}{R_o}\boldsymbol{e}_z\boldsymbol{e}_z$.
The first and second term is

$$2H\sigma\boldsymbol{n}+\nabla_s\sigma = -\boldsymbol{e}_r\frac{\sigma}{R_0}+\boldsymbol{e}_\theta\frac{1}{R_0}\frac{d\sigma}{d\theta}+\boldsymbol{e}_z\frac{d\sigma}{dz} \tag{61}$$

The third term first needs a definition of the surface divergence.

$$\begin{aligned} \nabla_s\cdot\boldsymbol{v} &= \Big(\boldsymbol{e}_z\frac{d}{dz}+\boldsymbol{e}_\theta\frac{1}{r}\frac{d}{d\theta}\Big)\cdot(\boldsymbol{e}_r v_r+\boldsymbol{e}_\theta v_\theta+\boldsymbol{e}_z v_z) \\ &= \frac{dv_z}{dz}+\frac{1}{r}\frac{dv_\theta}{d\theta}+\frac{v_r}{r} \end{aligned} \tag{62}$$

Therefore,

$$2H\boldsymbol{n}(\kappa_s+\mu_s)(\nabla_s\cdot\boldsymbol{v}) = \boldsymbol{e}_r\Big(-\frac{(\kappa_s+\mu_s)}{R_0}\Big)\Big(\frac{dv_z}{dz}+\frac{1}{R_0}\frac{dv_\theta}{d\theta}+\frac{v_r}{R_0}\Big) \tag{63}$$

The fourth term is

$$
\begin{aligned}
(\kappa_s + \mu_s)\nabla_s(\nabla_s \cdot \boldsymbol{v}) &= (\kappa_s + \mu_s)\left(\boldsymbol{e}_z\frac{d}{dz} + \boldsymbol{e}_\theta\frac{1}{r}\frac{d}{d\theta}\right)\left(\frac{dv_z}{dz} + \frac{1}{r}\frac{dv_\theta}{d\theta} + \frac{v_r}{r}\right) \\
&= (\kappa_s + \mu_s)\left(\boldsymbol{e}_z\frac{d}{dz}\left(\frac{dv_z}{dz} + \frac{1}{R_o}\frac{dv_\theta}{d\theta} + \frac{v_r}{R_o}\right) + \boldsymbol{e}_\theta\frac{1}{r}\frac{d}{d\theta}\left(\frac{dv_z}{dz} + \frac{1}{R_o}\frac{dv_\theta}{d\theta} + \frac{v_r}{R_o}\right)\right)
\end{aligned}
$$

The 5th term is

$$
\begin{aligned}
\nabla_s \times \boldsymbol{v} &= \left(\boldsymbol{e}_z\frac{d}{dz} + \boldsymbol{e}_\theta\frac{1}{r}\frac{d}{d\theta}\right) \times (\boldsymbol{e}_r v_r + \boldsymbol{e}_{\boldsymbol{\theta}} v_\theta + \boldsymbol{e}_z v_z) \\
&= \boldsymbol{e}_{\boldsymbol{\theta}}\left(\frac{dv_r}{dz}\right) + \boldsymbol{e}_r\left(-\frac{dv_\theta}{dz} + \frac{1}{R_o}\frac{dv_z}{d\theta}\right) + \boldsymbol{e}_z\left(-\frac{dv_r}{d\theta} + \frac{v_\theta}{R_o}\right)
\end{aligned} \tag{64}
$$

Therefore,

$$
\boldsymbol{n} \cdot (\nabla_s \times \boldsymbol{v}) = \frac{1}{R_o}\frac{dv_z}{d\theta} - \frac{dv_\theta}{dz} \tag{65}
$$

And,

$$
\begin{aligned}
\nabla_s(\boldsymbol{n} \cdot (\nabla_s \times \boldsymbol{v})) &= \left(\boldsymbol{e}_z\frac{d}{dz} + \boldsymbol{e}_\theta\frac{1}{r}\frac{d}{d\theta}\right)\left(\frac{1}{R_o}\frac{dv_z}{d\theta} - \frac{dv_\theta}{dz}\right) \\
&= \boldsymbol{e}_z\frac{d}{dz}\left(\frac{1}{R_o}\frac{dv_z}{d\theta} - \frac{dv_\theta}{dz}\right) + \boldsymbol{e}_\theta\frac{1}{R_o}\frac{d}{d\theta}\left(\frac{1}{R_o}\frac{dv_z}{d\theta} - \frac{dv_\theta}{dz}\right)
\end{aligned} \tag{66}
$$

so that

$$
\boldsymbol{n} \times \nabla_s(\boldsymbol{n} \cdot (\nabla_s \times \boldsymbol{v})) = -\boldsymbol{e}_\theta\frac{d}{dz}\left(\frac{1}{R_o}\frac{dv_z}{d\theta} - \frac{dv_\theta}{dz}\right) + \boldsymbol{e}_z\frac{1}{R_o}\frac{d}{d\theta}\left(\frac{1}{R_o}\frac{dv_z}{d\theta} - \frac{dv_\theta}{dz}n\right) \tag{67}
$$

The 6th term is (68)

$$
\begin{aligned}
\mu_s\left[2\Big((\boldsymbol{b} - 2H\mathbf{I}_s) : (\nabla_s\boldsymbol{v})\Big)\boldsymbol{n}\right] &= 2\mu_s\left[\left(\frac{\boldsymbol{e}_z\boldsymbol{e}_z}{R_o}\right) : (\nabla_s\boldsymbol{v})\right]\boldsymbol{e}_r \\
&= \boldsymbol{e}_r 2\frac{\mu_s}{R_o}\frac{dv_z}{dz}
\end{aligned} \tag{69}
$$

The 7th term is (70)

$$\begin{aligned}(-\mu_s)[(2(\boldsymbol{b}-2H\mathbf{I}_s)\cdot(\nabla_s\boldsymbol{v})\cdot\boldsymbol{n})] &= (-\mu_s)2\left(\frac{\boldsymbol{e}_z\boldsymbol{e}_z}{R_o}\cdot(\nabla_s\boldsymbol{v})\cdot\boldsymbol{e}_r\right) \\ &= (-\mu_s)2\left(\frac{\boldsymbol{e}_z}{R_o}\left(\frac{dv_r}{dz}\right)\right)\end{aligned} \tag{71}$$

Combining terms

$$\begin{aligned}\boldsymbol{n}\cdot(\boldsymbol{T}_{in}-\boldsymbol{T}_{ext})\cdot\boldsymbol{e}_\theta &= \frac{1}{R_0}\frac{d\sigma}{d\theta}+\frac{(\kappa_s+\mu_s)}{R_0}\frac{d}{d\theta}\left(\frac{dv_z}{dz}+\frac{1}{R_o}\frac{dv_\theta}{d\theta}+\frac{v_r}{R_o}\right) \\ &\quad -\mu_s\frac{d}{dz}\left(\frac{1}{R_o}\frac{dv_z}{d\theta}-\frac{dv_\theta}{dz}\right)\end{aligned} \tag{72}$$

$$\begin{aligned}\boldsymbol{n}\cdot(\boldsymbol{T}_{in}-\boldsymbol{T}_{ext})\cdot\boldsymbol{e}_z &= \frac{d\sigma}{dz}+(\kappa_s+\mu_s)\frac{d}{dz}\left(\frac{dv_z}{dz}+\frac{1}{R_o}\frac{dv_\theta}{d\theta}+\frac{v_r}{R_o}\right) \\ &\quad +\mu_s\frac{1}{R_o}\frac{d}{d\theta}\left(\frac{1}{R_o}\frac{dv_z}{d\theta}-\frac{dv_\theta}{dz}\right)-2\mu_s\frac{d}{dz}\left(\frac{v_r}{R_o}\right)\end{aligned} \tag{73}$$

$$\boldsymbol{n}\cdot(\boldsymbol{T}_{in}-\boldsymbol{T}_{ext})\cdot\boldsymbol{e}_r = -\frac{\sigma}{R_0}+\left(-\frac{(\kappa_s+\mu_s)}{R_0}\right)\left(\frac{dv_z}{dz}+\frac{1}{R_0}\frac{dv_\theta}{d\theta}+\frac{v_r}{R_0}\right)+2\frac{\mu_s}{R_o}\frac{dv_z}{dz} \tag{74}$$

There are actually several differences between Eqns. (72) - (74) and the corresponding formulas in Edwards [6] p.113. Eqns. (72) - (74) include an v_r/R_o term that stems from the $\nabla\cdot\boldsymbol{v}$ formula in cylindrical coordinates. The corresponding formulas in Edwards [6] don't have the v_r/R_o term. However, I can't see why that term shouldn't exist. Also, Eqn. (73) contains an extra $-2\mu_s\frac{d}{dz}\left(\frac{v_r}{R_o}\right)$ term that stems from the 7th term in Eqn. (51) calculated in Eqn. (71). Again, it's not in Edwards, and I don't see why not. Lastly, Eqn. (74) does not contain the $-\kappa_s v_r/R_0^2$ term that the Edwards book has. Actually it does, but the multiplier is $\kappa_s+\mu_s$ instead of κ_s, and it's part of the $\nabla\cdot\boldsymbol{v}$ term. Resolution of these differences awaits further checking or alternative methods for derivation.

2.4.3 Case Study: Cylindrical Coordinates with a perfectly flat interface $\boldsymbol{n} = \boldsymbol{k}$.

Let's assume that the interface occurs on a plane in the axial coodinate Then, $\boldsymbol{n} = \boldsymbol{e}_z$ and the surface curvature tensor, $\boldsymbol{b}$, turns out to be identically zero. Also $H = 0$.

The first and second term is

$$2H\sigma\boldsymbol{n}+\nabla_s\sigma = \boldsymbol{e}_\theta\frac{1}{r}\frac{d\sigma}{d\theta}+\boldsymbol{e}_r\frac{d\sigma}{dr} \tag{75}$$

The third term first needs a definition of the surface divergence.

$$\begin{aligned}\nabla_s \cdot \boldsymbol{v} &= \left(\boldsymbol{e}_r \frac{d}{dr} + \boldsymbol{e}_\theta \frac{1}{r}\frac{d}{d\theta}\right) \cdot (\boldsymbol{e}_r v_r + \boldsymbol{e}_{\boldsymbol{\theta}} v_\theta + \boldsymbol{e}_z v_z) \\ &= \frac{dv_r}{dr} + \frac{1}{r}\frac{dv_\theta}{d\theta} + \frac{v_r}{r}\end{aligned} \tag{76}$$

Therefore,

$$2H\boldsymbol{n}(\kappa_s + \mu_s)(\nabla_s \cdot \boldsymbol{v}) = 0 \tag{77}$$

The fourth term is

$$\begin{aligned}(\kappa_s + \mu_s)\nabla_s(\nabla_s \cdot \boldsymbol{v}) &= (\kappa_s + \mu_s)\left(\boldsymbol{e}_r \frac{d}{dr} + \boldsymbol{e}_\theta \frac{1}{r}\frac{d}{d\theta}\right)\left(\frac{dv_r}{dr} + \frac{1}{r}\frac{dv_\theta}{d\theta} + \frac{v_r}{r}\right) \\ &= (\kappa_s + \mu_s)\left(\boldsymbol{e}_r \frac{d}{dr}\left(\frac{dv_r}{dr} + \frac{1}{r}\frac{dv_\theta}{d\theta} + \frac{v_r}{r}\right) + \boldsymbol{e}_\theta \frac{1}{r}\frac{d}{d\theta}\left(\frac{dv_r}{dr} + \frac{1}{r}\frac{dv_\theta}{d\theta} + \frac{v_r}{r}\right)\right)\end{aligned}$$

The 5th term is

$$\begin{aligned}\nabla_s \times \boldsymbol{v} &= \left(\boldsymbol{e}_r \frac{d}{dr} + \boldsymbol{e}_\theta \frac{1}{r}\frac{d}{d\theta}\right) \times (\boldsymbol{e}_r v_r + \boldsymbol{e}_{\boldsymbol{\theta}} v_\theta + \boldsymbol{e}_z v_z) \\ &= \boldsymbol{e}_{\boldsymbol{\theta}}\left(-\frac{dv_z}{dr}\right) + \boldsymbol{e}_r\left(\frac{1}{r}\frac{dv_z}{d\theta}\right) + \boldsymbol{e}_z\left(\frac{dv_\theta}{dr} - \frac{1}{r}\frac{dv_r}{d\theta} + \frac{v_\theta}{r}\right)\end{aligned} \tag{78}$$

Therefore,

$$\boldsymbol{n} \cdot (\nabla_s \times \boldsymbol{v}) = \frac{dv_\theta}{dr} - \frac{1}{r}\frac{dv_r}{d\theta} + \frac{v_\theta}{r} \tag{79}$$

And,

$$\begin{aligned}\nabla_s(\boldsymbol{n} \cdot (\nabla_s \times \boldsymbol{v})) &= \left(\boldsymbol{e}_r \frac{d}{dr} + \boldsymbol{e}_\theta \frac{1}{r}\frac{d}{d\theta}\right)\left(\frac{dv_\theta}{dr} - \frac{1}{r}\frac{dv_r}{d\theta} + \frac{v_\theta}{r}\right) \\ &= \boldsymbol{e}_r \frac{d}{dr}\left(\frac{dv_\theta}{dr} - \frac{1}{r}\frac{dv_r}{d\theta} + \frac{v_\theta}{r}\right) + \boldsymbol{e}_\theta \frac{1}{r}\frac{d}{d\theta}\left(\frac{dv_\theta}{dr} - \frac{1}{r}\frac{dv_r}{d\theta} + \frac{v_\theta}{r}\right)\end{aligned} \tag{80}$$

so that

$$\boldsymbol{n} \times \nabla_s(\boldsymbol{n} \cdot (\nabla_s \times \boldsymbol{v})) = \boldsymbol{e}_\theta \frac{d}{dr}\left(\frac{dv_\theta}{dr} - \frac{1}{r}\frac{dv_r}{d\theta} + \frac{v_\theta}{r}\right) - \boldsymbol{e}_r \frac{1}{r}\frac{d}{d\theta}\left(\frac{dv_\theta}{dr} - \frac{1}{r}\frac{dv_r}{d\theta} + \frac{v_\theta}{r}\right) \tag{81}$$

The 6th and 7th terms are zero. Combining terms (82)

$$\boldsymbol{n} \cdot (\boldsymbol{T}_{in} - \boldsymbol{T}_{ext}) \cdot \boldsymbol{e}_\theta = \frac{1}{r}\frac{d\sigma}{d\theta} + \frac{(\kappa_s + \mu_s)}{r}\frac{d}{d\theta}\left(\frac{dv_r}{dr} + \frac{1}{r}\frac{dv_\theta}{d\theta} + \frac{v_r}{r}\right)$$
$$+ \mu_s\frac{1}{r}\frac{d}{d\theta}\left(\frac{dv_\theta}{dr} - \frac{1}{r}\frac{dv_r}{d\theta} + \frac{v_\theta}{r}\right) \tag{83}$$

$$\boldsymbol{n} \cdot (\boldsymbol{T}_{in} - \boldsymbol{T}_{ext}) \cdot \boldsymbol{e}_z = 0 \tag{84}$$

$$\boldsymbol{n} \cdot (\boldsymbol{T}_{in} - \boldsymbol{T}_{ext}) \cdot \boldsymbol{e}_r = \frac{d\sigma}{dr} + (\kappa_s + \mu_s)\left(\boldsymbol{e}_r\frac{d}{dr}\left(\frac{dv_r}{dr} + \frac{1}{r}\frac{dv_\theta}{d\theta} + \frac{v_r}{r}\right)\right)$$
$$+ \mu_s\frac{d}{dr}\left(\frac{dv_\theta}{dr} - \frac{1}{r}\frac{dv_r}{d\theta} + \frac{v_\theta}{r}\right) \tag{85}$$

One example of this type of flow is pure swirling flow, where $\boldsymbol{v} = \boldsymbol{e}_\theta ar$. Then, we note that

$$\boldsymbol{n} \cdot (\nabla_s \times \boldsymbol{v}) = \frac{dv_\theta}{dr} - \frac{1}{r}\frac{dv_r}{d\theta} + \frac{v_\theta}{r} = 2a \tag{86}$$

reflecting the fact that this is a pure vortex flow case/ Therefore, the derivative of this is zero and

$$\boldsymbol{n} \cdot (\boldsymbol{T}_{in} - \boldsymbol{T}_{ext}) = \boldsymbol{0} \ . \tag{87}$$

The later formula reflects the fact that there is no shearing of the surface layer occurring for pure swirling flow. Therefore, the jump in surface traction shouldn't depend upon μ_s or κ_s.

3.0 Shell Variables Pertaining to the Surface Rheology Treatment

3.1 Gamma4

As a first step intermediary variables are calculated using Goma shell element capability

The 4th variable is $\Gamma_4 = (\nabla_s \times \boldsymbol{v}) \cdot \boldsymbol{n}$.

The residual equation for this is

$$\int_{d\Omega} (\Gamma_4 - ((\nabla_s \times \boldsymbol{v}) \cdot \boldsymbol{n}))\Phi_i d\Gamma = 0 \tag{88}$$

Using Gaussian integration the formula for ths projection equation becomes Eqn. (89).

$$R = \sum(\Gamma_4 - ((\nabla_s \times \boldsymbol{v}) \cdot \boldsymbol{n}))\Phi_i \|J_{shell}\|(h_1 h_2 h_3) \tag{89}$$

Let's take a look at what this variable turns out to be, in several simple cases. Eqn. (86) demonstrates an example of a non-zero term. From the discussion in 2.4.2 and Eqn. (65), it turns out that the Γ_4 is zero in cylindrical coordinates, when there is no swirling flow, i.e., when v_θ is zero.

3.2 Surface Normal Unknowns

The surface normal may be calculated in 2D problems using the variable SH_N1 and SH_N2

$$\boldsymbol{n}^{sh} = \boldsymbol{n} = \frac{\boldsymbol{t}_1 \times \boldsymbol{t}_2}{det(\boldsymbol{J}_s)} \tag{90}$$

In 2D problems this reduces to

$$\boldsymbol{n}^{sh} = \begin{bmatrix} \mathrm{SH\_N1} \\ \mathrm{SH\_N2} \end{bmatrix} = \begin{bmatrix} \dfrac{t[0][1]}{det(\boldsymbol{J}_s)} \\ \dfrac{-t[0][0]}{det(\boldsymbol{J}_s)} \end{bmatrix} \tag{91}$$

The residual equations for these in 2D are

$$\int_{d\Omega} \left(\mathrm{SH\_N1} - \frac{t[0][1]}{det(\boldsymbol{J}_s)}\right)\Phi_i d\Gamma = 0 \tag{92}$$

$$\int_{d\Omega} \left(\mathrm{SH\_N2} + \frac{t[0][0]}{det(\boldsymbol{J}_s)}\right)\Phi_i d\Gamma = 0$$

Corresponding equations for 3D shells apply as well. The calculation of surface normals is described in the Coordinate systems memo for goma [8]. No surface diffusion was added to this equatoin. It seems to work and bunaffected by noise.

3.3 Surface Divergence of the velocity

The surface divergence of the velocity may be calculated using the following formula.

$$\Gamma_1 = \nabla_s \cdot \boldsymbol{v} = ((\mathbf{I} - \boldsymbol{n}\boldsymbol{n}) \bullet \nabla) \bullet \boldsymbol{v} \tag{93}$$

Within goma this may be directly solved as

$$\Gamma_1 = ((\mathbf{I} - \boldsymbol{nn}) \bullet \nabla) \bullet \boldsymbol{v} = (\mathbf{I} - \boldsymbol{nn}):\nabla \boldsymbol{v} = \sum_{i=1}^{VIM} \sum_{j=1}^{VIM} \left(\delta_{ij} \frac{\partial v_i}{\partial x_j} - n_i n_j \frac{\partial v_i}{\partial x_j} \right) \tag{94}$$

$\nabla \boldsymbol{v}$ is the gradient of the velocity, a tensor. An explicit example of this would be the pure swirling flow with a flat interface in cylindrical coordinates, where $\boldsymbol{n} = \boldsymbol{e}_z$. In this case $\boldsymbol{v} = ar\boldsymbol{e}_\theta$. And,

$$\Gamma_1 = \nabla_s \cdot \boldsymbol{v} = \frac{\partial}{\partial r} v_r + \frac{1}{r} \frac{\partial v_\theta}{\partial \theta} + \frac{v_r}{r} = 0 \tag{95}$$

For the case of a flat interface, the variable for the surface divergence is $\Gamma_1 = \nabla_s \cdot v$ would be identically zero as v_r is equal to zero unless the domain boundaries in the radial direction are oscillating.

Another example of interest would be an expanding or contracting spherical bubble. In this case

$$\begin{aligned} \Gamma_1 &= \nabla_s \cdot \boldsymbol{v} = (\boldsymbol{e}_\theta \boldsymbol{e}_\theta + \boldsymbol{e}_\phi \boldsymbol{e}_\phi):\left(\left(\frac{1}{r} \frac{\partial v_\theta}{\partial \theta} + \frac{v_r}{r} \right) \boldsymbol{e}_\theta \boldsymbol{e}_\theta + \left(\frac{1}{r \sin\theta} \frac{\partial v_\phi}{\partial \phi} + \frac{v_r}{r} + \frac{v_\theta}{r} \cot\theta \right) \boldsymbol{e}_\phi \boldsymbol{e}_\phi \right) = 0 \\ &= \frac{1}{r} \frac{\partial v_\theta}{\partial \theta} + \frac{2 v_r}{r} + \frac{1}{r \sin\theta} \frac{\partial v_\phi}{\partial \phi} + \frac{v_\theta}{r} \cot\theta \end{aligned} \tag{96}$$

The residual equation for this is

$$\int_{d\Omega} (\Gamma_1 - (\nabla_s \cdot v)) \Phi_i d\Gamma = 0 \tag{97}$$

Note, we have had tremendous difficulting solving Eqn. (97) in practice. The issue was that such a refined mesh was needed that the calculations ground to a halt. However, we believe it may be beneficial to rewrite Eqn. (97) to lower the order of the equation. We start with the expression, which is an expression of the surface divergence theorum.

$$\int_{d\Omega} (\nabla_s \cdot \boldsymbol{v} \Phi_i) d\Gamma = \int_{d\Omega} (\boldsymbol{m} \cdot \boldsymbol{v} \Phi_i) d\gamma - \int_{d\Omega} 2H(\boldsymbol{n} \cdot \boldsymbol{v} \Phi_i) d\Gamma \tag{98}$$

In this expression, the mean surface curvature H is equal to

$$H = -\left(\frac{1}{2} \nabla_s \cdot \boldsymbol{n} \right) = \frac{1}{2} (\kappa_{min} + \kappa_{max}) \tag{99}$$

Just for review, κ_{min} and κ_{max} are the minimum and maximum principle radii of curvature. Note for spheres the way we have defined the mean surface curvature, H is equal to $-1/r$, where the sign is correct (curvatures are negative for convex cases where $\boldsymbol{n}$ points out of the enclosed object.

We may then expand the lhs of Eqn. (98) to achieve Eqn. (100).

$$\int_{d\Omega} (\nabla_s \cdot \boldsymbol{v}\Phi_i)d\Gamma = \int_{d\Omega} \Phi_i(\nabla_s \cdot \boldsymbol{v})d\Gamma + \int_{d\Omega} (\boldsymbol{I}-\boldsymbol{nn}):(\boldsymbol{v}(\nabla\Phi_i))d\Gamma \tag{100}$$

Then, we may combine the two equations to yield Eqn. (101).

$$\int_{d\Omega} \Phi_i(\nabla_s \cdot \boldsymbol{v})d\Gamma = -\int_{d\Omega} (\boldsymbol{I}-\boldsymbol{nn}):(\boldsymbol{v}(\nabla\Phi_i))d\Gamma + \int_{d\gamma} (\boldsymbol{m} \cdot \boldsymbol{v}\Phi_i)d\gamma - \int_{d\Omega} 2H\Phi_i(\boldsymbol{n} \cdot \boldsymbol{v})d\Gamma \tag{101}$$

The revised equation has some merits over the initial equation because the order of the unknown, $\boldsymbol{v}$, has been reduced by one in the expression. Therefore, we may expect that the convergence of the variable $\Gamma_1 = \nabla_s \cdot v$ will be greatly enhanced by the restatement of the equation. It also separates out important parts of the original expression. In particular, the last part of the expression, which is proportional to the mean curvature, H, is distinctly separated out, leaving terms that are exceedingly small for normal conditions that don't consist of outflow boundary conditions involving flowing surfaces, i.e., where $\boldsymbol{m} \cdot \boldsymbol{v}\Phi_i$ is nonzero.

The expression in Eqn. (100) may be written out

$$(\boldsymbol{I}-\boldsymbol{nn}):(\boldsymbol{v}(\nabla\Phi_i)) = \sum_{a=1}^{VIM}\sum_{b=1}^{VIM}\left(\delta_{ab}v_a\frac{1}{h_b}\frac{\partial\Phi_i}{\partial q_b} - n_a n_b v_a\frac{1}{h_b}\frac{\partial\Phi_i}{\partial q_b}\right) \tag{102}$$

where h_b is the scale factor for the bth coordinate.

The edge integral, the second expression on the rhs of Eqn. (101) has not been explicitly coded up within Goma. The edge integral is zero for both symmetry boundary conditions and wall contact conditions. It is only non-zero for outflow and inflow boundary conditions with contact lines involving fluids which are flowing into or out of the domain. Our initial test cases don't include any problems of this type.

Initial numerical expeimrents using Eqn. (101) as input to the projection equation instead of the lhs of Eqn. (101) proved problematic. THe end result was that we abaondoned the effort in favor of adding surface difufsion into the projection equations and in going to more refined meshes.

3.3.1 Adding a surface diffusion term

We still have problems with this term. Therefore, let's add in a surface diffusion term. Consider a concentration of a surface species c that undergoes reaction and diffusion. We may write a continuity equation for c.

$$\frac{dc}{dt} + k_f - k_r c = D(\nabla_s \cdot \nabla_s c) \tag{103}$$

By analogy with Eqn. (103), we may write a diffusion addition for Γ_1 keeping track of signs. We will ignore the time dependence, assuming steady state behavior of *c*.

$$-\int_{d\Omega} ((\nabla_s \cdot v) - \Gamma_1)\Phi_i d\Gamma + \int_{d\Omega} D(\nabla_s \cdot \nabla_s \Gamma_1)\Phi_i d\Gamma = 0 \tag{104}$$

We may do the normal integration by parts using the surface divergence theorum. We note that the $\boldsymbol{n} \cdot \nabla_s \Gamma_1 = 0$ term simplifies the resulting expression.

$$-\int_{d\Omega} ((\nabla_s \cdot v) - \Gamma_1)\Phi_i d\Gamma - \int_{d\Omega} D(\nabla_s \Phi_i \cdot \nabla_s \Gamma_1) d\Gamma + \int_{d\gamma} \Phi_i(\boldsymbol{m} \cdot D\nabla_s \Gamma_1) d\gamma = 0\,\mathrm{T} \tag{105}$$

The middle term may additionally be simplified to yield

$$\begin{aligned} -\int_{d\Omega} ((\nabla_s \cdot v) - \Gamma_1)\Phi_i d\Gamma - \int_{d\Omega} D(\nabla \Phi_i \cdot \nabla \Gamma_1 - (\boldsymbol{n} \cdot \nabla \Phi_i)(\boldsymbol{n} \cdot \nabla \Gamma_1)) d\Gamma \\ + \int_{d\gamma} \Phi_i(\boldsymbol{m} \cdot D\nabla_s \Gamma_1) d\gamma = 0 \end{aligned} \tag{106}$$

We don't believe the edge term needs to be implemented at this time for the projection equations for any of the projection equations employed. Eqn. (106) has been implemented with Goma. It appears to be very successful at eliminating problems with the inclusion of noise within the porjection equations.

3.4 Surface Calculation of the Curvature

The local curvature of the surface is calculated as a shell variable, Γ_2 of the velocity may be calculated using the following formula.

$$\Gamma_2 = -\frac{1}{2}\nabla_s \cdot \boldsymbol{n} = -\frac{1}{2}((\mathbf{I} - \boldsymbol{nn}) \bullet \nabla) \bullet \boldsymbol{n} \tag{107}$$

Within goma this is solved as

$$\Gamma_2 = ((\mathbf{I} - \boldsymbol{nn}) \bullet \nabla) \bullet \boldsymbol{v} = \sum_{i=1}^{VIM} \sum_{j=1}^{VIM} \left(\delta_{ij} \frac{\partial n_i}{\partial x_j} - n_i n_j \frac{\partial n_i}{\partial x_j} \right) \tag{108}$$

An explicit example of this would be a pure sphere. In that case $\boldsymbol{n} = \boldsymbol{e}_r$, and

$$\Gamma_2 = -\frac{1}{2}\nabla_s \cdot \boldsymbol{n} = -\frac{1}{2}\left((\mathbf{I} - \boldsymbol{nn}) \bullet \left(\frac{\boldsymbol{e}_\theta \boldsymbol{e}_\theta}{r} + \frac{\boldsymbol{e}_\phi \boldsymbol{e}_\phi}{r}\right)\right) = -\frac{1}{r} \tag{109}$$

A surface diffusion term was added to the equation system as well. This was put in because the curvature variable was observed to have oscillations in its value when the shear viscosity was set to nominal values. These oscillations eventually caused the simulations to break down. The equation that's solved is Eqn. (110).

$$\begin{aligned} -\int_{d\Omega} \left(\left(-\frac{1}{2}\nabla_s \cdot \boldsymbol{n}\right) - \Gamma_2\right)\Phi_i d\Gamma - \int_{d\Omega} D(\nabla\Phi_i \cdot \nabla\Gamma_2 - (\boldsymbol{n} \cdot \nabla\Phi_i)(\boldsymbol{n} \cdot \nabla\Gamma_2))d\Gamma \\ + \int_{d\gamma} \Phi_i(\boldsymbol{m} \cdot D\nabla_s\Gamma_2)d\gamma = 0 \end{aligned} \tag{110}$$

In order to solve issues that arose at r = 0 under cylindrical coordinates we implemented the following boundary condition, which is implemented on the edge of a shell using a collocation strategy.

$$\int_{d\gamma} (\boldsymbol{m} \cdot \nabla\Gamma_2)d\gamma = 0 \tag{111}$$

The card is called GAMMA2_DERIV_SYMM. An example of its implementation is given below.

BC = GAMMA2_DERIV_SYMM NS 101 5 0.0

Collocation boundary conditions are usually applied on the nodes along a side set. However, Goma has been changed for this and the corresponding GAMMA1 boundary condition to apply collocation conditions at a node set consisting of a single point. $\boldsymbol{m}$ is the binormal vector introduced in Eqn. (19). It is the normal tangent to the surface along the line that points out of the surface. Eqn. (111) is applied at the r = 0 point, and replaces the equation at that point, in order to ensure symmetry is enforced. When the shear surface viscosity is nonzero, this additional constraint is apparently necessary.

3.5 Surface Calculation of $\nabla_s \boldsymbol{v} \cdot \boldsymbol{n}$

This term is nonzero because the surface normal operates on the right index and not on the left index of $\nabla_s \boldsymbol{v}$.

$$\boldsymbol{\Gamma_3} = \nabla_s \boldsymbol{v} \cdot \boldsymbol{n} = ((\mathbf{I} - \boldsymbol{nn}) \bullet \nabla \boldsymbol{v}) \bullet \boldsymbol{n} \tag{112}$$

$\boldsymbol{\Gamma_3}$ is a vector quantity. Each of its scalar components, β, is evaluated from the following equation, Eqn. (113).

$$\begin{aligned} &-\int_{d\Omega} ([(\nabla_s \boldsymbol{v} \cdot \boldsymbol{n}) \cdot \boldsymbol{e_\beta}] - \Gamma_3^\beta)\Phi_i d\Gamma - \int_{d\Omega} D(\nabla\Phi_i \cdot \nabla\Gamma_3^\beta - (\boldsymbol{n} \cdot \nabla\Phi_i)(\boldsymbol{n} \cdot \nabla\Gamma_3^\beta))d\Gamma \\ &\qquad + \int_{d\gamma} \Phi_i(\boldsymbol{m} \cdot D\nabla_s\Gamma_3^\beta)d\gamma = 0 \end{aligned} \tag{113}$$

3.6 Surface Terms

Putting it all together, from the finite element formulation, the difference in the normal stresses applied on either side of an interface arises naturally. We have shown that this difference can be expressed by Eqn. (114).

$$\begin{aligned} \boldsymbol{n} \cdot (\boldsymbol{T}_{in} - \boldsymbol{T}_{ext}) = {} & 2H\sigma\boldsymbol{n} + \nabla_s\sigma + 2H\boldsymbol{n}(\kappa_s + \mu_s)(\nabla_s \cdot \boldsymbol{v}) + (\kappa_s + \mu_s)\nabla_s(\nabla_s \cdot \boldsymbol{v}) \\ & + \mu_s[\boldsymbol{n} \times \nabla_s[(\nabla_s \times \boldsymbol{v}) \cdot \boldsymbol{n}]] \\ & + \mu_s\left[2\Big((\boldsymbol{b} - 2H\mathbf{I}_s) : (\nabla_s\boldsymbol{v})\Big)\boldsymbol{n} - (2(\boldsymbol{b} - 2H\mathbf{I}_s) \cdot (\nabla_s\boldsymbol{v}) \cdot \boldsymbol{n})\right] \end{aligned} \tag{114}$$

Let's review what there is already. There are two boundary conditions that apply. One is the CAPILLARY boundary condition. The other is the CAPILLARY_SHEAR_VISC boundary condition.

They are both integrated boundary conditions applied on surfaces. The CAPILLARY boundary condition imposes the following equation on single sided interfaces.

$$\boldsymbol{n} \cdot (\boldsymbol{T}_{in}) = (2)H\sigma\boldsymbol{n} - \boldsymbol{n}P_{ex} + \nabla_s\sigma \tag{115}$$

The CAPILLARY card may also be used for internal surfaces between fluid regions. The formulation turns out to be almost the same. The CAPILLARY card picks one side of the interface (or the user can pick the side alternatively) to be the primary side and implements the same boundary condition with $P_{ex} = 0$. This turns out to implement Eqn. (15) exactly, creating the jump in the pressure across the interface exactly if discontinuous P1 presure interpolations are chosen.

With the addition of surface viscosity, extra terms are needed at the interface. These are represented by terms in Eqn. (114) that are not in Eqn. (15). These are listed in Eqn. (116).

$$\begin{aligned}\boldsymbol{n}\cdot(\boldsymbol{S}_{extra}) = {} & 2H\boldsymbol{n}(\kappa_s+\mu_s)(\nabla_s\cdot\boldsymbol{v})+(\kappa_s+\mu_s)\nabla_s(\nabla_s\cdot\boldsymbol{v}) \\ & +\mu_s[\boldsymbol{n}\times\nabla_s[(\nabla_s\times\boldsymbol{v})\cdot\boldsymbol{n}]] \\ & +\mu_s\Big[2\Big((\boldsymbol{b}-2H\mathbf{I}_s):(\nabla_s\boldsymbol{v})\Big)\boldsymbol{n}-(2(\boldsymbol{b}-2H\mathbf{I}_s)\cdot(\nabla_s\boldsymbol{v})\cdot\boldsymbol{n})\Big]\end{aligned} \tag{116}$$

The CAPILLARY_SHEAR_VISC boundary condition calculates these extra terms and implements them on top of the CAPILLARY card. These are integrated weakly in the galerkin format just as the CAPILLARY card terms..

$$\int_\Gamma\Big(\phi_i\boldsymbol{e}_\beta\boldsymbol{n}:\boldsymbol{S}_{extra}\Big)d\Gamma \tag{117}$$

Let's break down each term in Eqn. (116) and figure out how we are to solve it.

$$\int_\Gamma\phi_i(\boldsymbol{e}_\beta\cdot\boldsymbol{n})2H(\kappa_s+\mu_s)(\nabla_s\cdot\boldsymbol{v})d\Gamma \tag{118}$$

The CAPILLARY_SHEAR_VISC card uses the routine apply_surface_viscosity(). Within the routine the following implementation described by Eqns. (119) to (123) is carried out.

$$2H\boldsymbol{n}(\kappa_s+\mu_s)(\nabla_s\cdot\boldsymbol{v}) = 2\Gamma_2\boldsymbol{n}(\kappa_s+\mu_s)(\Gamma_1) \tag{119}$$

$$(\kappa_s+\mu_s)\nabla_s(\nabla_s\cdot\boldsymbol{v}) = (\kappa_s+\mu_s)\nabla_s(\Gamma_1) \tag{120}$$

$$\mu_s[\boldsymbol{n}\times\nabla_s[(\nabla_s\times\boldsymbol{v})\cdot\boldsymbol{n}]] = \mu_s[\boldsymbol{n}\times\nabla_s\Gamma_4] = \mu_s[\boldsymbol{n}\times\nabla\Gamma_4] \tag{121}$$

$$\mu_s\Big[2\Big((\boldsymbol{b}-2H\mathbf{I}_s):(\nabla_s\boldsymbol{v})\Big)\boldsymbol{n}\Big] = \mu_s[2((\boldsymbol{b}-2\Gamma_2\mathbf{I}_s):(\nabla_s\boldsymbol{v}))\boldsymbol{n}] \tag{122}$$

$$\mu_s[-(2(\boldsymbol{b}-2H\mathbf{I}_s)\cdot(\nabla_s\boldsymbol{v})\cdot\boldsymbol{n})] = \mu_s[-(2(\boldsymbol{b}-2\Gamma_2\mathbf{I}_s)\cdot\boldsymbol{\Gamma}_3)] \tag{123}$$

In Eqns. (122) to (123), the surface diadic is calculated from

$$\mathbf{I}_s = \mathbf{I}-\boldsymbol{nn} \tag{124}$$

In Eqns. (119) to (123), all of the terms only involve single derivatives. Note, we have used Γ_2 in Eqn. (122) to Eqn. (123). It simplifies the arithmetic. However, we wonder whether that is the source of inconsistency. The term $\boldsymbol{b}-2\Gamma_2\mathbf{I}_s$ should be equal to zero identically for planes, cylinders, and spheres. Therefore it might seem that the same interpolation scheme should be used for all element of that vector. However, the significance of this has yet to be checked.

An example example input deck section for the surface equations is provided below

```
MAT = surface 5
 Coordinate System = CYLINDRICAL
 Element Mapping   = isoparametric
 Mesh Motion = ARBITRARY
 Number of bulk species = 0

       Number of EQ  = 7
       EQ = n_dot_curl_v Q2    gamma4 Q2             1.
       EQ = shell_normal1 Q2   SH_N1  Q2             1.
       EQ = shell_normal2 Q2   SH_N2  Q2             1.
       EQ = SHELL_SURF_CURV Q1 gamma2  Q1            1.
       EQ = SHELL_SURF_DIV_V Q1 gamma1  Q1            1.
       EQ = GRAD_V_DOT_N1 Q2 gamma3_1  Q2            1.
       EQ = GRAD_V_DOT_N2 Q2 gamma3_2  Q2            1
```

The CAPILLARY_SHEAR boundary condition is applied via the following cards.

```
#
#      CAPILLARY
#        Set the surface tension at the interface
#
BC = CAPILLARY SS 1 72. 0.0 0.0
BC = CAPILLARY_SHEAR_VISC SS 1 1.0  1.0  1.2 4.8
```

The first two doubles (after the identification of the side set on which the boundary condition is applied, i.e., SS 1) are the surface shear viscosity and the surface dilatational viscosity. The last two doubles on the card are optional parameters indicating the initial time and final time for a ramp of the surface viscosity values. If those numbers are on the card, a linear time ramp in the values of τ_s and κ_s from an initial value of zero for both of those parameters is carried out between the two times. For example in the case above the surface viscosity terms are ramped up form 1.2 to 4.8 seconds. This time ramp has been found to be useful in starting out the time dependent calculations. In those calculations there is frequently an oscillatory quasi-equilibration period at the start of the calculations, and it is easier to achieve the quasi-equilibrium without the addition of the surface viscosity terms.

3.7 Other Boundary conditions

For the cylindrical geometry cases where we are solving fluid mechanics at r = 0, we have implemented a boundary condition imposing a zero radial gradient at r = 0 for the axial velocity. An example of the card usage is

```
#        Set the axial velocity’s radial derivative
#
BC = DVZDR_ZERO SS 4
```

This boundary condition is applied as a collocated boundary condition, therefore throwing out the surface integral at r = 0 which is problematic in any case. Note, in all cases setting the radial velocity to zero is employed.

3.8 Results of the Capillary Bubble Problem.

It became clear at the end of the program that there were unresolved issues in the formulation that prevented the oscillating bubble problem from being solved correctly. In particular it was found using a heuristic approach that a sign on one of the surface rheology terms had to be flipped in order for the equations to be solved successfully.

$$\begin{aligned} \boldsymbol{n} \cdot (\boldsymbol{T}_{in} - \boldsymbol{T}_{ext}) = {} & 2H\sigma\boldsymbol{n} + \nabla_s\sigma + 2H\boldsymbol{n}(\kappa_s + \mu_s)(\nabla_s \cdot \boldsymbol{v}) + (\kappa_s + \mu_s)\nabla_s(\nabla_s \cdot \boldsymbol{v}) \\ & + \mu_s[\boldsymbol{n} \times \nabla_s[(\nabla_s \times \boldsymbol{v}) \cdot \boldsymbol{n}]] \\ & + \mu_s\Big[2\Big((\boldsymbol{b} - 2H\mathbf{I}_s) : (\nabla_s\boldsymbol{v})\Big)\boldsymbol{n} - (2(\boldsymbol{b} - 2H\mathbf{I}_s) \cdot (\nabla_s\boldsymbol{v}) \cdot \boldsymbol{n})\Big] \end{aligned} \tag{125}$$

The sign of the term that had to be flipped was the last term on the first line, $(\kappa_s + \mu_s)\nabla_s(\nabla_s \cdot \boldsymbol{v})$. Without flipping this term, the solution appeared to gain energy even under quiescent conditions. Recirculations would appear in the bubble problem that revolved in both directions depending upon the starting conditions. When the sign was flipped to a negative value, this degree of freedom disappeared. This behavior is characteristic of a non-null null-space for the jacobian for the positive sign and the violation of the first law of thermodynamics.

Just to reiterate, there is no theoretical basis for the flipping the sign. The fact that it was necessary indicates that there is an error within Goma of some sort.

While I was able to solve dilatational viscosity problems with this kluge of an arbitrary value of κ_s, I was not able to do the same for the shear surface viscosity problems. The culprit was the first term on the last line of Eqn. (125). Even flipping the sign didn't help that term. The calculations reached a point where it appeared that the problem became ill-conditioned and the step changes in the solution variables did not decrease along with the residual values. Again, this is characteristic of a Jacobian that is near singular, with a non-null null vector. The null vector seemed to include mostly surface terms involving the vector $(\nabla_s\boldsymbol{v}) \cdot \boldsymbol{n}$, which appeared to be constant and the value of $(\nabla_s \cdot \boldsymbol{v})$, whose value was constant throughout the bubble surface. This null vector also included a contribution from ΔP the pressure drop accross the bubble surface.

3.9 Recommendation

It's recommended that an approach based on returning to a raw formulation of the surface stresses be used. The starting condition for this formulation would be Eqn. (32). In this formulation the shell variables to be used would be the individual components of $\boldsymbol{D}_s$, of which there are 6 (because it's symmetric). We are guessing here that using the raw surface strain components $\boldsymbol{D}_s$ should less problematic just as using the raw bulk strain tensor is less problematic for bulk viscosity formulations.

An additional advantage for this formulation is that non-newtonian formulations for the surface shear and dilational viscosities could be employed in a rigorous and straightfoward manner, once the method is verified using newtonian viscosities.

4.0 References

1. S. Reynaert, C. F. Brooks, P. Moldenaers, J. Vermant, G. G. Fuller, "Analysis of the Magnetic Rod Interfacial Stress Rheometer," *J. of Rheology,* to appear (2008).

2. C. F. Brooks, "An Interfacial Stress Rheometer to Study the Shear Rheology of Langmuir Monolayers," Ph. D. Thesis Stanford University (1999).

3. *GOMA 5.0 A Full Newton Finite Element Program for Free and Moving Boundary Problems for Free and Moving Boundary Problems with Coupled Fluid/Solid Momentum, Energy Mass, and Chemical Species Transport: User's Guild.* P. R. Schunk et al., SAND Report 2006-5375/1, Sandia National Laboratories, Albuquerque, NM.

4. P. R. Schunk, "Surface-Rheology Models in GOMA: Boussinesq-Scriven Newtonian-Capillary Free surface model and others: User Tutorial," Sandia Memo, Sandia National Laboratories, NM 87185, March 4 (2005).

5. L. E. Scriven, "Dynamics of a Fluid Interface," *Chem. Eng. Sci.,* **12**, 98–108 (1960).

6. Edwards, D. A. Brenner, H. Wasan, D. T, *Interfacial Transport Processes and Rheology,* Betterworth-Heinemann, Boston, 1991.

7. R. A. Cairncross, P. R. Schunk, T. A. Baer, R. R. Rao, P. A. Sackinger, "A finite element method for free surface flows of incompressible fluids in three dimensions Part I. Baundary fitted mesh option," *Int. J. for Numerical Methods in Fluids*, **33**, 375-403 (2000).

8. H. K. Moffat "Treatment of Coordinate Systems within Goma," Sandia National Labs Memo, Albuquerque, NM (2010).

9. R. B. Bird, W. E. Stewart, E. N. Lightfoot, Transport Phenomena 2nd Ed., J. Wiley and Sons, NY, NY 2002.

5.0 Distribution

Dayfile	1516	
MS 0834	1510	J. S. Lash
MS 0601	1516	H. K. Moffat
MS 0601	1514	R. R. Rao
MS 0346	1513	C. F. Brooks
MS 0601	1514	L. A. Mondy
MS 0346	1513	A. M. Grillet

MS 0601	1516	P. R. Schunk
MS 0601	1514	D. R. Noble
MS 0382	1541	P. K. Notz
MS 0601	1513	D. J. Rader

APPENDIX D: PENDENT DROPLET ANALYSIS WITH GOMA

Sandia National Laboratories

Operated for the U.S. Department of Energy by
Sandia Corporation
Albuquerque, New Mexico 87185-

date: 09/10/10

to: Distribution

from: Harry K. Moffat,

subject: Pendent Droplet Analysis

1 Introduction and Summary

We wish to create a tool for measuring and quantifying dilatational surface viscosities. We will use an oscillating pendent drop to do this. A pendent drop will form a shape that differs from a sphere due to the gravitational force. That difference is called the Young-Laplace equation. To measure the dilatational viscosity it's then necessary to oscillate the droplet using the piston action of a syringe.

Oscillations of the droplet cause net bulk-viscosity terms to appear in the solution through the pressure terms of the surface. It's necessary to subtract off these terms in order to get at the surface viscosity terms.

2 Initial Problem

The initial problem has air in the droplet and water outside.

CGS units are used throughout the calculation

I've used the following properties for air

$\rho = 9.34\text{E-4}$ gm / cm3 (N2 at 620 torr)

$\mu = 1.8\text{E-4}$ gm / cm s

I've used the following properties for water

$\rho = 1.0$ gm / cm3

$\mu = 0.01$ gm / cm s

Exceptional Service in the National Interest

3 Analytical Answer

This discussion follows closely from Freer et al [2]. Assume a bubble on the end of a syringe is perfectly spherical. Assume that we can vary the bubble volume in a sinusoidal manner. Then, the volume constraint equation has the following form

$$V = V_o + \Delta V \sin \omega t = \frac{4\pi}{3} R^3 \qquad \text{with} \quad R = \left(\frac{3V}{4\pi} \right)^{1/3} \tag{1}$$

The instantaneous volumetric flow rate into the bubble Q is given by Eqn. (3).

$$Q = \frac{dV}{dt} = \Delta V \cos \omega t \tag{2}$$

Therefore, the time-dependent radius is given by Eqn. (4).

$$R = \left(\frac{3V_o}{4\pi} \right)^{1/3} \left[1 + \frac{\Delta V}{V_o} \sin \omega t \right]^{1/3} \tag{3}$$

The derivative of the radius with respect to time is given by Eqn. (5).

$$\frac{1}{R}\frac{dR}{dt} = \frac{1}{3}\frac{1}{V}\frac{dV}{dt} = \frac{1}{3}\frac{\Delta V \omega \cos \omega t}{V} = \frac{1}{3}\left(\frac{\Delta V \omega \cos \omega t}{V_o + \Delta V \sin \omega t} \right) \tag{4}$$

At the interface the following holds, if surface rheology is ignored.

$$\boldsymbol{n} \bullet \left(\boldsymbol{T}_{in} - \boldsymbol{T}_{ext} \right) = 2H\sigma \boldsymbol{n} \tag{5}$$

The normal component of the stress within the droplet and expterior to the droplet using different material properties is given by the following equations:

$$T_{rr} = +2\mu \frac{dv_r}{dr} - \left(\frac{2}{3}\mu - \kappa \right) (\nabla \bullet \boldsymbol{v}) - p_b \tag{6}$$

Therefore assuming that the drop is spherical the *r* component in spherical coordinates of Eqn. (5) becomes Eqn. (8). Note all terms are evaluated at the surface of the bubble which is expanding and contractin with time.

$$+2\left(\mu_{in} - \mu_{ext} \right) \left. \frac{dv_r}{dr} \right|_{r=R} - \left(p_{in} - p_{ext} \right) = 2H\sigma = \frac{-2\sigma}{R} \tag{7}$$

At the surface of the bubble, the velocity of the fluid is equal to the rate of radial expansion of the bubble, Eqn. (9).

$$v_r\Big|_{r=R} = \frac{dR}{dt} = \frac{R}{3}\frac{\Delta V\,\omega\,\cos\omega t}{V} = \frac{R}{3}\left(\frac{\Delta V\,\omega\,\cos\omega t}{V_o + \Delta V\sin\omega t}\right) \tag{8}$$

The continuity equation, Eqn. (10), may be used to compute the radial velocity.

$$\nabla\bullet\boldsymbol{v} \ = \frac{dv_r}{dr} + 2\frac{v_r}{r} = 0 \tag{9}$$

Therefore, it must be the case that the following holds so that continuity holds at all radii and at all times.

$$v_r = \frac{a}{r^2} \tag{10}$$

Then, we may use Eqn. (8) to find *a*.

$$a = R^2 v_r = R^2\frac{dR}{dt} = \frac{R^3}{3}\frac{\Delta V\,\omega\cos\omega t}{V} = \frac{R^3}{3}\left(\frac{\Delta V\,\omega\cos\omega t}{V_o + \Delta V\sin\omega t}\right) \tag{11}$$

$$a = R^2 v_r = R^2\frac{dR}{dt} = \frac{R^3}{3}\frac{\Delta V\,\omega\cos\omega t}{V} = \frac{R^3}{3}\left(\frac{\Delta V\,\omega\cos\omega t}{V_o + \Delta V\sin\omega t}\right) = \frac{\Delta V\,\omega\cos\omega t}{4\pi}$$

Therefore, the gradient of the velocity throughout the bubble is given by Eqn. (13).

$$\frac{dv_r}{dr} = -2\frac{v_r}{r} = -\frac{2a}{r^3} = -\frac{2}{r^3}\frac{\Delta V\,\omega\,\cos\omega t}{4\pi} = -\frac{\Delta V\,\omega\,\cos\omega t}{2\pi r^3} \tag{12}$$

We may use Eqn. (12) and apply it at the bubble surface to complete the derivation of the stress balance at the surface.

$$\left(\mu_{in} - \mu_{ext}\right)\left(\frac{-\Delta V\,\omega\cos\omega t}{\pi R^3}\right) - \left(p_{in} - p_{ext}\right) = 2H\sigma = \frac{-2\sigma}{R} \tag{13}$$

The last formula agrees with Freer's Eqn. (4).

$$\left(\mu_{in} - \mu_{ext}\right)\left(\frac{\Delta V\,\omega\,\cos\omega t}{\pi\left(\frac{3V_o}{4\pi}\right)\left[1 + \frac{\Delta V}{V_o}\sin\omega t\right]}\right) + \left(p_{in} - p_{ext}\right) = \frac{2\sigma}{R} \tag{14}$$

So

$$\sigma = \left(\mu_{in} - \mu_{ext}\right)\left(\frac{\Delta V \omega \cos \omega t}{2\pi\left(\frac{3V_o}{4\pi}\right)^{2/3}\left[1+\frac{\Delta V}{V_o}\sin \omega t\right]^{2/3}}\right) + \frac{\left(p_{in} - p_{ext}\right)}{2}\left(\frac{3V_o}{4\pi}\right)^{1/3}\left[1+\frac{\Delta V}{V_o}\sin \omega t\right]^{1/3} \tag{15}$$

Free et al. (4) seem to go off the deep end at this point, defining an effective surface tension from the formula

$$\sigma_{eff} = \sigma - \left(\mu_{in} - \mu_{ext}\right)\left(\frac{\Delta V \omega \cos \omega t}{2\pi R^2}\right) \tag{16}$$

They do this because the surface tension measured from a Young-Laplace analysis of their data indicate that the variations in the surface tension is 90 degrees out of phase with the volume oscillations. The formula in Eqn. (16) yields the phase lag, though it monumentally fails in predicting the magnitude of the effect observed in their experiment.

The entire formula is weird in the sense that σ_{eff} is observed to have the phase lag, but it is a steady-state quantity. σ_{eff} is suppose to be able to be calculated from the shape of the droplet from a Young-Laplace analysis. However, that analysis only applies to the steady state. A better approach would be to take account of the transient response.

3.1Macroscopic Balance

Let's take the momentum equation and form a macroscopic balance around the bubble assuming spherical symmetry. We will integrate over all angles, and assume the densities are constant in the two phases.

$$\rho \frac{dv}{dt} + \rho\left(v - v_m\right) \bullet \nabla v = \nabla \bullet T + f \tag{17}$$

We get the following equation

$$\rho \int \frac{dv_r}{dt} dV_{\mathrm{int}} + \rho \int \frac{dv_r}{dt} dV_{ext} = \int \left(\nabla \bullet \boldsymbol{T}\right) \bullet \boldsymbol{e}_r \, dV + \int f \, dV \tag{18}$$

This represents a macroscopic balance

$$\rho\int\frac{dv_r}{dt}dV_{\text{int}}+\rho\int\frac{dv_r}{dt}dV_{ext}=\int \boldsymbol{e}_r\bullet\left(\nabla\bullet\boldsymbol{T}\right)dV+\int f\,dV$$

$$=n\bullet\left(\boldsymbol{T}_{in}-\boldsymbol{T}_{ext}\right)\Big|_{r=R}+\int \boldsymbol{e}_r\bullet\left(\nabla\bullet\boldsymbol{T}\right)dV_{in}+\int \boldsymbol{e}_r\bullet\left(\nabla\bullet\boldsymbol{T}\right)dV_{ext}$$

$$\rho\int\frac{dv_r}{dt}dV_{\text{int}}+\rho\int\frac{dv_r}{dt}dV_{ext}=4\pi R^2\left(\boldsymbol{e}_r\bullet\left(\boldsymbol{T}_{in}-\boldsymbol{T}_{ext}\right)\bullet n\Big|_{r=R}\right)+\int \boldsymbol{e}_r\bullet\left(\nabla\bullet\boldsymbol{T}\right)dV_{in}+\int \boldsymbol{e}_r\bullet\left(\nabla\bullet\boldsymbol{T}\right)dV_{ext}$$

$$=4\pi R^2\left(2H\sigma n+2Hn\left(\kappa_s+\mu_s\right)\left(\nabla_s\bullet v\right)\right)+\int \boldsymbol{e}_r\bullet\left(\nabla\bullet\boldsymbol{T}\right)dV_{in}+\int \boldsymbol{e}_r\bullet\left(\nabla\bullet\boldsymbol{T}\right)dV_{ext}$$

$$\rho\int\frac{dv_r}{dt}dV_{\text{int}}+\rho\int\frac{dv_r}{dt}dV_{ext}=4\pi R^2\left(\boldsymbol{e}_r\bullet\left(\boldsymbol{T}_{in}-\boldsymbol{T}_{ext}\right)\bullet n\Big|_{r=R}\right)+\int \boldsymbol{e}_r\bullet\left(\nabla\bullet\boldsymbol{T}\right)dV_{in}+\int \boldsymbol{e}_r\bullet\left(\nabla\bullet\boldsymbol{T}\right)dV_{ext}$$

$$=4\pi R^2\left(2H\sigma+2\left(\frac{-1}{R}\right)\left(\kappa_s+\mu_s\right)\left(\frac{v_r}{R}\right)\right)+\int \boldsymbol{e}_r\bullet\left(\nabla\bullet\boldsymbol{T}\right)dV_{in}+\int \boldsymbol{e}_r\bullet\left(\nabla\bullet\boldsymbol{T}\right)dV_{ext} \tag{19}$$

Note the surface tension term has a negative sign as well. This represents the extra energy that must be employed to create more surface area when the bubble is expanding.

The negative sign in front of the surface viscosity term is a necessary condition for a viscosity term. It represents the fact that the viscosity terms represent dampening forces. If the sign were switched in Eqn. (19), the solution, for a sufficiently high surface viscosity to overcome the other dampening terms from the bulk viscosity, would be represented by an exponentially growing velocity without bounds.

3.2Addition of a Surface Dilatational Viscosity Component

With the addition of a dilatational viscosity component the following Eqn. (21) is true.

$$\boldsymbol{n}\bullet\left(\boldsymbol{T}_{in}-\boldsymbol{T}_{ext}\right)=2H\sigma\boldsymbol{n}+2H\left(\kappa_s+\mu_s\right)\left(\nabla_s\bullet v\right)\boldsymbol{n} \tag{20}$$

Assuming spherical symmetry for the drop, the following is true

$$\nabla_s \bullet v = 2\frac{v_r}{R} = -\left.\frac{dv_r}{dr}\right|_{r=R} \tag{21}$$

Therefore,

$$\boldsymbol{n}\bullet\left(\boldsymbol{T}_{in} - \boldsymbol{T}_{ext}\right) = 2H\sigma\boldsymbol{n} + 2\left(\frac{-1}{R}\right)\left(\kappa_s + \mu_s\right)\left(-\left.\frac{dv_r}{dr}\right|_{r=R}\right)\boldsymbol{n} \tag{22}$$

Now, we plug in the definition of the tractions on the lhs and we obtain.

$$+2\left(\mu_{in} - \mu_{ext}\right)\left.\frac{dv_r}{dr}\right|_{r=R} - \left(p_{in} - p_{ext}\right) = 2\left(\frac{-1}{R}\right)\sigma + 2\left(\frac{-1}{R}\right)\left(\kappa_s + \mu_s\right)\left(-\left.\frac{dv_r}{dr}\right|_{r=R}\right) \tag{23}$$

Or

$$\left(p_{in} - p_{ext}\right) = \frac{2\sigma}{R} + 2\left(\frac{\left(\kappa_s + \mu_s\right)}{R} + \left(\mu_{in} - \mu_{ext}\right)\right)\left(-\left.\frac{dv_r}{dr}\right|_{r=R}\right) \tag{24}$$

This is exactly the same formula that derived without the dilatational component in Eqn. (13). Therefore, the previous analysis carries forward with the dilatational viscosity terms being added to the formulas. For example, Eqn. (16) is replaced with Eqn. (26).

$$\sigma_{eff} = \sigma - \left(\frac{\left(\kappa_s + \mu_s\right)}{R} + \left(\mu_{in} - \mu_{ext}\right)\right)\left(\frac{\Delta V\omega\cos\omega t}{2\pi R^2}\right) \tag{25}$$

3.3 NUMERICAL IMPLEMENTATION

I am trying to change the volume using a piston. I do an augmented boundary condition to enforce the movement of the piston. The variable that I employ to with this augmented boundary condition is the static pressure head that is entered on the FLOW_PRESSURE boundary condition at the inlet to the syringe.

```
BC = FLOW_PRESSURE   SS 31 950. 0.0
```

The 950 in the above boundary condition card is the pressure value at the inlet to the syringe. This is used to modulate the flow into the syringe, because elsewhere in the domain the pressure is set to zero on an open boundary condition using the FLOW_PRESSURE card with a zero static pressure. Therefore, this sets up a pressure driving force that drives the gas or liquid into the domain according to a volume constraint imposed on the size of the bubble at the head of the syringe.

BC = FLOW_PRESSURE SS 11 0.0

Therefore, this sets up a pressure driving force that drives the gas or liquid into the domain according to a volume constraint imposed on the size of the bubble at the head of the syringe.

$$V = V_o + \Delta V \sin \omega t = \frac{4\pi}{3} R^3 \qquad \text{with} \qquad R = \left(\frac{3V}{4\pi} \right)^{1/3} \tag{26}$$

The logic for this piston simulation is currently implemented in the routine user_ac.c

The actual augmented boundary condition has the following form

$$f_{ac} = n_o RT - PV_{tot} \quad \text{where } V_{tot} = V_{ext} + V_{\text{int}} \tag{27}$$

V_{int} is calculated by Goma's internal volume integrator, and includes the volumes for the syringe and the bubble. It includes effects associated with the moving mesh.

$$V_{ext} = V_{ext}^o - V_{loss}^o - A \sin\left(\frac{t2\pi}{\lambda} \right) \tag{28}$$

where

$$n_o = \frac{P_o \left(V_{\text{int}}^o + V_{ext}^o \right)}{RT} \qquad \text{with } P_o = \text{OneAtm} + 1000. \tag{29}$$

V_{ext}^o is a buffer value equal to 0.3 cm^3. V_{int}^o is equal to the initial volume of the internal domain, which includes the inside of the syringe and the bubble, as calculated by Goma's internal volume integrator.

V_{loss}^o is used to adjust the total volume of the bubble, from its initial value to a final value that hopefully agrees with experiment, via a ramp function

$$V_{loss}^o = \begin{cases} V_{loss}^{amplitude} \left(\dfrac{t}{t_{ramp}} \right) & t < t_{ramp} \\ V_{loss}^{amplitude} & t > t_{ramp} \end{cases} \tag{30}$$

Currently, $t_{ramp} = 5$ secs.

P is the current pressure in the bubble, including both the thermodynamic, static and the hydrodynamic pressure assuming that the hydrodynamic pressure is near zero throughout the bubble and the static pressure is equal to the applied pressure at the inlet to the syringe. With this assumption this hydrodynamic plus static pressure becomes equal to the pressure applied on the FLOW_PRESSURE card at the inlet to the syringe, P_{inlet}. The total pressure P is given by adding the thermodynamic pressut to that Eqn. (32).

$$P \;= \mathrm{OneAtm} + P_{inlet} \tag{31}$$

Note, as is usual for low speed flows of gases, the thermodynamic pressure head OneAtm (1.0E6) is much greater than the hydrodynamic pressure and is also much greater than the static pressure head (1000) as well.

So, assuming that the static pressure is a constant, which it is up to the third significant digit, the equations would reduce to a value of

$$V_{bub} = V_{bub}^{o} + V_{loss}^{o} + A\sin\left(\frac{2\pi t}{\lambda}\right) \tag{32}$$

This is equivalent to the analytical representation.

4 References

1. H. Wong, D. Rumschitzki, C. Maldarelli, Theory and experiment on the low-Reynolds-number expansion and contraction of a bubble pinned at a submerged tube tip, J. Fluid Mech., 356, 93-124 (1998).
2. 2. E. M. Freer, H. Wong, C. J. Radke, Oscillating drop/bubble Tensiometry: effect of viscous forces on the measurement of interfacial tension," *J. Colloid and Interface Science*, 282 128-132 (2005).

Distribution:

1	MS0346	Chris Bourdon	01512
3	MS0346	Lisa Mondy	01512
1	MS0346	Anne Grillet	01512
1	MS0346	Carlton Brooks	01512
1	MS0836	Harry Moffat	01516
1	MS0828	Melissa Yaklin	01513
1	MS0346	Tim Koehler	01513
1	MS0826	Jaime Castañeda	01512
1	MS0826	Raymond Cote	01512
1	MS0836	Rekha Rao	01514
1	MS0899	Technical Library	9536 (electronic copy)
1	MS0123	D. Chavez, LDRD Office	1011 (electronic copy)

Sandia National Laboratories